

NOVEL STABLE ISOTOPE METHODS TO QUANTIFY GLUCOSE METABOLISM

By

Martha Lynn Wall

Thesis

Submitted to the Faculty of the
Graduate School of Vanderbilt University
in partial fulfillment of the requirements
for the degree of

MASTER OF SCIENCE

in

Chemical and Physical Biology

December, 2016

Nashville, Tennessee

Approved:

Jamey D. Young, Ph.D.

Owen P. McGuinness, Ph.D.

ACKNOWLEDGEMENTS

I am thankful for admission into the Interdisciplinary Graduate Program at Vanderbilt University and the stimulating first year of classes and laboratory rotations. I had wonderful experiences in each rotation lab. I am especially grateful for Dr. Raf Van de Plas who provided me with the best advice I received during graduate school. “Let’s build something cool today!”

My labmates in the Young lab were generous with support and advice. Dr. Robert Egnatchik and Dr. Alexandra Leamy were my role models. I had many productive conversations with Dr. Lara Jazmin, and I enjoyed building cool things with her input. I will always hold my friendship with Adeola Adebisi close to my heart. She has extremely good taste in music and footwear. “It’s who I am!”

Collaborations in the O’Brien and Wasserman labs were very productive. Notably, working with Dr. Curtis Hughey was an honor. He always treated me and my work with respect, and for that, I will always be grateful.

I was humbled to receive the Honor Fellowship awarded by the Graduate School. My graduate career was funded, in part, by both the Molecular Endocrinology Training Program (DK07563) and the Mouse Metabolic Phenotyping Center MICROMouse award (DK076169) from NIH and CBET 0955251 from NSF.

TABLE OF CONTENTS

	Page
ACKNOWLEDGEMENTS	ii
LIST OF TABLES	vi
LIST OF FIGURES	vii
Chapter	
I. GENERAL INTRODUCTION	1
II. SAMPLE PROCESSING AND ANALYSIS OF GC-MS DATA	6
Preparation of glucose derivatives	6
GC-MS analysis	8
Integration of glucose derivative peaks	8
Guided integration using integrate_gcms	10
Evaluation of the accuracy of fragment measurements from biological samples	11
Positional enrichment analysis of glucose	12
The effect of measurement error on enrichment estimates	13
Automated glucose positional enrichment analysis	16
Conclusions and Future Directions	17
III. APPLICATION TO GLUCOSE CYCLING	21
Introduction	21
Experimental design	24

Quantification of glucose cycling in WT and <i>G6pc2</i> KO islets isolated from CF mice.....	29
Quantification of glucose cycling in WT and <i>G6pc2</i> KO islets isolated from HFF mice	31
Quantification of the influence of extracellular glucose concentration on glucose cycling.....	32
Conclusions of isolated mouse islet experiments	36
Future directions	39
IV. APPLICATION TO METABOLIC FLUX ANALYSIS	46
Introduction.....	46
Modeling hepatic glucose production in INCA	47
Proof-of-concept: [U- ¹³ C ₃]-propionate infusion rate study	51
Proof-of-concept: Fasting study.....	58
Effect of CO ₂ recycling on flux values.....	61
Validation: ² H ₂ O and [6,6- ² H ₂]glucose.....	64
Conclusions and Future Directions.....	71
V. SUMMARY OF CONCLUSIONS.....	74
Appendix	
A. USER MANUAL FOR THE INTEGRATION GUI	76
B. USER MANUAL FOR THE POSITIONAL ANALYSIS GUI.....	99
C. DERIVATION OF GLUCOSE CYCLING EQUATION	109

D. USER MANUAL FOR THE BATCH GUI.....	111
E. DESCRIPTION OF MATHEMATICAL MODELING FOR FLUX ANALYSIS ...	116
REFERENCES	127

LIST OF TABLES

Table	Page
2.1 Maximum RMSE in fragment measurement from plasma samples	12
2.2 Effect of measurement error on enrichment analysis of simulated biological mixtures.....	14
3.1 Comparison of glucose cycling and uptake among experimental groups.....	35
3.2 Glucose cycling in isolated human islets	44
4.1 Metabolic network model for in vivo metabolic flux analysis	49
4.2 Metabolites with equivalent hydrogen atoms	50
4.3 Effect of CO ₂ recycling on SSR and simulated CO ₂ enrichment.	64
4.4 Percent difference between simulated and measured MIDs with or without ¹³ CO ₂ recycling.....	71
A.1 Description of NetCDF_data subfields	92
A.2 Correlation between MSLib subfields and method table columns	93
E.1 Gluc.ext EMUs correspond to measured glucose fragments.....	118
E.2 EMU Balance Equations	119

LIST OF FIGURES

Figure	Page
1.1 Positional enrichment analysis of glucose using overlapping GC-MS fragments.....	4
1.2 Overview of GC-MS-based positional enrichment methodology	5
2.1 Overview of sample and data processing.....	6
2.2 The integrate_gcms GUI guides a user through integration to produce MIDs.....	11
2.3 Effect of measurement error on enrichment analysis of a simulated biological mixture	15
2.4 The gpa GUI automates positional analysis of glucose	17
2.5 Glucose production in cultured hepatocytes under gluconeogenic conditions	19
2.6 Chromatogram from a 1:1:1 mixture of glucose derivatives	19
3.1 Glucose cycling is controlled by the action of glucokinase and G6PC2.	24
3.2 Glucose cycling in WT or <i>G6pc2</i> KO islets isolated from chow fed mice and incubated in 5 mM D7-glucose.....	30
3.3 Glucose cycling in WT or <i>G6pc2</i> KO islets isolated from high fat fed mice and incubated in 5 mM D7-glucose.....	32
3.4 Simulation of GSIS dose-response curve shifting in the linear range.	33
3.5 Glucose cycling in WT or <i>G6pc2</i> KO islets isolated from chow fed mice and incubated in 11 mM D7-glucose.....	34
3.6 Glucose cycling in WT or <i>G6pc2</i> KO islets isolated from high fat fed mice and incubated in 11 mM D7-glucose.....	35
3.7 Glucose methyloxime pentapropionate mass spectra from unlabeled and tracer glucose.	41

4.1 Model of hepatic glucose production during fasting	48
4.2 The dependence of each flux estimate on isotopomer measurements	50
4.3 The experimental timecourse	52
4.4 Relative isotopomer abundances over the experimental timecourse	53
4.5 Comparison of isotopic enrichment levels to [U- ¹³ C ₃]propionate dose.....	54
4.6 Comparison of flux estimates among infusion groups	55
4.7 Comparison of blood glucose and enrichment levels between fasting groups	59
4.8 Effect of fasting time on fluxes.....	61
4.9 The effect of CO ₂ recycling on flux estimates.....	63
4.10 A simplified model for estimating gluconeogenic-related fluxes using deuterated tracers	65
4.11 Comparison of GNG-related fluxes between simulated and fasting study data	66
4.12 ² H enrichment over the experimental timecourse	67
4.13 Comparison of simulated and measured MIDs.....	68
4.14 GNG-related flux estimates from simulated and measured data	68
4.15 Effect of hydrogen flux on the reduced model	70
A.1 The launched GUI with major components identified.....	77
A.2 Loading and visualizing NetCDF files.....	77
A.3 The method panel allows the user to load and edit an existing method or create a new method.....	78

A.4	The peak parameters (highlighted by a red box) can be viewed and edited manually by the user in the panel accessible from the Options menu or by right-clicking on a filename in the listbox	82
A.5	All calculated baselines can be visualized and edited in the Visualize and Adjust Baselines interface	83
A.6	The <i>File</i> menu	83
A.7	The <i>Options</i> menu	84
A.8	The <i>Find Peaks Options</i> interface allows the user to adjust the settings used in the algorithm to calculate noise and the baseline	85
A.9	The <i>gcms_scan</i> window allows the user to review the full MS scan at any timepoint in the chromatogram	87
A.10	An example of smoothing the raw, summed selected ion chromatogram using <i>mssgolay</i>	90
A.11	With <i>Add new peak</i> selected in the <i>Metabolite</i> menu, define the name of the new metabolite.....	94
A.12	Estimating relative intensities of main ion ranges using GUI plot tools	95
A.13	Screenshot of <i>integrate_gcms</i> output file in Excel.....	98
B.1	The launched <i>gpa</i> GUI	101
B.2	The GUI table is populated with sample names and ID numbers	103
B.3	The GUI axes display the sample MIDs for each fragment	103
B.4	Unlabeled control samples are used for weighting fragments in the LSQ regression	104
B.5	The active isotopomers in the model can be adjusted by the user	104
B.6	The user can activate specific isotopomers in the model using <i>Customize</i>	105

B.7 A click of the Run GPA button initiates the analysis.....	105
B.8 The first output file contains the fractional contribution values for each isotopomer.....	106
B.9 The second output file contains the total enrichment estimates (%) at each carbon position.....	107
B.10 After the analysis has completed, the minimized MIDs are plotted (fit) with the experimental values (data)	107
B.11 The INCA output details isotopomer abundances (H1-H6), average enrichment values (D1-D6), and an evaluation of the goodness-of-fit (SSR; 95% confidence intervals LB95 and UB95)	108
B.12 The Reset button is used to clear all data from the GUI.....	108
D.1 The initialized inca_batch GUI.....	111
D.2 The batch GUI with mod_test loaded. The box on the left-hand side displays the experiment names, while the box on the right-hand side displays a summary of the selected experiment.....	112
D.3 An Excel spreadsheet defines MIDs and measurement errors (SE) for each timepoint of each experiment.....	113
D.4 The batch GUI displays the imported experiments.....	114
D.5 The <i>Options</i> menu defines the batch protocol for data fitting	115

CHAPTER I

GENERAL INTRODUCTION

Glucose is the primary energy source for the majority of animal cells. The pathways of glucose metabolism are complex and interconnected. The complete oxidation of glucose to CO₂ requires two major pathways: glycolysis and the citric acid cycle (CAC). Glycolytic reactions take place in the cytosol and CAC reactions are compartmentalized in the mitochondria. Reducing equivalents produced during glucose oxidation are used in oxidative phosphorylation to produce ATP, the predominant intracellular energy molecule. Glucose can also be produced intracellularly through both glycogenolysis and gluconeogenesis (GNG). Glycogenolysis produces glucose from glycogen stores. GNG produces glucose from many different non-carbohydrate carbon sources. Lactate, glycerol, and gluconeogenic amino acids can all be used to generate glucose. Many of the same reactions of glycolysis and CAC are used in GNG.

In the whole animal, maintaining blood glucose homeostasis is vital to ensure that cellular energy needs are met. When blood glucose is high, insulin is released from the β -cells of the pancreas. Insulin signaling activates glucose uptake and utilization throughout the body. Liver and muscle cells clear excess glucose and store it as glycogen. Conversely, when blood glucose is low, glucagon is released from the α -cells of the pancreas. Glucagon activates glycogenolysis and GNG in hepatocytes. During fasting, the liver is primarily responsible for producing glucose to maintain blood glucose homeostasis, which ensures cellular energy needs are continuously met throughout the body. The regulation of glucose

homeostasis involves whole animal metabolism and, thus, necessitates the development of system-level approaches.

Glucose metabolism is carefully regulated. In addition to hormonal control, the rate of turnover of molecules – or *flux* – through each step in the pathway can be regulated by allosteric effectors, covalent modifications, substrate cycling, or by enzyme and substrate availability. Despite this complexity, metabolic pathway alterations are often inferred from changes in enzyme expression. For many enzymes, mRNA or protein abundances do not correlate with flux (13, 25). Flux analysis, which combines metabolite measurements with mathematical modeling, provides comprehensive information on the dynamics of carbon flow through a metabolic network.

Disruptions in normal glucose metabolism and homeostasis can cause or indicate disease. Changes in normal glucose metabolism are the hallmark of type 2 diabetes, a condition rising in prevalence and closely linked to the current obesity epidemic (14). In addition to diabetes, many cancer cells exhibit profound metabolic reprogramming. The Warburg effect is a common metabolic phenotype in cancer cells, whereby glycolytic flux and lactate production are significantly elevated in comparison to control cells (28). Characterizing glucose metabolism in cancer cells is used diagnostically, prognostically, and to evaluate treatment efficacy (28). In non-alcoholic fatty liver disease (NAFLD), abnormal accumulation of fatty acids in hepatocytes causes ER stress and mitochondrial dysfunction that alters CAC flux and induces oxidative stress (21, 45). Changes in glucose metabolism have been linked to many other diseases, from polycystic kidney disease (60) to sleep apnea (41) to Alzheimer's disease (17, 62). Because glucose metabolism is central to energy homeostasis and dysfunctional in many human disease states, the development

of sensitive, quantitative methods to characterize glucose metabolism is of vital importance.

Isotope labeling experiments are performed to quantitatively measure flux. *Stable isotopes*, which are naturally occurring isotopes with one or more extra neutrons, are often utilized as labels because they are less expensive, more stable, and safer to handle than radioisotopes. Labeling experiments generally require a higher concentration of stable isotopes than radioisotopes because of the natural, baseline abundance of stable isotopes in the environment. However, stable isotopes provide a richer data set than radioisotopes, which supports flux analysis. In these studies, ^2H and/or ^{13}C -labeled substrates, are introduced to a system (i.e. cells in culture or a laboratory mouse). Careful measurement of the labeling patterns of one or more intermediates or products of the metabolic network allows the flux through the pathways to be quantified. For many studies, the application of stable isotope tracers requires the accurate analysis of the number and position (or *positional enrichment*) of isotopes on the measured products. Because accurate positional enrichment is required, analysis is currently constrained to nuclear magnetic resonance (NMR) spectroscopy. NMR equipment costs, lengthy sample analysis times, large sample volume requirements, and low sensitivity are significant limitations to the application of stable isotope tracers.

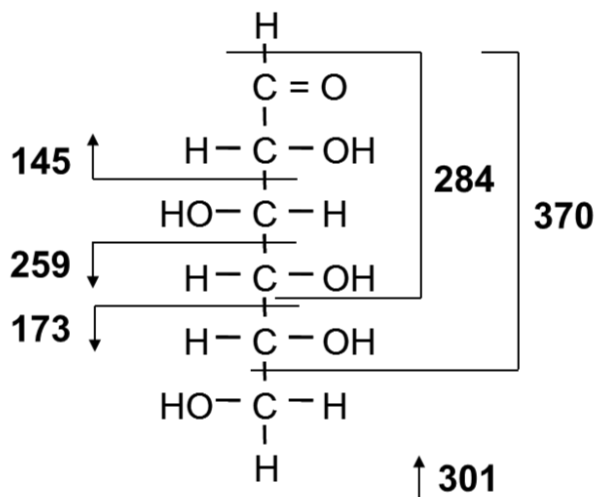


Figure 1.1

Positional enrichment analysis of glucose using overlapping GC-MS fragments. Six ions – m/z 145, 173, 259, 284, 301, and 370 – break up the parent glucose molecule into overlapping fragments that can be used to determine positional enrichment computationally.

Gas chromatography-mass spectrometry (GC-MS) can measure the mass shifts expected with stable isotope labeling. However, unlike NMR, GC-MS cannot readily perform positional enrichment analysis. The sensitivity of GC-MS, combined with the lower cost and higher throughput, make it desirable for stable isotope studies. Recently, a novel method for evaluating positional enrichment using GC-MS was published (4). This proof-of-concept showed that a combination of glucose derivatization, GC-MS, and linear regression could be used to precisely measure the positional enrichment of ²H on tracer glucose standards. The chemically distinct glucose derivatives elute at different times and fragment into unique ions. Evaluating the mass isotopomer distribution (MID) of six fragment ions provides overlapping information at each carbon position of the parent glucose molecule (Figure 1.1). Using least-squares (LSQ) regression, the fractional abundance of each of the 2⁷ possible hydrogen isotopomers of glucose can be estimated, and the total enrichment of ²H at each carbon position can be determined (Figure 1.2).

In this work, the GC-MS-based methodology was validated in biological samples and used to investigate biological systems. The second chapter details the validation studies and the creation of MATLAB-based user interface tools that improve the accessibility of the method. In the third chapter, the validated methodology is used to study glucose cycling in isolated mouse islets. Finally, in Chapter IV, the overlapping fragments are used with a metabolic network model to perform flux analysis *in vivo*.

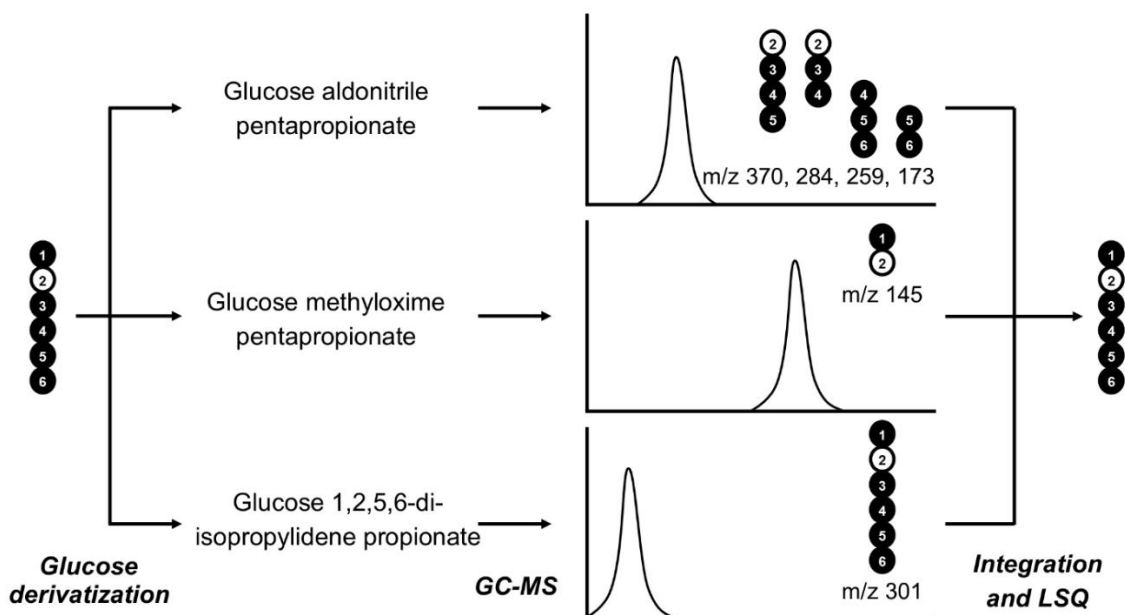


Figure 1.2

Overview of GC-MS-based positional enrichment methodology. Sample glucose isotopomers are derivatized three ways. Each derivative is distinct in structure and mass. The derivatives elute at different retention times and produce different ion fragments. The overlapping ion fragments are used to estimate the abundance of each of the possible 2^7 hydrogen isotopomers of glucose.

CHAPTER II

SAMPLE PROCESSING AND ANALYSIS OF GC-MS DATA

In all studies, glucose was derivatized, as described by Antoniewicz et al. (2), from biological samples. The three glucose derivatives were analyzed by GC-MS (Figure 1.2). The derivative peaks were integrated using a fixed-width, adjustable baseline algorithm (1) adapted into a MATLAB-based user interface. Integration produced MIDs for six ions of interest (Figure 1.1). The ions produced overlapping information for each carbon position of the parent glucose molecule. In studies shown here and in Chapter III, this overlapping information was used in a LSQ regression (2) to obtain positional enrichment estimates. In studies detailed in Chapter IV, the overlapping information was used with a network model to estimate metabolic fluxes. An overview of sample processing and data analysis is provided in Figure 2.1.



Figure 2.1

Overview of sample and data processing. Samples were collected from cell culture media or blood. Each sample was derivatized through three separate protocols. The samples were analyzed by GC-MS. Each derivative peak was integrated, and the resulting MIDs were used to perform positional analysis or metabolic flux analysis (MFA).

Preparation of glucose derivatives

Low sample volume requirements are a significant advantage of the methodology, especially for *in vivo* applications. Only 50 μL of cell culture media or blood plasma is necessary for analysis. In these studies, samples were divided into three aliquots, and each

was derivatized separately to obtain di-*O*-isopropylidene propionate, aldonitrile pentapropionate, and methyloxime pentapropionate derivatives of glucose.

Proteins were precipitated from 20 μL of sample using 300 μl of cold acetone, and the supernatant was decanted to a glass screw-cap culture tube. The supernatants were placed in a 60°C heating block and evaporated to dryness under air flow. 500 μL of a 1:46 sulfuric acid:acetone solution was added to each tube, and the samples were incubated at room temperature for 60 minutes. 400 μL of 0.44 mM sodium carbonate solution was added to neutralize the reaction. 1 mL of saturated sodium chloride and 1 mL of ethyl acetate were added to each tube. The tubes were shaken vigorously to mix and incubated 2 minutes at room temperature for phase separation. The top, organic layer was carefully transferred to a microcentrifuge tube using a glass Pasteur pipette. This layer was evaporated to dryness under air flow at room temperature. 150 μL of a 2:1 solution of propionic anhydride:pyridine was added to each tube, and the samples were incubated 30 minutes at 60°C. The samples were placed in a 60°C heating block and evaporated to dryness. The dried samples were resuspended in 100 μl of ethyl acetate and centrifuged 10 minutes at 14,000 rpm to pellet solid debris. The samples were then transferred to GC injection vials with 250 μl glass inserts for GC-MS analysis.

For both aldonitrile and methyloxime derivatization, proteins were precipitated from 10 μl of sample using 300 μl of cold acetone, and the supernatants were decanted to microcentrifuge tubes. The supernatants were placed in a 60°C heating block and evaporated to dryness under air flow. 50 μL of 2 wt% hydroxylamine hydrochloride in pyridine solution or 2 wt% methoxyamine hydrochloride in pyridine solution was added to each tube for aldonitrile and methyloxime derivatization, respectively. All samples were

incubated 60 minutes at 90°C. 100 µL of propionic anhydride was added to each tube, and the samples were incubated 30 minutes at 60°C. The samples were placed in a 60°C heating block and evaporated to dryness under air flow. The dried samples were resuspended in 100 µl of ethyl acetate, centrifuged to pellet solid debris, and transferred to GC injection vials with 250 µl glass inserts for GC-MS analysis.

GC-MS analysis

GC-MS analysis was performed using an Agilent 7890A gas chromatography (GC) System with an HP-5 ms (30 m x 0.25 mm x 0.25 µm; Agilent J&W Scientific) capillary column interfaced with an Agilent 5975C mass spectrometer (MS). For optimal signal-to-noise, injection volumes were varied between 1-5 µl with purge flow times between 30-60 seconds. Samples were injected into a 270°C injection port in splitless mode. Helium flow was maintained at 0.88 ml/min. For analysis of di-*O*-isopropylidene and aldonitrile derivatives, the column temperature was held at 80°C for 1 minute, ramped at 20°C/minute to 280°C and held for 4 minutes, then ramped at 40°C/min to 325°C. For methyloxime derivatives, the same oven program was used except the ramp to 280°C was 10°C/minute. After a 5 minute solvent delay, the MS collected data in scan mode from m/z 300 to 320 for di-*O*-isopropylidene derivatives, m/z 100 to 500 for aldonitrile derivatives, and m/z 144 to 260 for methyloxime derivatives.

Integration of glucose derivative peaks

The raw GC-MS data was converted from the proprietary ChemStation format to NetCDF using File Translator Pro (<http://www.sisweb.com/software/csw/gcmsfile.htm>).

Each derivative peak was integrated using a custom MATLAB function to obtain MIDs for six specific ion ranges: aldonitrile - m/z 173-176, 259-263, 284-287, 370-374; methyloxime - m/z 145-147; di-*O*-isopropylidene - m/z 301-321.

The fixed width-adjustable baseline integration algorithm proposed by Antoniewicz et al. (1) and adapted by the Young lab is unique in several ways. Traditional “peak picker” algorithms often identify peaks by finding local maxima using the first derivative method. This integration algorithm, however, relies on probabilities to identify the most likely peak. The method requires the analyst to provide accurate information on each metabolite of interest, similar to the information found in the NIST mass spectral library. Specifically, the user must input: estimated retention time; at least two main ions or main ion ranges; estimated relative abundance of each main ion. The algorithm first computes the probability that a metabolite peak is at a given time value based on the ratios of relative intensities of the main ions. Then, the probability that a metabolite peak is at a given time value is calculated based on the provided retention time. The most likely peak location is identified as the time value where the product of the probabilities is the greatest.

The peak start and peak end values are calculated from the selected ion chromatogram (SIC) made up of the sum of the main ions. The algorithm moves down the summed peak until the signal is equal to the baseline times a noise multiplier. The width of the peak is fixed and used in the integration of each mass isotopomer SIC. Using this strategy, data can be collected from low abundance mass isotopomers that do not have a clean peak. This component of the algorithm is key for analyzing biological samples, which contain many metabolite peaks and significant noise. The algorithm is robust against common artifacts like peak tailing and shouldering.

The computational time required for integration by this method was significantly lower than for built-in MATLAB peak finding functions, including findpeaks and mspeaks. In addition, Antoniewicz et al. (1) and our work showed that the algorithm provided more accurate MIDs than other methods.

One collaborator of the Young lab was manually integrating each metabolite peak in the mass spectrometer instrument software. By eye, the middle 70% of the peak was estimated, and the average intensity was calculated. The location of the baseline was estimated, and the baseline intensity was subtracted from the average peak intensity. I analyzed this data using the integration algorithm described above and by MATLAB's mspeaks function. To assess uncertainty, root-mean-square error (RMSE) was calculated by comparing the baseline MID of unlabeled metabolites in the sample to the theoretical MID computed from the known abundances of naturally occurring isotopes. The average maximum RMSE was $0.90\% \pm 0.10\%$ ($n=5$) by the manual method. Our integration algorithm produced MIDs with maximum RMSE that was not significantly different ($0.96\% \pm 0.13\%$) at a fraction of the time. mspeaks produced MIDs with significantly higher RMSE ($1.77\% \pm 0.38\%$).

Guided integration using `integrate_gcms`

A disadvantage of the GC-MS-based methodology is the extensive computation required. To improve the accessibility of the methodology, the computational methods were packaged into user-friendly interface tools in the MATLAB programming environment. The MATLAB-based tool **`integrate_gcms`** (Figure 2.2) identifies derivative peaks from a user-defined method file in an automated fashion on a batch of files, while

allowing the user to visually check and manually refine the peak start, peak end, and baseline. Integration of each peak produces a spreadsheet with MIDs for each ion range defined in the method. This tool has been tested in the Young laboratory and in collaborating labs. It has proven invaluable for stable isotope studies, allowing complete visualization of metabolite peaks and automated integration in a single tool. A full user manual is included in APPENDIX A.

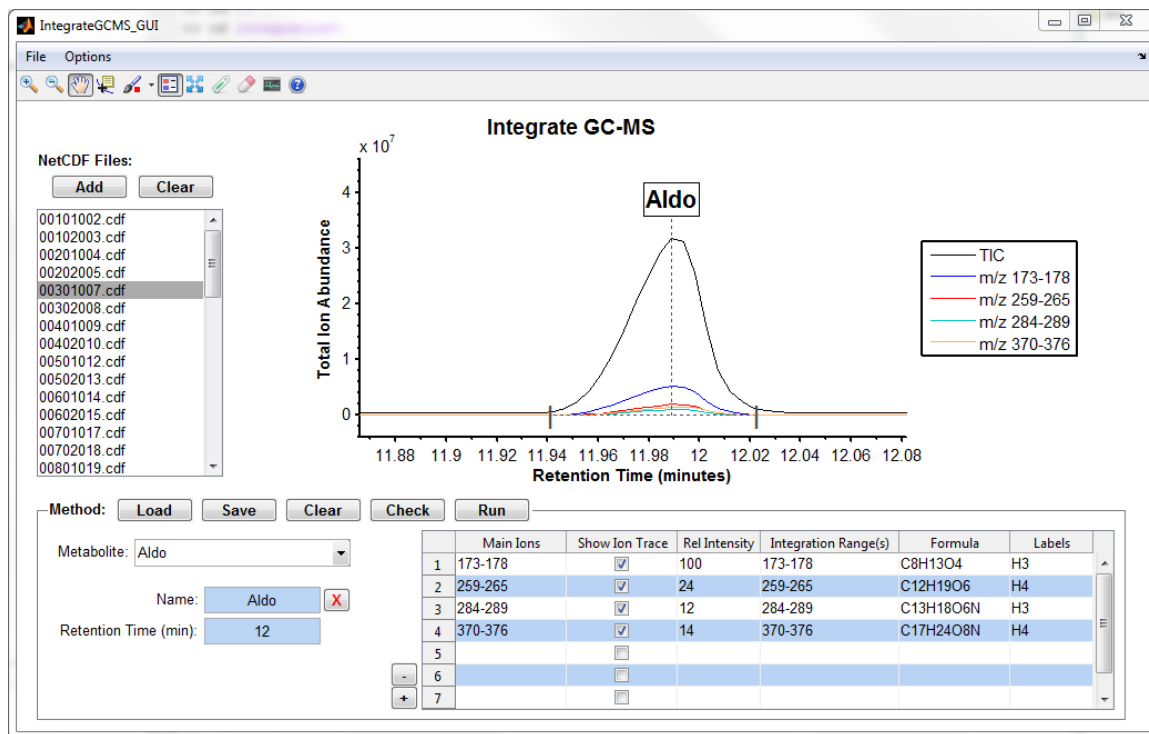


Figure 2.2
The `integrate_gcms` GUI guides a user through integration to produce MIDs.

Evaluation of the accuracy of fragment measurements from biological samples

Plasma samples from mice were collected, and the naturally labeled blood glucose was derivatized and analyzed by GC-MS. The measurement error associated with each glucose derivative fragment was evaluated by comparing the experimental MIDs to the

theoretical MIDs, based on the natural abundance of stable isotopes. The maximum RMSE was calculated by Equation 2.1:

$$\max \left(\sqrt{\frac{\sum_{i=1}^n (MID_M - MID_T)^2}{n}} \right) \quad (2.1)$$

where MID_M was the measured MID, MID_T was the theoretical MID, and n was the number of samples. It was expected that measurement error would be higher in biological samples than previously reported for pristine glucose standards ($\leq 0.3\%$, (4)). Indeed, in this study, the RMS error ranged from $\sim 0.4\text{-}1.0\%$ (Table 2.1).

Table 2.1
Maximum RMSE in fragment measurement from plasma samples.

Fragment (m/z)	Maximum RMSE (n=30)
145	0.63%
173	0.43%
259	0.38%
284	0.95%
301	0.79%
370	0.45%

Naturally labeled blood glucose was derivatized, and the derivatives were analyzed by GC-MS. The RMSE was calculated by comparing the experimental MIDs, obtained by integration, to the theoretical MID.

Positional enrichment analysis of glucose

In studies detailed in this chapter and in Chapter III, positional enrichment analysis (adapted from (4)) was performed using a LSQ regression. After integration of glucose derivative peaks, the six measured MIDs were linearly combined into a single vector in MATLAB (MID_M). The theoretical MIDs expected for each of the 128 possible hydrogen

isotopomers of glucose were calculated based on natural isotope abundances (8) and the atomic formula of each fragment. Theoretical MIDs were combined into a matrix, T . Multiplying T by a fractional contribution matrix, x , produced a vector of MIDs (MID_C) expected from the x -defined mixture of hydrogen isotopomers (Equation 2.2). The LSQ regression minimized the difference between MID_M and MID_C by manipulating x (Equation 2.3). The first output of the computational method is an estimation of the relative abundance of each hydrogen isotopomer in the sample. Multiplying this output, x , by a transformation matrix that defines each hydrogen isotopomer in terms of zeros, representing unlabeled carbons, and ones, representing labeled carbons, produces a second output that quantifies the total ^2H enrichment at each of the six carbon positions of glucose.

$$MID_C = T \times x \quad (2.2)$$

$$\min \sum (MID_C - MID_M)^2 \quad (2.3)$$

The effect of measurement error on enrichment estimates

The calculated RMSEs (Table 2.1) were used in simulation studies in MATLAB to determine the effect of measurement error on ^2H enrichment estimates. $^2\text{H}_2\text{O}$ is often used as a gluconeogenic tracer (43). In *in vivo* studies, the water of fasted animal subjects is supplemented with $^2\text{H}_2\text{O}$ and/or a bolus of $^2\text{H}_2\text{O}$ is administered to enrich body water to 4-5%. Singly labeled glucose molecules (M+1 isotopomers) are produced, predominantly with labeling at carbons 2 and 5. To simulate a biological sample from a $^2\text{H}_2\text{O}$ study, the expected MIDs (MID_C) for a mixture of M+1 glucose isotopomers, with fractional abundances defined in x , was calculated. For each fragment, measurement error was added

as random noise to the MID in 10 separate trials. The LSQ regression algorithm was used to estimate the ^2H enrichment at each carbon position. The enrichment estimates from MIDs without and with added measurement error were compared. With simulated measurement error, significant deviations from the expected values were reported. Significant overestimations were reported at positions 1, 3, and 6. Enrichment at carbons 2 and 5 were underestimated (*Method 1*, Table 2.2).

Table 2.2
Effect of measurement error on enrichment analysis of simulated biological mixtures.

	Mean Enrichment \pm SEM % ($n=10$)				
	Expected	Method 1	Method 2	Method 3	Method 4
C1	1.5	4.1 \pm 2.0	3.2 \pm 1.7	2.4 \pm 1.5	1.7 \pm 1.1
C2	6.0	4.3 \pm 2.3	5.3 \pm 2.4	4.6 \pm 1.6	5.9 \pm 1.1
C3	1.5	5.2 \pm 2.3	3.4 \pm 1.9	3.2 \pm 1.6	1.9 \pm 0.9
C4	1.5	1.8 \pm 0.7	2.1 \pm 1.4	1.6 \pm 0.5	1.3 \pm 0.8
C5	3.0	2.6 \pm 0.7	3.5 \pm 1.1	2.6 \pm 1.1	3.0 \pm 1.2
C6	0.5	1.5 \pm 0.4	0.8 \pm 0.4	0.6 \pm 0.5	0.5 \pm 0.4

MIDs were simulated assuming 1.5% [$1\text{-}^2\text{H}$]glucose, 6% [$2\text{-}^2\text{H}$]glucose, 1.5% [$3\text{-}^2\text{H}$]glucose, 1.5% [$4\text{-}^2\text{H}$]glucose, 3% [$5\text{-}^2\text{H}$]glucose, 0.5% [$6\text{-}^2\text{H}$]glucose, and 86% unlabeled glucose (**Expected**). Random measurement error was added. ^2H enrichment at each carbon was calculated using an unweighted (Method 1 and 3) or weighted (Method 2 and 4) LSQ regression. Methods 3 and 4 used a simplified model, reducing the number of possible hydrogen isotopomers from 128 to 8.

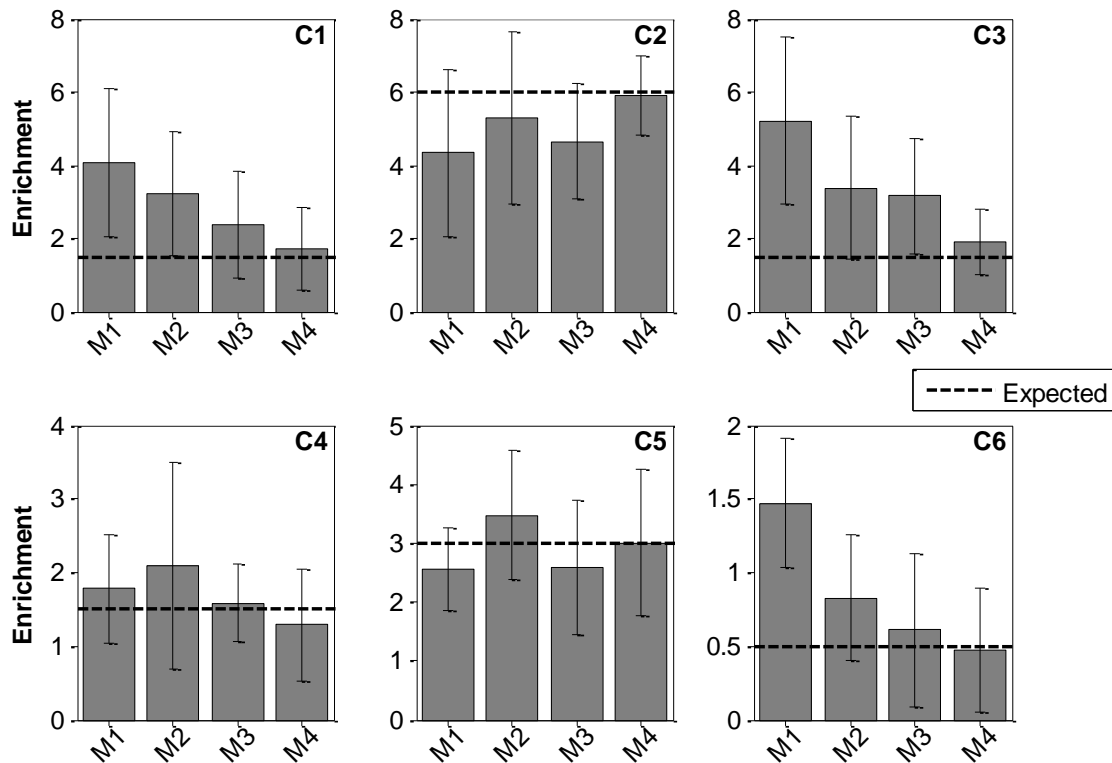


Figure 2.3

Effect of measurement error on enrichment analysis of a simulated biological mixture. MIDs were simulated assuming 1.5% [1-²H]glucose, 6% [2-²H]glucose, 1.5% [3-²H]glucose, 1.5% [4-²H]glucose, 3% [5-²H]glucose, 0.5% [6-²H]glucose, and 86% unlabeled glucose (**Expected**, dotted line). Random measurement error was added. ²H enrichment at each carbon position from carbon 1 (C1) to carbon 6 (C6) was calculated using an unweighted (Method 1 and 3) or weighted (Method 2 and 4) LSQ regression. Methods 3 and 4 used a simplified model, reducing the number of possible hydrogen isotopomers from 128 to 8. The x-axis abbreviates Methods 1-4 as M1-M4. The y-axis shows the average enrichment ± SEM % (*n*=10).

Performing a weighted LSQ regression, where the weights for each fragment were set as the inverse maximum RMSE, improved the accuracy of the estimation at carbon 2 and reduced erroneous enrichment estimations at carbons 1, 3, and 6 (*Method 2*, Table 2.2). The accuracy of the estimations was further improved by adjusting the number of possible hydrogen isotopomers of glucose in the model. For ²H₂O labeling studies, it can be assumed that glucose will be unlabeled or singly labeled; the probability of double labeling is low. Therefore, the number of possible hydrogen isotopomers in the model was reduced

from 128 to 8 (unlabeled glucose and 7 M+1 isotopomers). The estimations from the unweighted LSQ with the simplified model showed a reduction in enrichment at carbons 1 and 6 (*Method 3*, Table 2.2). With the simplified model, weighting improved the accuracy of the estimation at carbons 2 and 5 and further reduced erroneous estimates (*Method 4*, Table 2.2).

The effects of measurement error were overcome by weighting the fragments and by making assumptions to simplify the number of active isotopomers in the model. The simple mixture detailed in this example would not apply to every experiment. If a significant accumulation of M+2 isotopomers was observed in a $^2\text{H}_2\text{O}$ study, different assumptions would be applied, and the model would be simplified to 29 isotopomers (M+0, M+1, M+2). Extensive testing of the regression algorithm showed that, with adjustments, it is fully capable of producing accurate estimations of complex biological mixtures.

Automated glucose positional enrichment analysis

A tool for automated positional enrichment analysis was built in MATLAB that takes the integration output files as inputs (Figure 2.4). The tool averages technical replicates, calculates fragment error, and performs a weighted or unweighted LSQ regression. The hydrogen isotopomers active in the model are adjustable by the user. The tool outputs the relative abundance of each hydrogen isotopomer as well as the calculated total enrichment at each carbon position of glucose. To evaluate the confidence of the estimations, the comparison between MID_M and MID_C are presented to the user in a visual way. The complete user manual for this tool can be found in APPENDIX B.

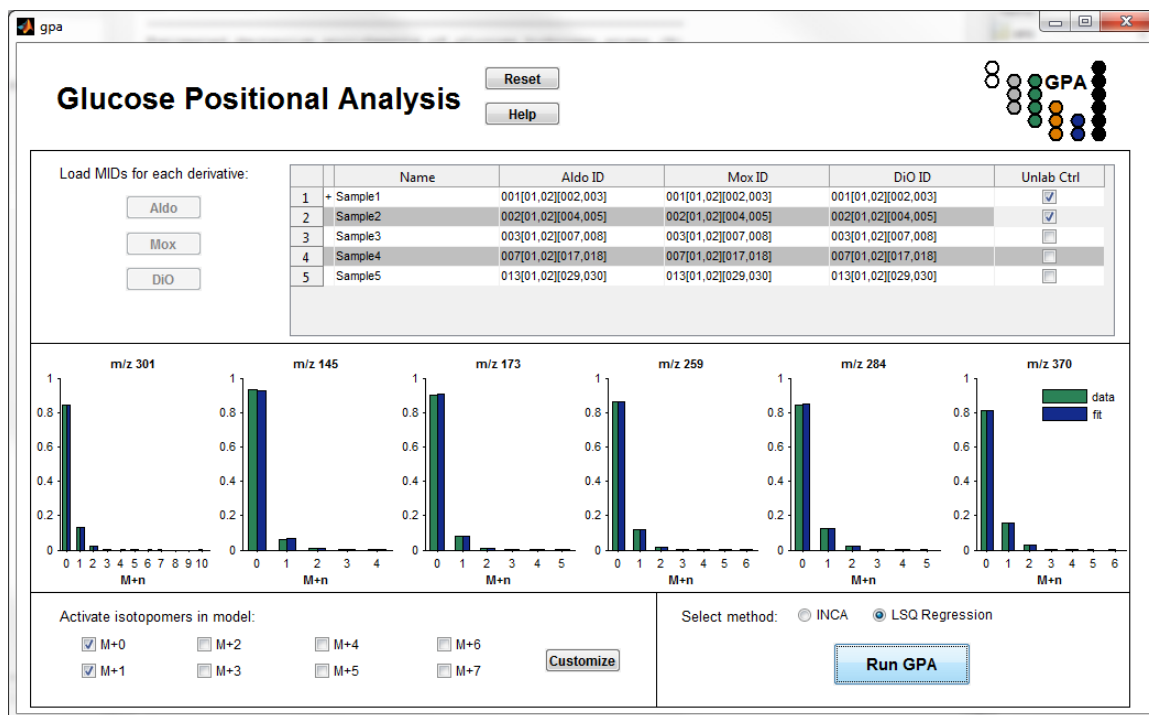


Figure 2.4
The gpa GUI automates positional analysis of glucose.

Conclusions and future directions

The six glucose derivative fragments necessary for positional enrichment analysis can be measured accurately from biological samples, with RMSEs less than 1%. While the measurement errors are low, they significantly impact positional enrichment estimates. Adapting the algorithm to weight fragments based on inverse RMSE and simplifying the number of isotopomers in the model improves estimates. Other computational approaches may also improve the robustness of the methodology. Experimental approaches, such as adding a solid-phase extraction (80), could be employed to partially purify glucose derivatives, remove contaminants, and improve RMSE.

Future studies should directly compare the refined GC-MS-based positional enrichment methodology with the gold standard method, NMR. The results of this comparison would reinforce the utility of the GC-MS-based method. For these studies, isotopic tracers (e.g. the tracer set described in CHAPTER IV) could be added to the media of isolated rat hepatocytes under gluconeogenic conditions. After a minimum of 8 hours, the labeled medium glucose could be analyzed by both GC-MS and NMR. This experimental design is advantageous because of the abundance of hepatocytes per isolation and the large volume of media per culture dish (~10 mL).

The induction of glucose production in isolated hepatocytes was successful in a pilot experiment without tracers (Figure 2.5). In this experiment, primary hepatocytes were isolated from rats. The cell count was quantified microscopically using a hemocytometer. The hepatocytes were purified and suspended in attachment media (DMEM) with 20 mM of glucose. Approximately five million cells were added to each 10 cm collagen-coated dish. After four hours, the attachment media was removed and replaced with a maintenance media containing 20 mM glucose. The cells were allowed to recover overnight. Then, the maintenance media was removed, and the attached hepatocytes were carefully washed and cultured in 10 mL of a 0 mM glucose gluconeogenic media with or without 10 nM of glucagon. After one hour, some dishes received the gluconeogenic precursors pyruvate (1 mM) and lactate (10 mM). 150 μ L media samples were obtained every two hours over 24 hours. The glucose concentration was assessed in duplicate using a YSI 2300 STAT PLUS analyzer.

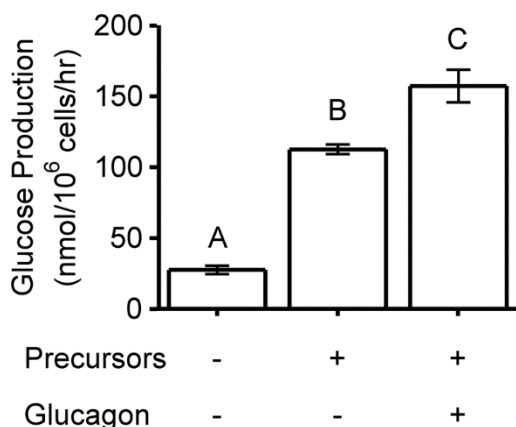


Figure 2.5

Glucose production in cultured hepatocytes under gluconeogenic conditions. Average glucose production (nmol/10⁶ cells/hr) \pm SEM ($n=3$) in primary hepatocytes incubated in glucose-free media for 8 hours with or without glucogenic precursors and glucagon. The glucose concentration was measured in duplicate using a YSI 2300 STAT PLUS analyzer. Letters indicate statistically separated groups, as determined by ANOVA and Tukey-Kramer.

The GC-MS-based methodology is much less time-intensive than the traditional NMR-based methodologies. User interface tools built for this project reduce analysis time and improve the accessibility of the computational-intensive method. However, method time can be reduced further. In all studies reported in this thesis, glucose derivatives were analyzed separately by GC-MS. In a pilot study, the derivatives were mixed 1:1:1 in a glass GC-MS vial. Clear derivative peaks were identified in the combination run (Figure 2.6), and accurate MIDs were obtained. An expanded study would confirm that accurate measurements can be obtained from derivative mixtures. Combining derivatives would reduce GC-MS run time by more than two-thirds.

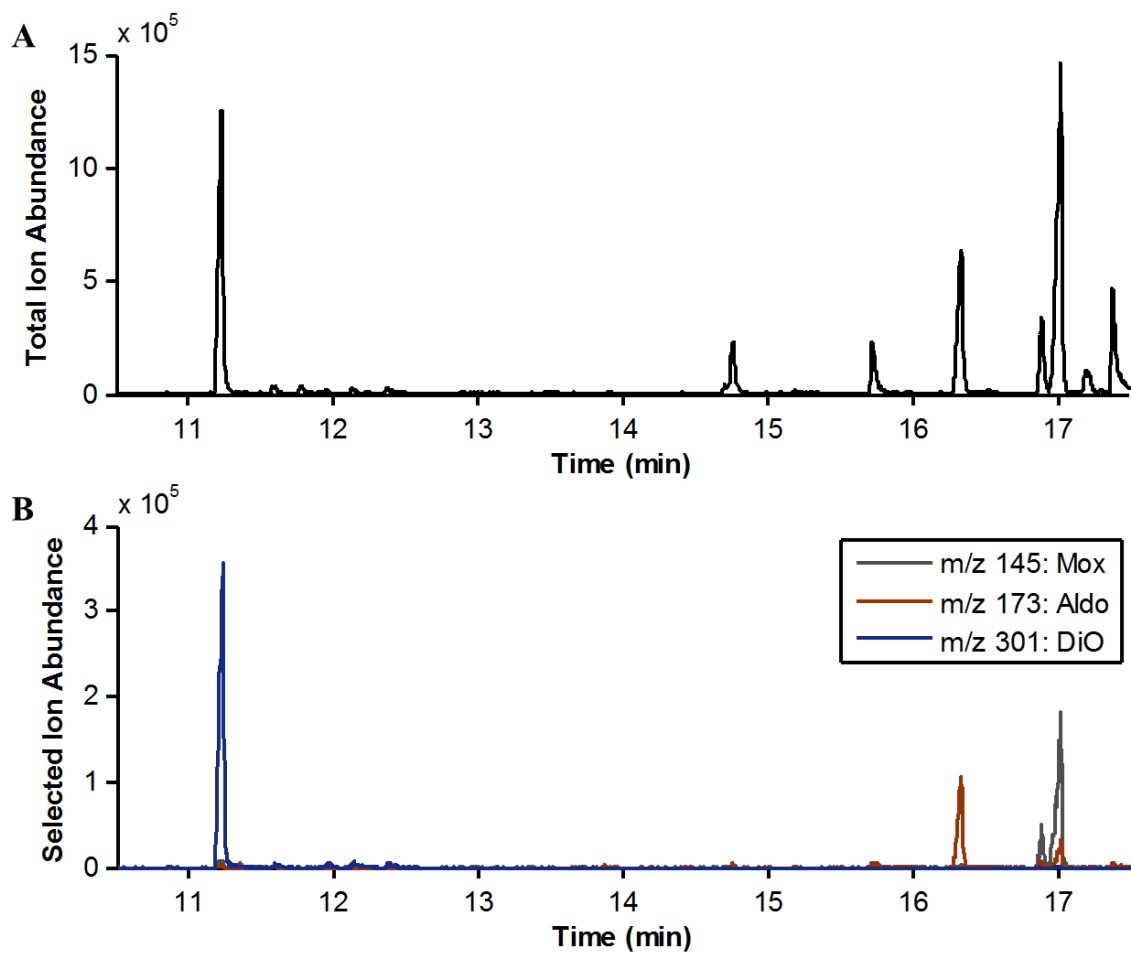


Figure 2.6

Chromatogram from a 1:1:1 mixture of glucose derivatives. (A) The total ion chromatogram for the analysis run shows many peaks in the expected time window. (B) The SICs from the main ion in each derivative reveals three clear peaks. m/z 145 was the main ion for the methyloxime pentapropionate (Mox) derivative of glucose (gray), m/z 173 for the aldonitrile pentapropionate (Aldo) derivative (red), and m/z 301 for the di-*O*-isopropylidene propionate (DiO) derivative (blue).

CHAPTER III
APPLICATION TO GLUCOSE CYCLING

The isolated mouse islet studies described in this chapter were published in *Diabetes* in 2015 (71).

Introduction

Glucose-6-phosphatase catalyzes the hydrolysis of glucose-6-phosphate (G6P) to glucose and inorganic phosphate (24, 29, 51, 69, 70). It exists as a multi-component system located in the endoplasmic reticulum (ER) and is comprised of several integral membrane proteins, namely a catalytic subunit (G6PC), a glucose transporter and a G6P/inorganic phosphate antiporter (24, 29, 51, 69, 70). Three G6PC isoforms have been identified, designated G6PC, G6PC2 and G6PC3 (29). Each isoform is encoded by a separate gene with a distinct pattern of tissue-specific expression (29). *G6PC* is predominantly expressed in liver where it catalyzes the final step in gluconeogenesis and glycogenolysis (24, 29, 51, 69, 70). *G6PC3*, also known as *UGRP* and *G6Pase-beta*, is ubiquitously expressed (11, 49). Mutations that reduce G6PC3 activity result in neutropenia, however, the physiological function of G6PC3 is unclear (12, 18). *G6PC2*, also known as *IGRP* (5, 48), is selectively expressed in pancreatic islet beta cells (54). G6PC2 is a major autoantigen in both mouse (26, 46, 52) and human (31, 75) type 1 diabetes.

Historically the question as to whether glucose-6-phosphatase activity is present in islets has been controversial, though it is now generally agreed that activity is detectable, but at a lower level than that found in liver (5, 24, 54, 55, 66). While a majority of studies agree that glucose-6-phosphatase activity exists in pancreatic islets, the issue as to whether

the level of activity is enough to affect glucose-stimulated insulin secretion (GSIS), and therefore be of biological significance, is currently unresolved. Matschinsky and colleagues (66) concluded that, while glucose-6-phosphatase activity is present in rat islets, the level of activity is not enough to result in sufficient G6P hydrolysis so as to affect GSIS. However, two caveats have subsequently arisen with respect to this conclusion. First, in contrast to all other vertebrate species examined (see <http://genome.ucsc.edu/>), *G6PC2* is a pseudogene in rats (48). Second, in various rat models associated with impaired glucose tolerance, *G6PC* expression is induced such that G6P hydrolysis would be elevated (38, 44, 68).

Several papers have also addressed the issue of G6P hydrolysis in mouse islets. Early studies suggested that, even though glucose-6-phosphatase activity is present in mouse islets, G6P hydrolysis does not occur (6). While seemingly counterintuitive, such a scenario would be possible if G6P entry into the ER lumen was blocked. However, later studies challenged this conclusion and showed that the measurement of G6P hydrolysis within islets is critically dependent on assay conditions (15, 36). More recently the O'Brien lab has shown that *G6pc2* accounts for the low glucose-6-phosphatase enzyme activity detected in mouse islets (57) and that a global knockout of *G6pc2* in mice on both a mixed (72) and pure C57BL/6J genetic background (57) results in a mild metabolic phenotype characterized by a ~15% decrease in FBG. These knockout mouse data are consistent with recent genome wide association studies (GWAS) showing that single nucleotide polymorphisms (SNPs) within the human *G6PC2* gene are associated with variations in FBG (10). Based on these observations, we hypothesize that *G6PC2* forms a futile substrate cycle with the beta cell glucose sensor, glucokinase (30, 50), and acts as a negative

regulator of basal GSIS by hydrolyzing G6P, thereby modulating beta cell glycolytic flux (57). Consistent with this model, a reduction in *G6pc2* expression results in a leftward shift in the dose response curve for GSIS, such that under fasting conditions blood glucose levels are reduced (57).

A major caveat with this model for the function of G6PC2 is the fact that estimates of glucose cycling obtained by radiotracer studies of pancreatic islets are very low (15, 36). Because the glucose-6-phosphatase activity of G6PC2 is ~40 fold lower than that of G6PC (57) and because G6PC2 also possesses a phosphatidic acid phosphatase domain (49), the possibility exists that G6PC2 influences GSIS through a mechanism independent of its ability to hydrolyze G6P. We have revisited this issue using an alternate, novel stable isotope methodology. With this approach, we can demonstrate much higher levels of glucose cycling in islets than previously reported. Importantly, glucose cycling is abolished in *G6pc2* KO mouse islets, suggesting that *G6pc2* modulates GSIS, at least in part, through its ability to hydrolyze G6P and thereby oppose the action of the beta cell glucose sensor, glucokinase (Figure 3.1).

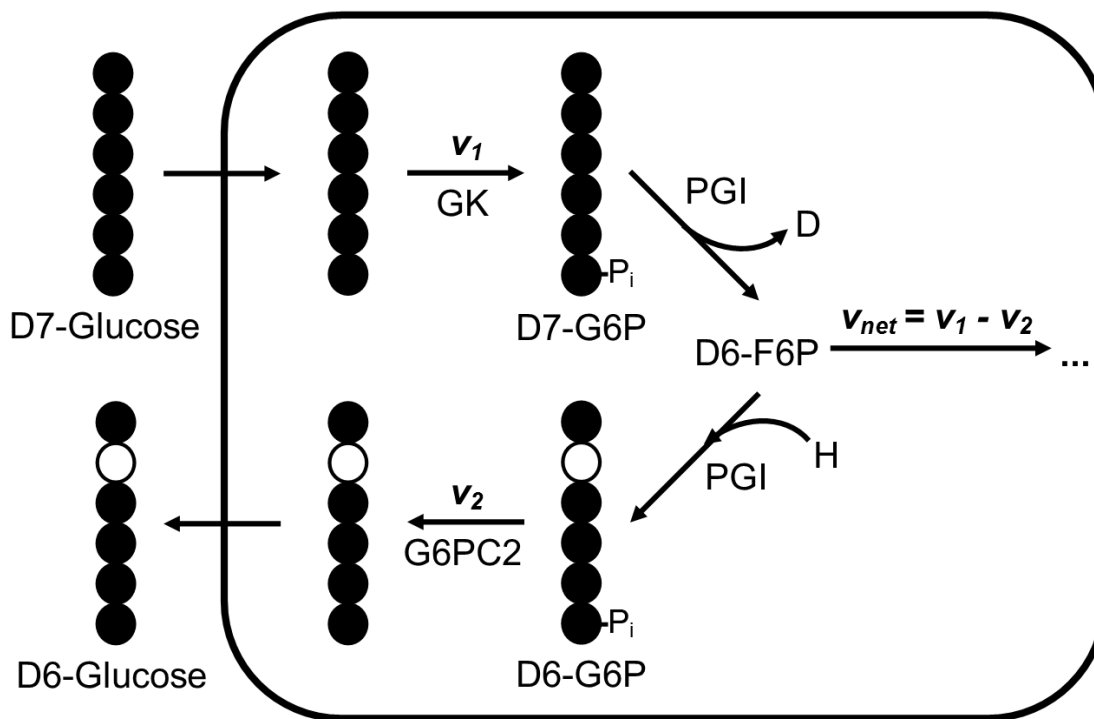


Figure 3.1

Glucose cycling is controlled by the action of glucokinase and G6PC2. Tracer glucose (D7-glucose) is converted to glucose-6-phosphate (D7-G6P) through the action of the enzyme glucokinase (GK) at rate v_1 . G6P is assumed to fully equilibrate with fructose-6-phosphate (F6P). The phosphoglucosomerase (PGI)-catalyzed isomerization of G6P to F6P results in exchange of hydrogen at the second carbon (C2) of G6P. Any deuterium at C2 derived from the D7-glucose tracer is replaced by an unlabeled hydrogen derived from water during the reverse isomerization reaction. The action of G6PC2 counteracts the activity of GK, converting G6P to glucose at rate v_2 . The rate of net uptake of glucose is denoted v_{net} , which is equal to v_1 minus v_2 . Black circles represent a carbon bound to deuterium, and white circles represent a carbon with hydrogen bound.

Experimental design

Animal care

The animal housing and surgical facilities used for this study meet the standards set by the American Association for the Accreditation of Laboratory Animal Care standards. The Vanderbilt University Medical Center Animal Care and Use Committee approved all protocols used. Prior to islet isolation, mice were maintained either continuously on a

standard rodent chow diet (calorie contributions: 28% protein, 12% fat, 60% carbohydrate (14% disaccharides); LabDiet 5001; PMI Nutrition International) or on a high-fat diet (calorie contributions: 15% protein, 59% fat, 26% carbohydrate (42% disaccharides); Mouse Diet F3282; BioServ) for 5-8 months. Food and water were provided ad libitum.

*Generation of *G6pc2* knockout (KO) mice*

The generation of *G6pc2* KO mice on a pure C57BL/6J genetic background has been previously described (57, 72).

Islet isolations

Islets were isolated from adult (8-12 months) male wild type and *G6pc2* KO mice as previously described (57). Isolated islets were incubated overnight in petri dishes in RPMI-1640 medium containing 11 mM glucose. Aliquots of ~100 islets were then transferred to 96 well plates and incubated for 24 or 72 hr in RPMI-1640 medium containing 5 mM or 11 mM glucose in a volume of 175 μ l. Islets were incubated in either naturally labeled glucose or [1,2,3,4,5,6,6-²H₇]glucose (D7-glucose) (98% isotopic purity per site; Cambridge Isotope Laboratories, Inc., Andover, MA, USA). Following the 24 or 72 hr incubation, islets were resuspended by pipetting and pelleted by centrifugation. The supernatant was retained for analysis of insulin content and glucose isotopomers, whereas the cell pellet was washed in PBS and then solubilized in passive lysis buffer (Promega) before quantitation of protein content using the Bio-Rad colorimetric protein assay.

Preparation of glucose derivatives

Derivatization was performed as described in CHAPTER II with one addition to the Di-*O*-isopropylidene propionate protocol. For this derivatization, 20 μ l of supernatant was mixed with 20 μ l of 5 mM [U- $^{13}\text{C}_6$; 1,2,3,4,5,6,6- $^2\text{H}_7$]glucose (Cambridge Isotope Laboratories, Inc., Andover, MA, USA), which served as an internal standard. The derivatization then proceeded as described previously to produce glucose 1,2,5,6-di-isopropylidene propionate.

GC-MS analysis

GC-MS analysis of the glucose derivatives was performed as described in CHAPTER II.

Estimation of total glucose concentration in the presence of deuterated glucose

Because enzymatic methods for glucose quantification are sensitive to kinetic isotope effects, we used a GC-MS-based method for quantification. The di-*O*-isopropylidene glucose peak was integrated over a mass range from m/z 301 ($M+0$) to 321 ($M+20$), and the ratio of the integrated ion counts of the glucose in the medium supernatant ($M+0$ to $M+10$) to the fully labeled [U- $^{13}\text{C}_6$; 1,2,3,4,5,6,6- $^2\text{H}_7$]glucose internal standard ($M+11$ to $M+20$) was determined. We used known glucose standards that were derivatized and analyzed alongside the experimental samples in each run to build a standard curve as shown in Equation 3.1,

$$\frac{[\text{Sample}]}{[\text{INSTD}]} = k \frac{\sum_{i=0}^{10}(M+i)}{\sum_{i=11}^{20}(M+i)} + b \quad (3.1)$$

where $[Sample]$ is the concentration of glucose in the supernatant sample, $[INSTD]$ is the known concentration of the internal standard, $(M + i)$ is the relative abundance of the i th mass isotopomer, k is the slope of the calibration curve, and b is its y-intercept. Cell-free evaporation controls were collected at 24 and 72 hours from replicate wells. The glucose concentration of these unlabeled samples was measured with a YSI 2300 STAT Plus Glucose & Lactate Analyzer. An evaporation correction factor was calculated by dividing the average concentration of the 72-hour cell-free controls by the average concentration of the 24-hour cell-free controls, and all 72-hour sample concentrations were divided by the correction factor.

Calculation of glucose uptake and cycling

Net glucose uptake (v_{net}) was calculated from the change in medium glucose concentration from 24 hours to 72 hours and expressed in picomoles/islet/hour using Equation 3.2,

$$v_{net} = \frac{C_{72} - C_{24}}{48 \text{ hrs}} \times \frac{V}{N} \quad (3.2)$$

where C_{72} is the extracellular glucose concentration at 72 hrs, C_{24} is the glucose concentration at 24 hrs, V is the liquid volume in each well (=175 μ L), and N is the number of islets in each well. The rate of glucose cycling (GC) was expressed as a percentage of glucose uptake v_2/v_{net} using an equation derived from the model illustrated in Figure 3.1.

Using the glucose concentration and relative isotopomer abundance measurements, GC was calculated according to Equation 3.3:

$$GC = \frac{v_2}{v_{net}} = \frac{y_{72} - y_{24}}{x_{72} - x_{24}} \quad (3.3)$$

where

$$y = \ln\left(\frac{A}{A+B}\right) \quad (3.4)$$

and

$$x = \ln(C) \quad (3.5)$$

In Equation 3.3, y represents the natural logarithm of the ratio of M+7 glucose abundance (A) to total M+1 through M+7 abundance ($A+B$) (Equation 3.4), and x is the natural logarithm of the glucose concentration C (Equation 3.5). The subscripts on x and y represent the time at which each measurement was taken. Equation 3.3 was applied to estimate GC by using the measured di-*O*-isopropylidene glucose MIDs, corrected for natural isotope abundance (23), to calculate the relative abundances B (m/z 302 to 307) and A (m/z 308). The derivation of Equation 3.3 is shown in APPENDIX C.

Calculation of positional enrichment

The MIDs of six ion fragments, m/z 145, 173, 259, 284, 301, and 370, derived from all three glucose derivatives were compiled into a matrix and compared to theoretical distributions using a custom least-squares regression program described in CHAPTER II (Figure 1.2). The program was used to estimate the relative abundance of each of the 128 possible hydrogen isotopomers of glucose.

Statistical analyses

Data were analyzed using a two-tailed Student's *t*-test: two sample assuming equal variance. The level of significance is indicated in the figure legends.

Quantification of glucose cycling in WT and *G6pc2* KO islets isolated from CF mice

During incubations with isolated islets, lower mass isotopomers of glucose would be expected to accumulate in the culture medium if a D7-glucose tracer is converted to D7-G6P through the action of glucokinase but is then converted back to D6-glucose through the action of *G6pc2* (Figure 3.1). To address this hypothesis, we incubated wild type (WT) and *G6pc2* knockout (KO) islets, isolated from CF mice, in the presence of 5 mM D7-glucose and measured the MIDs of medium glucose samples collected at 24 and 72 hours. We first examined the MIDs obtained from integrating the glucose 1,2,5,6-diisopropylidene propionate derivative peak, which preserves all 7 carbon-bound hydrogen atoms from the parent glucose molecule. After correcting for natural isotope abundance, we summed the relative abundances of the lower mass isotopomers from m/z 302 (M+1) to m/z 307 (M+6) and normalized them to the total labeled glucose signal from M+1 to M+7. The results show a significant accumulation of total M+1 to M+6 isotopomers in the incubation media from WT islets but no increase in the media from KO islets (Figure 3.2A).

Next, we examined the positional ^2H enrichment. Our model suggests that cycling of D7-glucose should result in accumulation of a specific M+6 mass isotopomer of glucose with deuterium replaced by hydrogen at the C2 position (i.e., $[1,3,4,5,6\text{-}^2\text{H}_6]\text{glucose}$). Least-squares regression analysis using mass isotopomer data obtained from three glucose derivatives (Figure 1.2) enabled us to calculate the ^2H enrichment at each carbon position of glucose in the culture media. This calculation confirmed that loss of deuterium at the C2 position of glucose from the fully labeled D7-glucose tracer accounted for the majority of the lower mass isotopomers that were formed in the media from WT islet incubations

(Figure 3.2B). Accumulation of the [1,3,4,5,6,6-²H₆]glucose mass isotopomer was not observed in the media from KO islet incubations (Figure 3.2B).

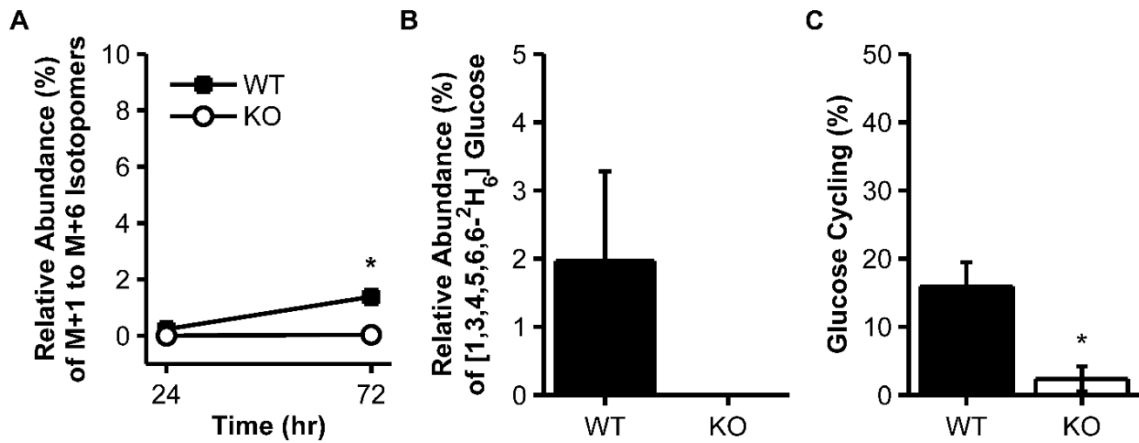


Figure 3.2

Glucose cycling in WT or *G6pc2* KO islets isolated from chow fed mice and incubated in 5 mM D7-glucose. *A*: The average relative abundance of lower mass isotopomers (M+1 to M+6) of the 1,2,5,6-di-isopropylidene propionate derivative fragment in the media from WT (black squares) or KO (white circles) islet incubations at 24 and 72 hours. The relative abundances are corrected for natural stable isotope labeling (23) and normalized to the total labeled glucose signal from M+1 to M+7. The average relative abundance of the 24-hour KO samples was baseline subtracted to correct for the isotopic purity of the D7-glucose tracer. In all experiments where tracer control samples were analyzed, the mass isotopomer distribution (MID) of the 24-hour KO samples was nearly identical to the MID of the pure D7-glucose tracer. *B*: The average estimated abundance \pm SEM of the [1,3,4,5,6,6-²H₆] glucose isotopomer with deuterium loss at C2 in the media from WT (black bar) or KO (white bar; all experiments reported zero abundance) islet incubations at 72 hours. *C*: Average glucose cycling \pm SEM, reported as a percentage of net glucose uptake. WT, 24 hours $n=4$; WT, 72 hours $n=4$; KO, 24 hours $n=4$; KO, 72 hours $n=4$ incubations of 100 islets. * $P < 0.05$ vs. WT.

Finally, using Equations 3.3-3.5, we calculated the rate of glucose cycling relative to net glucose uptake (Table 3.1) and found that WT islets exhibited cycling rates that were ~16% of the net uptake (Figure 3.2C). This is much higher than the 3% rate of glucose cycling previously reported by Khan et al. (37), who used a radiotracer method to quantify glucose cycling in islets isolated from CF mice and incubated in 5.5 mM glucose. In contrast, glucose cycling in KO islets was negligible (Figure 3.2C). Taken together, these

findings are consistent with our hypothesis that G6PC2 acts by hydrolyzing G6P, thereby opposing the action of glucokinase.

Quantification of glucose cycling in WT and *G6pc2* KO islets isolated from HFF mice

Both WT and *G6pc2* KO mice fed a high fat diet have a ~100 mg/dl elevation in FBG, though, as in CF mice, FBG remains ~20 mg/dl lower in *G6pc2* KO mice compared to WT mice (26). Based on this observation, we hypothesized that the rate of G6P hydrolysis (v_2) would be similar in CF and HFF mouse islets. To address this hypothesis, we applied our stable isotope method to islets isolated from HFF mice.

Consistent with our model for the action of G6PC2 on glucose cycling, M+1 to M+6 glucose isotopomers accumulated in the media between 24 and 72 hours in WT islet incubations only (Figure 3.3A). Further validation of the cycling model was provided by the positional ^2H enrichment results, which showed that the relative abundance of the [1,3,4,5,6,6- $^2\text{H}_6$] glucose isotopomer with deuterium loss at the second carbon was greater in the WT islet incubations compared to the KO islet incubations (Figure 3.3B). We again calculated the rate of glucose cycling relative to net glucose uptake. As expected, and consistent with the similar accumulation of M+1 to M+6 isotopomers observed in the HFF incubations (Figure 3.3A), the rate of G6P hydrolysis (v_2) was nearly identical between CF and HFF islets in 5 mM glucose (Table 3.1). Net glucose uptake (Table 3.1) and glucose cycling (Table 3.1) were not statistically different between CF and HFF islets. As in CF islets, glucose cycling was completely abolished in KO islets from HFF mice (Figure 3.3C).

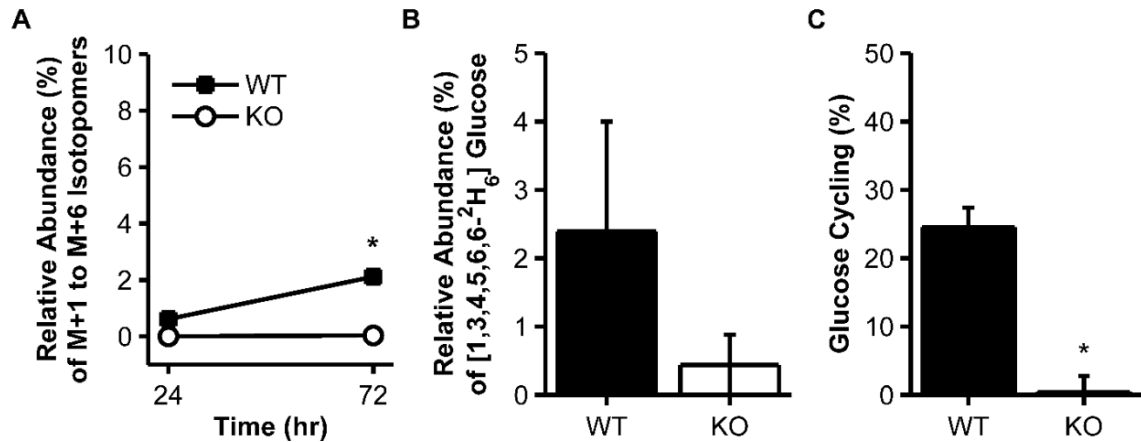


Figure 3.3

Glucose cycling in WT or *G6pc2* KO islets isolated from high fat fed mice and incubated in 5 mM D7-glucose. Panels A, B, and C show the same data as described in **Error! Reference source not found.**, but using islets obtained from high fat fed mice. WT, 24 hours $n=5$; WT, 72 hours $n=5$; KO, 24 hours $n=5$; KO, 72 hours $n=5$ incubations of 100 islets. * $P < 0.05$ vs. WT.

Quantification of the influence of extracellular glucose concentration on glucose cycling

An analysis of insulin secretion from perfused WT and *G6pc2* KO mouse pancreata suggests a parallel shift in the dose response curve for GSIS to the left in the KO pancreata when glucose increased from 5 to 11 mM (57). This parallel shift is indicative of a fixed rate of G6P hydrolysis (v_2), since v_1 should be the same in both WT and KO pancreata at the same glucose concentration with the difference in GSIS between the two curves being solely attributable to v_2 (Figure 3.4). This situation could arise if either transport of G6P into the ER lumen or hydrolysis of G6P to glucose by *G6pc2* was operating at V_{max} , the latter being supported by enzymatic studies (56). Based on this observation, we hypothesized that the rate of G6P hydrolysis (v_2) would be similar at 5 and 11 mM and that the glucose cycling rate (v_2/v_{net}) would be reduced in response to the expected increase in glucose uptake (v_{net}) at elevated glucose concentration. To address this hypothesis, glucose cycling was assessed at 11 mM glucose using islets isolated from CF and HFF mice.

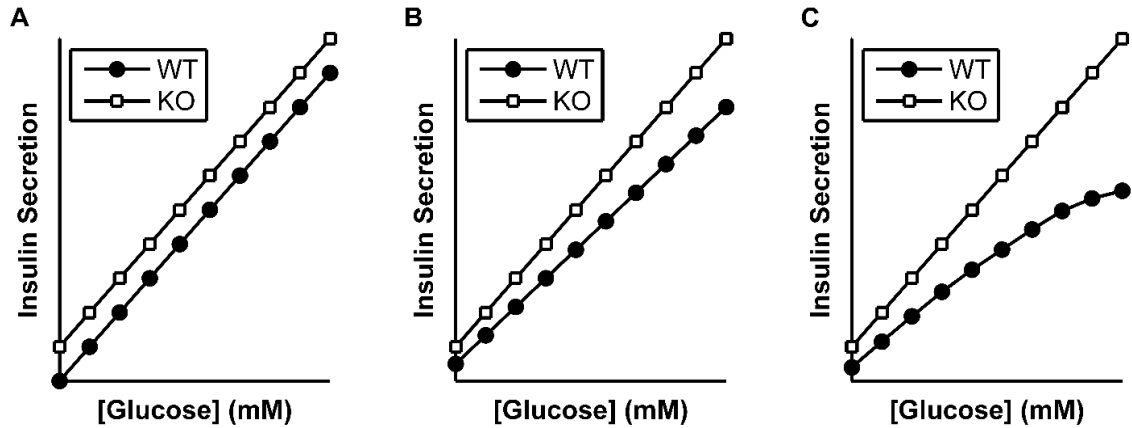


Figure 3.4

Simulation of GSIS dose-response curve shifting in the linear range. Total glucose uptake (v_1) is driven by the glucose sensor glucokinase and is assumed to be directly proportional to the glucose concentration (x-axis) and independent of genotype. In WT islets, the hydrolysis of G6P by G6pc2 (v_2) opposes v_1 and reduces glycolytic flux (v_{net}), which is equal to $v_1 - v_2$. In KO islets, v_2 is assumed to be zero and v_{net} is therefore equal to v_1 . v_{net} is assumed to be directly proportional to insulin secretion (y-axis). The simulation is based on the expectation that v_{net} should be greater in *G6pc2* KO islets at any given glucose concentration in the linear range. The experimental observation that v_{net} is the same for WT and *G6pc2* KO islets suggests that islets have adapted to prolonged culture. In (A), v_2 is fixed at a constant rate in the WT simulation and is set to zero in the KO simulation. The KO dose-response curve shifts parallel to the WT curve. Because v_1 and therefore v_{net} increases as the glucose concentration increases, the glucose cycling rate (v_2/v_{net}) decreases as glucose concentration increases. In (B), glucose cycling (v_2/v_{net}) is fixed at a constant value in the WT simulation and set to zero in the KO simulation. The KO dose-response curve shifts from the WT curve in a non-parallel manner, as the rate of G6P hydrolysis (v_2) increases with net glucose uptake (v_{net}). In (C), glucose cycling increases with glucose concentration, simulated by increasing v_2 over the glucose concentration range. The WT and KO curves diverge significantly at higher glucose concentrations, and the WT dose-response curve loses its linearity.

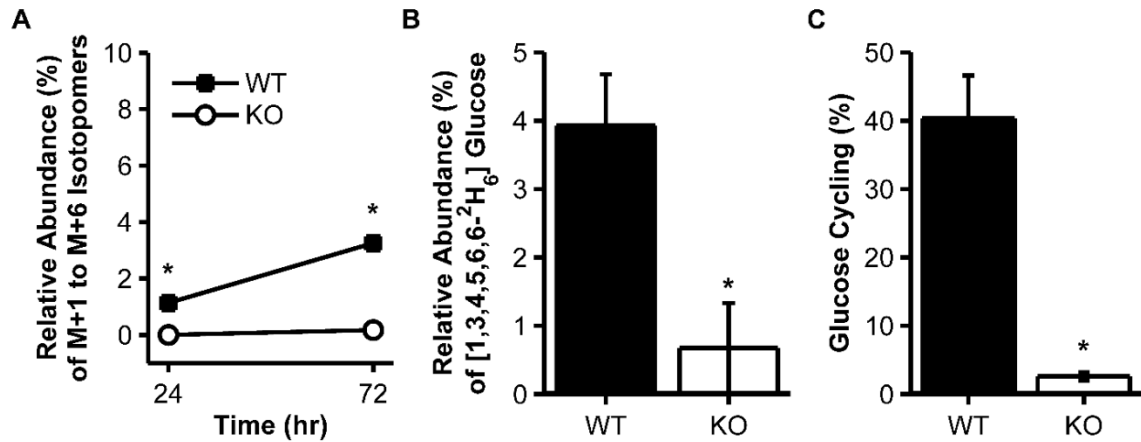


Figure 3.5

Glucose cycling in WT or *G6pc2* KO islets isolated from chow fed mice and incubated in 11 mM D7-glucose. Panels A, B, and C show the same data as described in **Error! Reference source not found.**, but using islets obtained from high fat fed mice. WT, 24 hours $n=5$; WT, 72 hours $n=5$; KO, 24 hours $n=4$; KO, 72 hours $n=4$ incubations of 100 islets. * $P < 0.05$ vs. WT.

If the rate of G6P hydrolysis (v_2) was similar in the 5 mM and 11 mM incubations, as hypothesized, the accumulation of M+1 to M+6 isotopomers of glucose in the medium would be similar. However, a significant increase in the accumulation of M+1 to M+6 isotopomers, consistent with an increase in G6P hydrolysis (v_2), was observed in CF (Figure 3.5A) and HFF (Figure 3.6A) islets. Even at the early 24 hour time point, the accumulation of M+1 to M+6 isotopomers in the media is significant in CF (Figure 3.5A) and HFF (Figure 3.6A) WT incubations, while the abundance of M+1 to M+6 isotopomers in KO incubations does not change from the baseline observed in the 5 mM glucose experiments (Figure 3.5A, Figure 3.6A). The accumulated M+1 to M+6 isotopomers in the WT media contain a significant abundance of the model-predicted [1,3,4,5,6,6-²H₆] glucose isotopomer with deuterium loss at the second carbon position, while this isotopomer is not present in the KO incubations (Figure 3.5B and Figure 3.6B). Unexpectedly, both CF and HFF WT islets exhibited increased cycling, relative to CF islets

in 5 mM glucose, driven by the significant increase in G6P hydrolysis (v_2), with rates quantified as ~35-40% of net uptake (Figure 3.5C and Figure 3.6C). Once again, the cycling in KO islets was negligible (Figure 3.5C and Figure 3.6C).

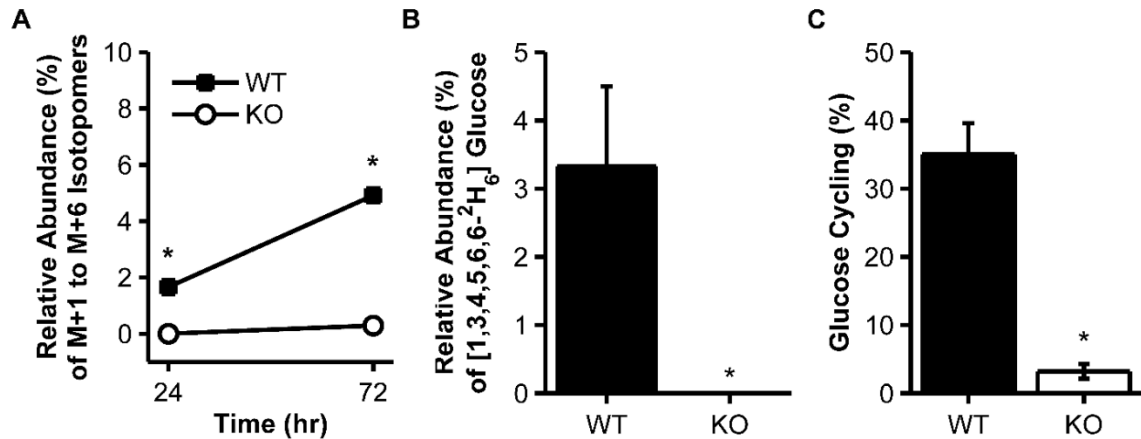


Figure 3.6

Glucose cycling in WT or *G6pc2* KO islets isolated from high fat fed mice and incubated in 11 mM D7-glucose. Panels A, B, and C show the same data as described in **Error! Reference source not found.**, but using islets obtained from high fat fed mice and incubated at 11 mM glucose. WT, 24 hours $n=7$; WT, 72 hours $n=7$; KO, 24 hours $n=7$; KO, 72 hours $n=7$ incubations of 100 islets. * $P < 0.05$ vs. WT.

Table 3.1

Comparison of glucose cycling and uptake among experimental groups

Diet	[Glc] (mM)	Rate of G6P Hydrolysis, v_2 (pmol/islet/hr)		Glucose Uptake, v_{net} (pmol/islet/hr)		Glucose Cycling (%) v_2/v_{net}	
		WT	<i>G6pc2</i> KO	WT	<i>G6pc2</i> KO	WT	<i>G6pc2</i> KO
CF	5	2.7 ± 0.4 (4) ^A	0.1 ± 0.3 (4)	18 ± 1 (4) ^A	14 ± 3 (4) ^A	16 ± 4 (4) ^A	2 ± 2 (4)
HFF	5	3.1 ± 0.1 (5) ^A	0.1 ± 0.3 (5)	14 ± 2 (5) ^A	14 ± 3 (5) ^A	25 ± 3 (5) ^{A/B}	0.5 ± 2 (5)
CF	11	11 ± 1 (5) ^B	0.9 ± 0.3 (4)	28 ± 4 (5) ^{A/B}	31 ± 5 (4) ^{A/B}	40 ± 6 (5) ^B	3 ± 1 (4)
HFF	11	14 ± 1 (7) ^B	1.2 ± 0.4 (7)	45 ± 8 (7) ^B	46 ± 9 (7) ^B	35 ± 5 (7) ^B	3 ± 1 (7)

Rate of G6P hydrolysis, glucose uptake and cycling results reported as mean ± SEM with the number of incubations indicated in parentheses. In each column, groups were compared by ANOVA. If at least one mean was significantly different, pairwise comparisons were performed by Tukey-Kramer. Statistically separated groups are indicated by letters.

Conclusions of isolated mouse islet experiments

This study describes a novel method for quantifying glucose cycling in isolated pancreatic islets that is based on the use of a stable D7-glucose tracer and the model presented in Figure 3.1. We applied this method to islets isolated from WT and *G6pc2* KO mice to investigate the role of G6pc2 in glucose cycling. In all WT islet incubations, a significant accumulation of M+1 to M+6 glucose isotopomers was observed over 72 hours (Figure 3.2A, Figure 3.3A, Figure 3.5A, and Figure 3.6A), and a specific, model-predicted D6-glucose isotopomer, [1,3,4,5,6,6-²H₆] glucose, accounted for most of the cycled glucose (Figure 3.2B, Figure 3.3B, Figure 3.5B, and Figure 3.6B), as determined by a custom least squares regression algorithm (Figure 1.2). Glucose cycling in WT islets varied with the assay conditions and was estimated to be 16 to 40% of net glucose uptake (Table 3.1). *G6pc2* KO islets took up glucose from the media at rates similar to WT islets (Table 3.1), but no accumulation of M+1 to M+6 glucose isotopomers was observed (Figure 3.2A, Figure 3.3A, Figure 3.5A, and Figure 3.6A), and glucose cycling was negligible (Table 3.1). These observations are consistent with our hypothesis that G6PC2 controls glucose cycling by opposing the action of glucokinase, thereby regulating glycolytic flux and ultimately GSIS. In this manner, G6PC2 may play an important role in the regulation of FBG, a hypothesis supported by GWAS data linking G6CP2 to FBG in humans (9, 10).

WT islets isolated from CF mice and incubated in 5 mM glucose cycled ~16% of the net glucose uptake (Figure 3.2). Previous studies using tritiated water quantified glucose cycling in isolated islets by measuring ³H incorporation at carbon 2 of derivatized glucose (37, 38). This method was not sensitive enough to quantify cycling in 3 hour, 5.5

mM glucose incubations using islets isolated from lean, WT mice, but based on extrapolation of data derived from *ob/ob* mouse islets, was used to estimate WT cycling rates at 3-4% of total uptake (37). While our novel method for measuring glucose cycling using stable isotopes requires longer incubation times, the simplicity and sensitivity are distinct advantages. Both the tritiated water method (37) and our method for measuring glucose cycling rely on the assumption that G6P and fructose-6-phosphate are in a rapid and complete equilibrium. However, hydrogen isotopes alter the kinetics of the PGI reaction such that equilibrium may not be complete. Nevertheless, previous work suggests the kinetic isotope effect of tritium reduces the V_{max} of the PGI reaction more than deuterium (47), which potentially makes our stable isotope method more accurate in applying this assumption. We expect that the rates of other reactions in our model, including the reactions catalyzed by glucokinase (v_1) and G6pc2 (v_2), would be minimally affected by the presence of either ^2H or ^3H tracers because they do not involve hydrogen transfer. Both methods only account for G6P molecules that are completely cycled out of the cell and subsequently accumulate in the culture medium. Therefore, the calculated rates of glucose cycling will underestimate the true cycling rate catalyzed by G6pc2 if some of the resulting glucose molecules are redirected toward an alternative intracellular fate and do not reappear in the extracellular medium.

To investigate the effect of diet on glucose cycling, islets were isolated from HFF mice. Similar increased rates of G6P hydrolysis were observed in CF and HFF islets when glucose was increased from 5 mM to 11 mM glucose (Table 3.1), consistent with our previous observation that the difference in FBG between WT and G6pc2 KO mice is similar on both diets despite elevated FBG in the HFF groups (37). Interestingly, previous

studies reported a significant increase in glucose cycling in islets isolated from obese *ob/ob* mice relative to WT (15, 36, 37, 39, 40). Kahn et al. (39) showed that this increase was not due to hyperglycemia, which is characteristic of *ob/ob* mice. However, whether hyperlipidemia or the absence of leptin signaling influence glucose cycling in *ob/ob* mice is unclear. Furthermore, the magnitude of this previously reported enhancement of glucose cycling in *ob/ob* mouse islets could, in part, be due to the underestimation of cycling in lean, WT mice.

Our method requires 72 hr islet incubations in order to enrich the medium in lower mass isotopomers of glucose for quantification. Over this time period in non-physiological conditions, the data suggest that the islets are losing some of their in vivo characteristics. *G6pc2* KO mice have a significantly lower FBG than their WT littermates (57), and consistent with this finding, isolated KO islets exhibited increased glycolytic flux (data not shown) and insulin secretion (57) in acute assays. However, after 72 hr in culture, insulin secretion between the WT and KO islets normalizes such that the concentration of insulin in the medium is not significantly different between WT and KO islets. In addition, the estimated net uptake rate of glucose between 24 and 72 hours in WT and *G6pc2* KO islets is equivalent (Table 3.1). While these glucose uptake data are consistent with the insulin secretion data (data not shown), the acute insulin secretion assays predict increased glucose uptake in *G6pc2* KO relative to WT islets. Similarly, a surprising elevation in the rate of G6P hydrolysis was observed in CF and HFF islets incubated in 11 mM glucose (Figure 3.5A and Figure 3.6A, Table 3.1). This observation is at odds with perfused pancreas data showing a parallel, leftward shift in the dose response curve for GSIS in CF *G6pc2* KO mice (26). In combination, these observations suggest that the islets are undergoing

adaptation during the long assay incubation. We hypothesize that the KO islets adapt to the absence of G6pc2 by reducing glucose uptake, which would make biological sense in that elevated glucose metabolism has been shown to be toxic to beta cells (19). We also hypothesize that the ability of glucose to stimulate G6pc2 expression (56) may explain the increase in v_2 . This induction would not have been a factor in acute insulin secretion experiments, given their short time course. Addressing these hypotheses and the molecular mechanisms behind islet adaptation to prolonged culture are clearly of interest and will be the subject of future experiments. Given these apparent effects of the long incubation time and any limitation in gas exchange in the 96 well plates used for the assay, future work will focus on using microfluidic devices specifically designed for islet culture (20, 59) allowing the media volume, and thus the time in culture, to be reduced. Such experiments would also reveal whether the significant increase in glucose uptake at 11 mM in HFF islets but not CF islets (Table 3.1) is also an artifact of the long incubation times.

In conclusion, the data presented in this study suggest that glucose cycling in WT islets is greater than previously reported and that G6pc2 is responsible for this cycling. These findings are consistent with the GWAS studies linking G6PC2 to regulation of FBG (9, 10, 16).

Future directions

Revise experimental design to remove m/z 145 fragment contamination

We chose D7-glucose as the tracer in the glucose cycling experiments so that all major cycling products could be identified in an unbiased manner. Our studies support the hypothesized model (Figure 3.1). The only significant cycling product that accumulated in the media was [1,3,4,5,6,6-²H₆]glucose. The positional analysis methodology successfully

measured the abundance of this specific cycling product. However, the error associated with these measurements was significant. Further analysis revealed that the m/z 145 fragment from the glucose methyloxime pentapropionate derivative was contaminated by a lower mass fragment that shifts into the analytical range.

In unlabeled glucose, the major ion in the methyloxime derivative is m/z 145 (Figure 3.7A). Lower mass ions m/z 141 and m/z 142 are present but do not significantly interfere with the MID of m/z 145. The methyloxime fragment from D7-glucose shifted from m/z 145 to m/z 147 as this fragment contained two ^2H (Figure 3.7B). m/z 146 is present at significant abundance due to the inherent impurity of the tracer. The m/z 141 and 142 ions present in the unlabeled spectra were not present in the spectra from D7-glucose. We hypothesized that m/z 141 shifted to m/z 143 and that m/z 142 shifted to m/z 145. The relative abundance of m/z 145 is far more significant than expected. Computational fragment analysis (73) predicted that the m/z 142 ion contains carbons 3, 4, and 5. While not conclusive, analysis of the methyloxime derivative from [1,2- $^{13}\text{C}_2$]glucose showed the mass shift to m/z 147 expected from the main ion with no change in the relative abundances of m/z 141 and m/z 142 (Figure 3.7C). Future studies could use a customized, lower enrichment tracer to eliminate the interference from m/z 142 at the risk of losing the ability to identify all potential cycling products. Computational correction methods could also be pursued, or a different derivatization method could be sought to identify a different fragment consisting of the same two carbons.

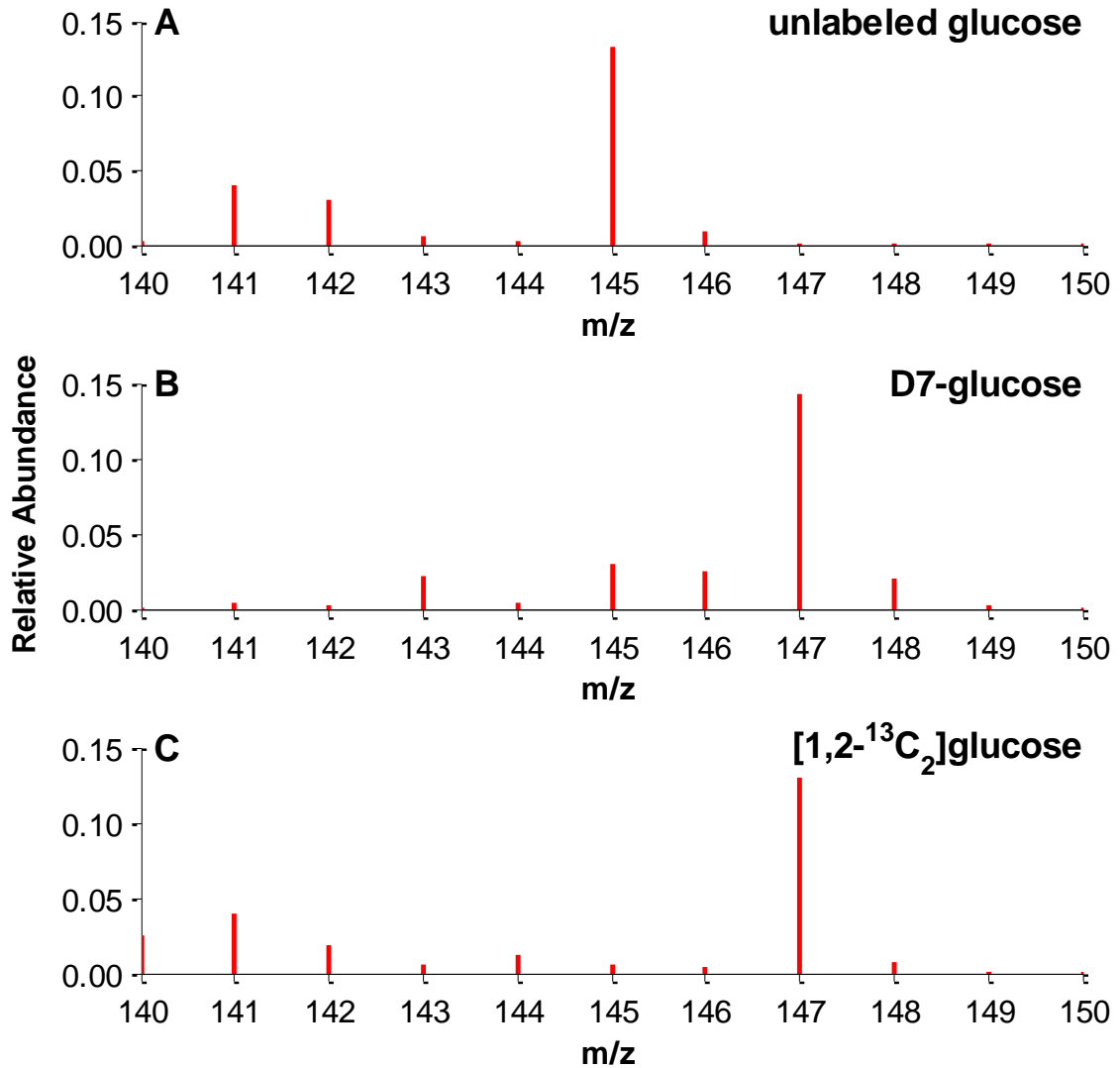


Figure 3.7
Glucose methyloxime pentapropionate mass spectra from unlabeled and tracer glucose.

Determine the effect of glucocorticoid treatment on glucose cycling

Multiple glucocorticoid response elements (GREs) are present in the promotor region of *G6PC2* (42). Previous work showed insulin secretion was significantly reduced and *G6pc2* activity was significantly elevated in isolated islets from glucocorticoid-treated *ob/ob* mice compared to untreated *ob/ob* mice (32). Similar results were reported for transgenic mice overexpressing the glucocorticoid receptor, increasing the glucocorticoid

sensitivity of isolated islets (39). We hypothesize that glucose cycling will increase in response to glucocorticoid treatment and that our sensitive methodology will be able to quantify this increase in islets isolated from CF WT mice. We further hypothesize that no increase in glucose cycling will be observed in islets isolated from treated *G6pc2* KO mice.

Investigate glucose cycling in isolated human islets

The isolated islet studies described above provide strong evidence that G6pc2 can modulate GSIS by cycling glucose in mice. We hypothesize that human G6PC2 has a similar functional role. GWAS studies support this hypothesis (9, 10, 16). To test this hypothesis, isolated islet incubations will be performed, as described above, in collaboration with the laboratory of Dr. Alvin Powers, the Integrated Islet Distribution Program, and the Human Islet Research Network. Human islets will be tested from a variety of donors. A normal range of glucose cycling from healthy, adult donors will be determined. Then, it will be determined if glucose cycling is aberrant in islets from donors who had type 2 diabetes. Glucose cycling rates will be correlated with GSIS (7, 35) and with G6PC2 activity (42).

In a pilot study, human islets isolated from non-diabetic donors were incubated in D7-glucose. Initially, samples were obtained at 24 and 48 hours, as in the isolated mouse islet studies. However, over this time period, glucose was almost completely depleted from the media, suggesting that the human islets are more metabolically active than the mouse islets. The protocol was revised to sample at 6 and 12 hours. Cycling and uptake were calculated as described above.

The accumulation of lower mass isotopomers of glucose was obvious over time in the human islet samples, strongly supporting our hypothesis that G6PC2 is cycling glucose in human islets. Positional analysis supported the model of cycling, although more work is needed for confirmation. Significant variability was observed among the islets (Table 3.2). The effect of glucose concentration was not clear from the limited number of samples. Genetic differences may account for the variability. We also believe that cycling and uptake may trend with the islet profiles identified by Powers and colleagues (35); the secretory profile number was included in the preliminary data shown in Table 3.2. Additional experiments are necessary to understand the variability.

Table 3.2
Glucose cycling in isolated human islets.

	Experiment 1	Experiment 2	Experiment 3	Experiment 4	Experiment 5	Experiment 6
[Glc] (mM)	5	11	5	11	5	11
Cycling (% of v_{net})	13.0	25.4	5.2	4.9	7.8	10.7
v_{net} (pmol/islet/hr)	20.3	20.1	29.3	62.1	19.7	27.5
Secretory profile	1	4	4	1/2	28.2	63.7
				3	15.4	23.5
				3	4	4
				3	4	1

Measure ^2H labeling in intracellular metabolites to validate model

The model of glucose cycling detailed in Figure 3.1 may be too simple to capture the dynamics of glucose flux and cycling. Because we only measure the accumulation of extracellular glucose cycling products, the measurements may underestimate the true cycling rate. Alternatively, intracellular metabolite extraction and the measurement of ^2H labeling (21, 22, 53, 67) may be required to understand how D7-glucose is utilized and to quantify the flux through G6PC2.

CHAPTER IV
APPLICATION TO METABOLIC FLUX ANALYSIS

Portions of the work described in this chapter were published in *The American Journal of Physiology – Endocrinology and Metabolism* in 2015 (27).

Introduction

Several NMR-based methods for phenotyping hepatic glucose production *in vivo* utilize three stable isotope tracers: ^2H or ^{13}C -labeled glucose, $^2\text{H}_2\text{O}$, and $[\text{U-}^{13}\text{C}_3]\text{propionate}$ (34). Each tracer serves a distinct purpose. $[\text{U-}^{13}\text{C}_3]\text{propionate}$ labels CAC metabolites and $^2\text{H}_2\text{O}$ labels intermediates of GNG. The glucose produced by the liver therefore has a distinct labeling pattern that is carbon-source and pathway dependent. The ^2H or ^{13}C -labeled glucose is infused at a constant rate and acts as an internal standard, allowing for the calculation of absolute flux rates. This three tracer methodology has been used to quantify CAC and GNG fluxes in fasted rats (32, 33), humans (65), and, to a limited extent, mice (61). However, the sensitivity limitations of NMR prevent the widespread application of this technique to the mouse. The large plasma blood volumes required for NMR analysis inflicts stress that disrupts metabolism and obviates replicate sampling. We hypothesized that the six glucose derivative fragments (Figure 1.1) would provide sufficient information for flux analysis. The lower volume requirements make the GC-MS-based method easily applicable to the mouse. The tool significantly enhances the ability to assess *in vivo* hepatic metabolism in wild-type and transgenic mice as well as in mouse models of human disease.

Modeling hepatic glucose production in INCA

A model of hepatic glucose production (Figure 4.1) was constructed using the INCA software package (33) (accessible at <http://mfa.vueinnovations.com/mfa>). The hydrogen and carbon transitions were defined for each reaction (Table 4.1). The model is based on the reaction network of Jones et al. (34) and assumes: (A) full equilibration of four-carbon intermediates in the CAC; (B) complete equilibration between glucose-6-phosphate (G6P) and fructose-6-phosphate (F6P) by phosphoglucosomerase (PGI); (C) complete equilibration between glyceraldehyde-3-phosphate (GA3P) and dihydroxyacetone phosphate (DHAP) by triose phosphate isomerase (TPI); (D) no entry of labeled carbon from acetyl-CoA; (E) no re-entry of CO₂ formed in the reaction network. The model consisted of 19 biochemical reactions (Table 4.1), 22 metabolite nodes, and 424 mass isotopomer balance equations. Metabolites with equivalent atoms were defined (Table 4.2). A description of the mathematical modeling approach applied to these studies is provided in APPENDIX E. The MIDs obtained from integration of GC-MS ion traces were imported into INCA. The flux through each reaction was estimated (Figure 4.2), relative to V_{CS} , by minimizing the sum-of-squared residuals (SSR) between simulated and experimental data. Flux estimates were repeated 25 times from random initial values. Goodness-of-fit was assessed by a chi-square test with 22 degrees of freedom (i.e. the regressions were overdetermined by 22 measurements). 95% confidence intervals were computed by evaluating the sensitivity of the SSR to variations in the flux values. The relative fluxes were converted to absolute fluxes in $\mu\text{mol/kg/min}$ using the known [6,6-²H₂]-glucose infusion rate (V_{INF} , Figure 4.1), and the mouse weights were used to convert fluxes to $\mu\text{mol/min}$.

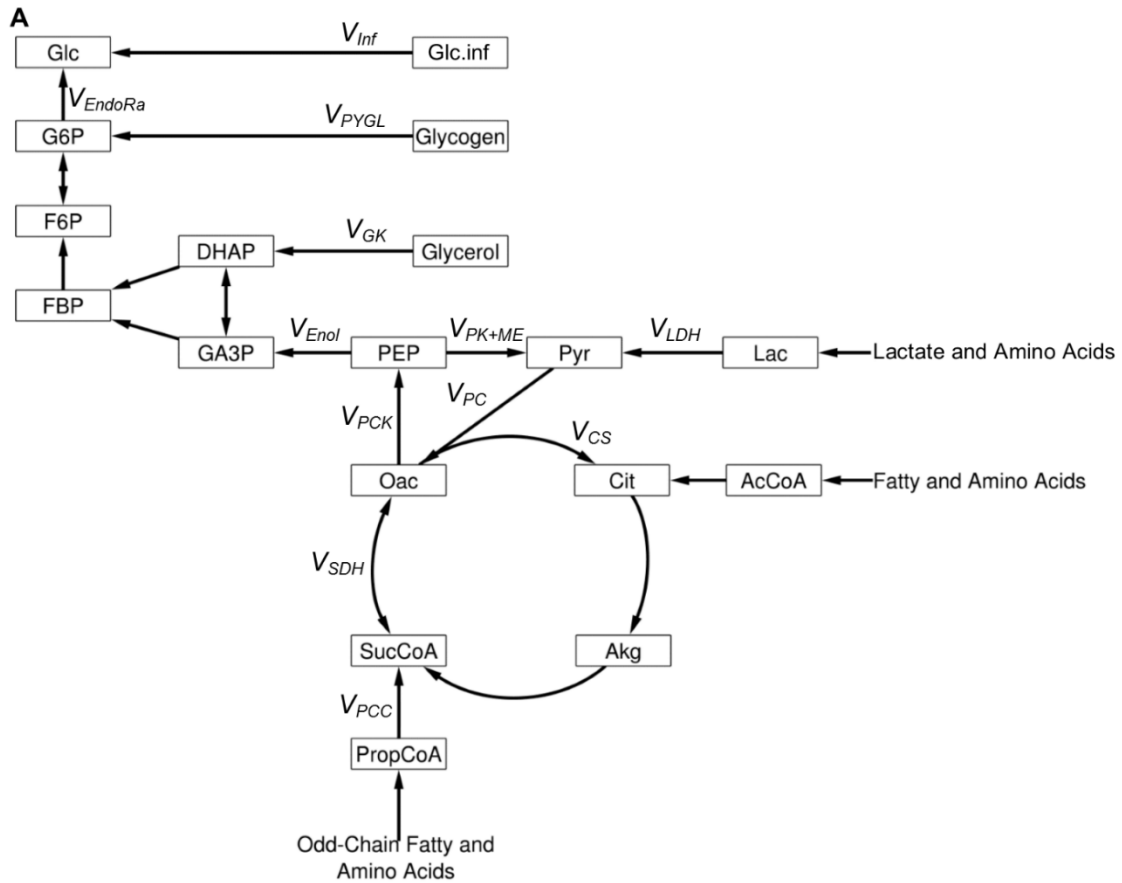


Figure 4.1

Model of hepatic glucose production during fasting. ^{13}C from $[\text{U-}^{13}\text{C}_3]$ -propionate enters the citric acid cycle as succinyl-CoA (SucCoA) at rate V_{PCC} . Lactate, amino acids, fatty acids, glycerol, and glycogen are also modeled as carbon sources for glucose production. ^2H incorporation from $^2\text{H}_2\text{O}$ occurs during gluconeogenesis. The rate of glucose production is estimated as V_{EndoRa} . $[6,6\text{-}^2\text{H}_2]$ -glucose (Glc.inf) is infused at rate V_{INF} .

Key: Endogenous glucose production (V_{EndoRa}), infusion of $[6,6\text{-}^2\text{H}_2]$ -glucose (V_{INF}), flux from glycogen to glucose-6-phosphate (G6P) (V_{PYGL}), glycerol to dihydroxyacetone phosphate (DHAP) (V_{GK}), phosphoenolpyruvate (PEP) to glyceraldehyde-3-phosphate (GA3P) (V_{ENOL}), oxaloacetate (Oac) to PEP (V_{PCK}), pyruvate (Pyr) to Oac (V_{PC}), Oac and acetyl-coA (AcCoA) to citrate (Cit) (V_{CS}), propionyl-CoA (PropCoA) to succinyl-CoA (SucCoA) (V_{PCC}), SucCoA to Oac (V_{SDH}), the joint contribution of pyruvate kinase (PK) and malic enzyme (ME) to Pyr ($V_{\text{PK+ME}}$), and substrate flux to Pyr (V_{LDH}). Multiple substrates, including lactate (Lac) and amino acids, shuttle through Pyr to the CAC; thus, V_{LDH} encompasses all non-PEP derived, unlabeled sources of anaplerotic flux to the CAC.

Table 4.1
Metabolic network model for *in vivo* metabolic flux analysis.

<i>Anaplerosis and Gluconeogenesis</i>		
V_{EndoRA}	G6P (AaBbCcDdEeFfg)	→ Gluc.ext (AaBbCcDdEeFfg)
V_{PYGL}	Glycogen (AaBbCcDdEeFfg) + H (h)	→ G6P (AaBhCcDdEeFfg) + H (b)
V_{GPI}	F6P (AabBCcDdEeFfg) + H (h)	→ G6P (AbBhCcDdEeFfg) + H (a)
V_{ALDO}	DHAP (CchBAab) + GAP (DdEeFfg)	→ F6P (AabBCcDdEeFfg) + H (h)
V_{GAPDH}	BPG (ABbCcd) + H (e) + H (f)	→ 0.5*GAP (AfBeCcd) + 0.5*DHAP (AefBCcd) + H (b)
V_{GK}	Glycerol (AaeBbCcd) + H (f)	→ 0.5*DHAP (AfeBCcd) + 0.5*GAP (AeBfCcd) + H (a) + H (b)
V_{ENO}	PEP (ABCcd) + H (b)	→ BPG (ABbCcd)
$V_{\text{PK+ME}}$	PEP (ABCab) + H (c)	→ Pyr (ABCabc)
V_{PC}	Pyr (ABCcde) + CO ₂ (D) + H (f) + H (g)	→ 0.5*Oac (ABCfgD) + 0.5*Oac (DCBfgA) + H (c) + H (d) + H (e)
V_{PCK}	Oac (ABCabD)	→ PEP (ABCab) + CO ₂ (D)
V_{LDH}	Lac (ABbCcde)	→ Pyr (ABCcde) + H (b)
<i>Citric Acid Cycle</i>		
V_{CS}	Oac (ABCcdD) + AcCoA (EFfgh)	→ Cit (DCcdBFfgEA) + H (h)
V_{IDH}	Cit (ABabCDcdEF) + H (e)	→ Akg (ABCeaDcdE) + H (b) + CO ₂ (F)
V_{OGDH}	Akg (ABCabDcdE)	→ SucCoA (BCabDcdE) + CO ₂ (A)
V_{SDH}	SucCoA (ABabCcdD) + H (e) + H (f)	→ 0.5*Oac (ABCefD) + 0.5*Oac (DCBefA) + H (a) + H (b) + H (c) + H (d)
<i>Infusates</i>		
V_{INF}	Gluc.inf (AaBbCcDdEeFfg)	→ Gluc.ext (AaBbCcDdEeFfg)
H_{INF}	H.inf (a)	→ H (a)
H_{SINK}	H	→ Sink
V_{PCC}	PropCoA (ABabCcde) + CO ₂ (D)	→ SuccCoA (ACcdBabD) + H (e)

The 19 reaction network model used for *in vivo* metabolic flux analysis, depicted in Figure 4.1, tracks both carbon (uppercase letters) and hydrogen (lowercase letters) atom transitions through the citric acid cycle and gluconeogenesis (Table A1). Infusion is indicated by *inf*. Transport out of the liver is indicated by *ext*. CO₂ is unbalanced in the model because free transfer into or out of the system is assumed. Some metabolites have hydrogen atoms that are biochemically equivalent. The carbon positions of the equivalent hydrogen atoms are detailed in Table A2.

Table 4.2
Metabolites with equivalent hydrogen atoms.

Metabolite	Carbon Position
AcCoA	2
Lactate	3
PropCoA	3
Pyr	3

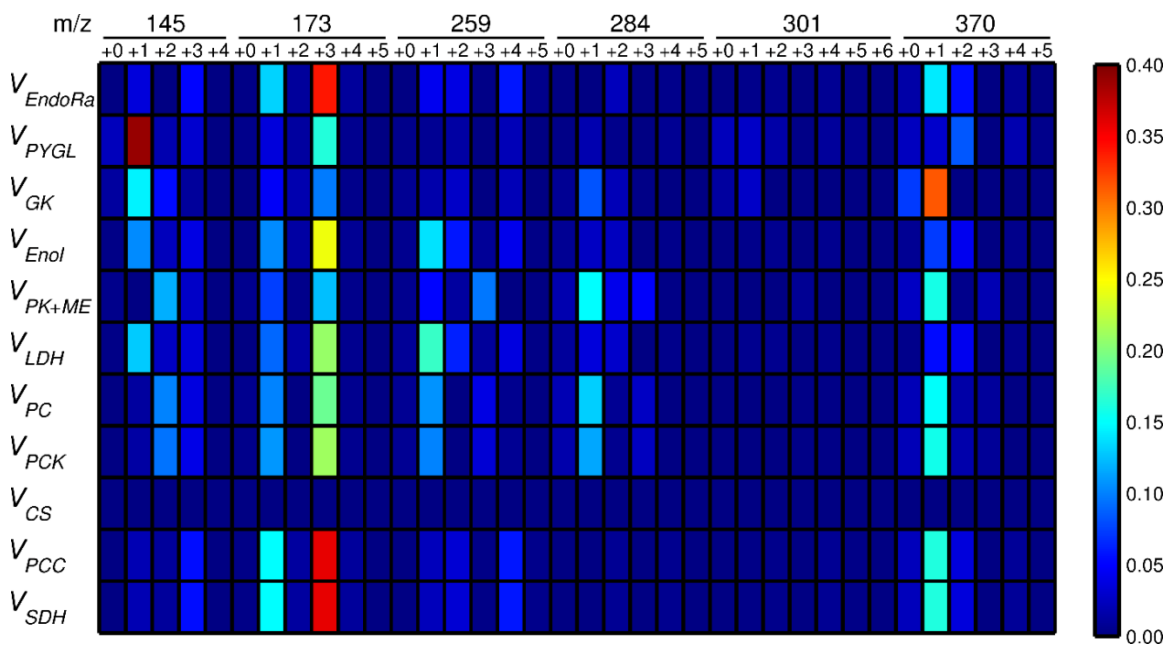


Figure 4.2
The dependence of each flux estimate on isotopomer measurements. The heatmap shows the fractional contribution of mass isotopomers from each glucose fragment ion (top) to flux estimates (left).

Proof-of-concept: [U-¹³C₃]-propionate infusion rate study

Mice were placed in one of three [U-¹³C₃]-propionate infusion groups and fasted 15.5 hours. The experimental time course (Figure 4.3A) began when a 40 μL baseline arterial plasma sample was collected at -125 minutes. ²H₂O and [6,6-²H₂]-glucose venous administration was the same across infusion groups. A bolus of ²H₂O was administered to all mice at -120 minutes to achieve a 4.5% ²H enrichment of body water. An 80 mg·kg⁻¹ prime of [6,6-²H₂]-glucose was also given at -120 minutes. Following the prime, [6,6-²H₂]-glucose was continuously infused at 0.8 mg·kg⁻¹·min⁻¹. At 0 minutes, mice in the *standard* infusion group received a 108.9 mg·kg⁻¹ prime of [U-¹³C₃]-propionate followed by a continuous infusion at 5.4 mg·kg⁻¹·min⁻¹. Mice in the *one-half* infusion group received half of the *standard* [U-¹³C₃]-propionate dose per kilogram (54.5 mg·kg⁻¹ prime and infusion at 2.7 mg·kg⁻¹·min⁻¹). Accordingly, mice in the *one-fourth* infusion group received a quarter of the *standard* [U-¹³C₃]-propionate dose per kilogram (27.2 mg·kg⁻¹ prime and infusion at 1.4 mg·kg⁻¹·min⁻¹). Plasma samples were collected from the arterial line at 90, 100, and 110 minutes after approximately 19 hours of fasting.

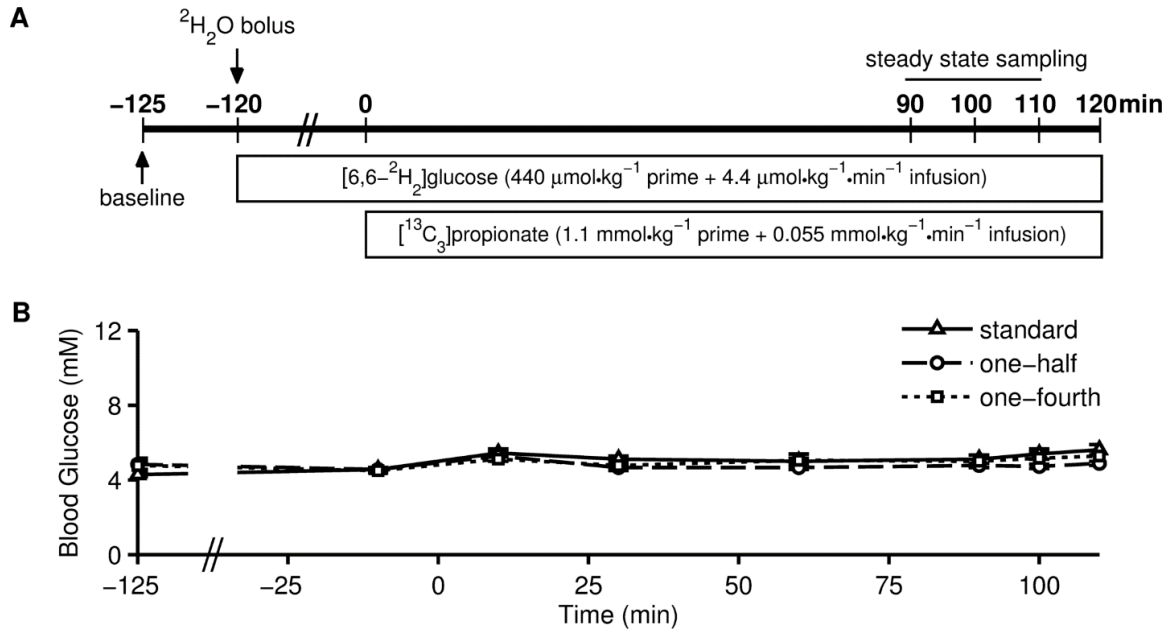


Figure 4.3

The experimental timecourse. (A) Experimental timeline. A 40 μL baseline plasma sample was taken from each mouse at -125 minutes. At -120 minutes, a bolus of $^2\text{H}_2\text{O}$ was administered, and the 0.8 $\text{mg}/\text{kg}/\text{min}$ infusion of [6,6- $^2\text{H}_2$]-glucose was initiated with an 80 mg/kg prime. At 0 minutes, the 5.4 $\text{mg}/\text{kg}/\text{min}$ infusion of [U- $^{13}\text{C}_3$]-propionate was initiated with a 108.9 mg/kg prime for the *standard* infusion group, as shown. Accordingly, the *one-half* infusion group received a 54.5 mg/kg prime followed by a continuous infusion of 2.7 $\text{mg}/\text{kg}/\text{min}$ [U- $^{13}\text{C}_3$]-propionate. The *one-fourth* infusion group received a 27.2 mg/kg prime followed by a continuous infusion of 1.4 $\text{mg}/\text{kg}/\text{min}$ [U- $^{13}\text{C}_3$]-propionate. 50 μL isotopic steady state plasma samples were taken at 90, 100, and 110 minutes. Note the break in the timeline between -120 and 0 minutes. (B) The average blood glucose measurements taken over the time course for the mice in the *standard* (triangle, solid line; $n=7$), *one-half* (circle, dashed line; $n=8$), and *one-fourth* (square, dotted line; $n=8$) infusion groups. Note the break in the x-axis between -125 and -25 minutes.

Blood glucose measurements were taken throughout the experimental time course.

No significant differences in blood glucose were observed among the [U- $^{13}\text{C}_3$]-propionate infusion groups (Figure 4.3B). Ten minutes after the administration of the [U- $^{13}\text{C}_3$]-propionate prime, a 14-20% increase in blood glucose was observed in all infusion groups. Thirty minutes later, blood glucose had returned to pre-prime levels (Figure 4.3B). The similarity in blood glucose throughout the time course suggests that the propionate infusion rate does not significantly alter hepatic glucose production.

Plasma glucose samples collected at -125, 90, 100, and 110 minutes (Figure 4.3A) from each mouse were analyzed by GC-MS. Baseline samples collected at -125 minutes produced MIDs that matched the theoretical distribution expected based on the natural abundance of stable isotopes. For example, the m/z 301 fragment, which retains all of the carbon and hydrogens from the parent glucose molecule (Figure 1.1), had less than 0.5% RMSE relative to its theoretical MID. Compared to baseline, m/z 301 fragment ions from samples collected at 90, 100, and 110 minutes showed a significant decrease in the relative abundance of the unlabeled ($M+0$) mass isotopomer (Figure 4.4A-C). In all infusion groups, the average MID was unchanged from 90 to 110 minutes, confirming that isotopic steady state had been achieved (Figure 4.4A-C).

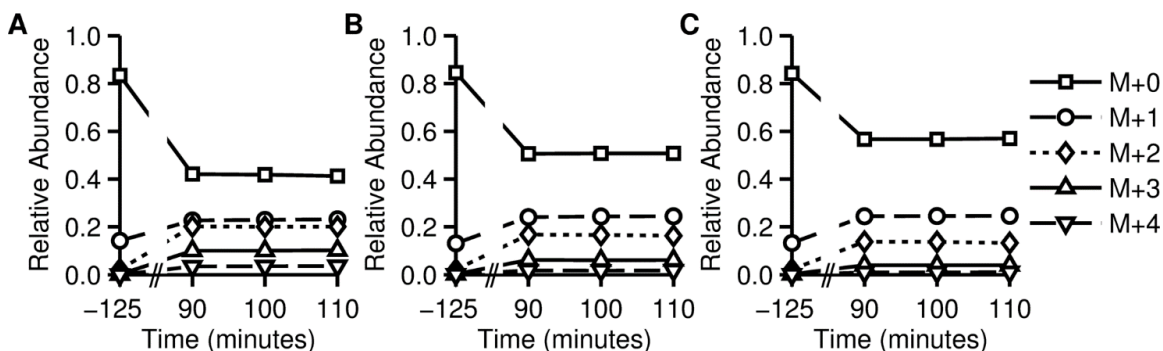


Figure 4.4

Relative isotopomer abundances over the experimental timecourse. Average relative abundance of m/z 301 isotopomers at baseline (-125 minutes) and isotopic steady state (90, 100, and 110 minutes) for mice in the (A) *standard* ($n=7$), (B) *one-half* ($n=8$), and (C) *one-fourth* ($n=8$) infusion groups. The y-axis shows the relative uncorrected abundance of each isotopomer detailed in the legend from $M+0$ (unlabeled, m/z 301) to $M+4$ (m/z 305). Note the break in the x-axis.

The isotopic steady state MIDs showed $[U-^{13}C_3]$ -propionate dose-dependent trends in enrichment (Figure 4.5A-F). In all glucose fragments analyzed (Figure 1.1), the *one-fourth* infusion group showed the highest average abundance of unlabeled ($M+0$)

isotopomers and the *standard* infusion group showed the lowest average abundance of unlabeled (M+0) isotopomers. Because the $^2\text{H}_2\text{O}$ bolus was the same for all infusion groups, the relative abundance of the M+1 isotopomers that result from single ^2H incorporation are not significantly different. However, the abundance of higher mass M+2 to M+4 isotopomers trend with the $[\text{U-}^{13}\text{C}_3]$ -propionate infusion rate. In all fragments, the relative abundance of M+2 to M+4 isotopomers is highest in the *standard* infusion group and lowest in the *one-fourth* infusion group. For example, the m/z 301 fragment shows that glucose from the *standard* infusion group was 40% unlabeled (M+0) and 60% enriched with ^2H and ^{13}C isotopes, while the *one-half* infusion group was 50% enriched and the *one-quarter* infusion group was 40% enriched (Figure 4.5E).

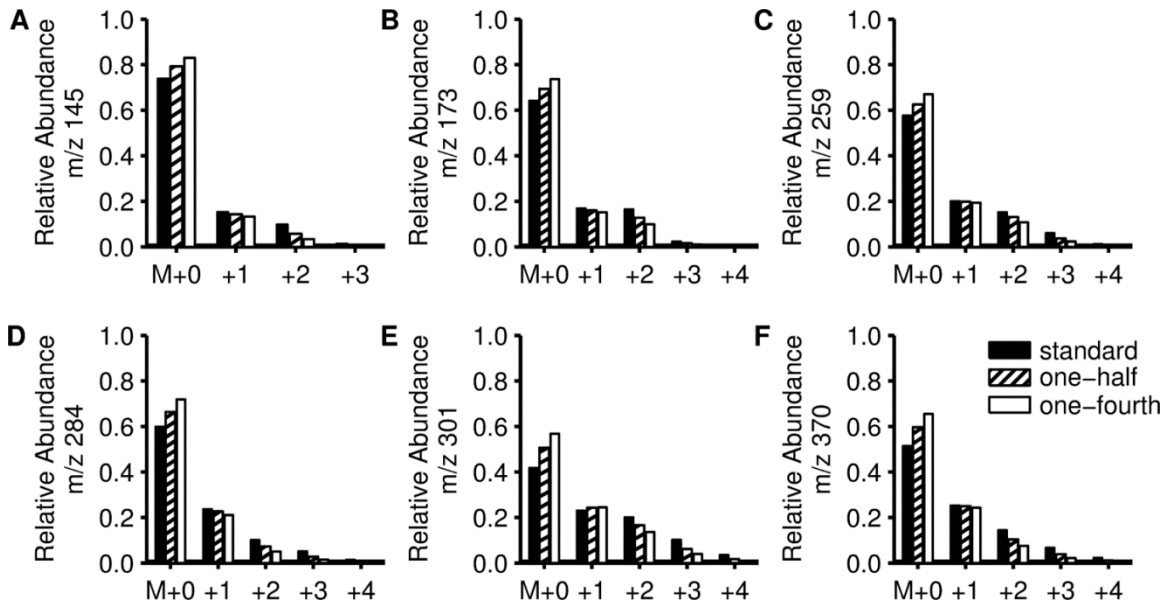


Figure 4.5

Comparison of isotopic enrichment levels to $[\text{U-}^{13}\text{C}_3]$ propionate dose. Comparison of mean isotopic steady state mass isotopomer distributions among *standard* (black bars; n=7 mice), *one-half* (striped bars; n=8 mice), and *one-fourth* (white bars; n=8 mice) infusion groups for six glucose fragments (Fig. 1B): (A) m/z 145; (B) m/z 173; (C) m/z 259; (D) m/z 284; (E) m/z 301; (F) m/z 370. The y-axis shows the relative uncorrected abundance of each isotopomer detailed on the x-axis, where M+n refers to the mass shift from the unlabeled state.

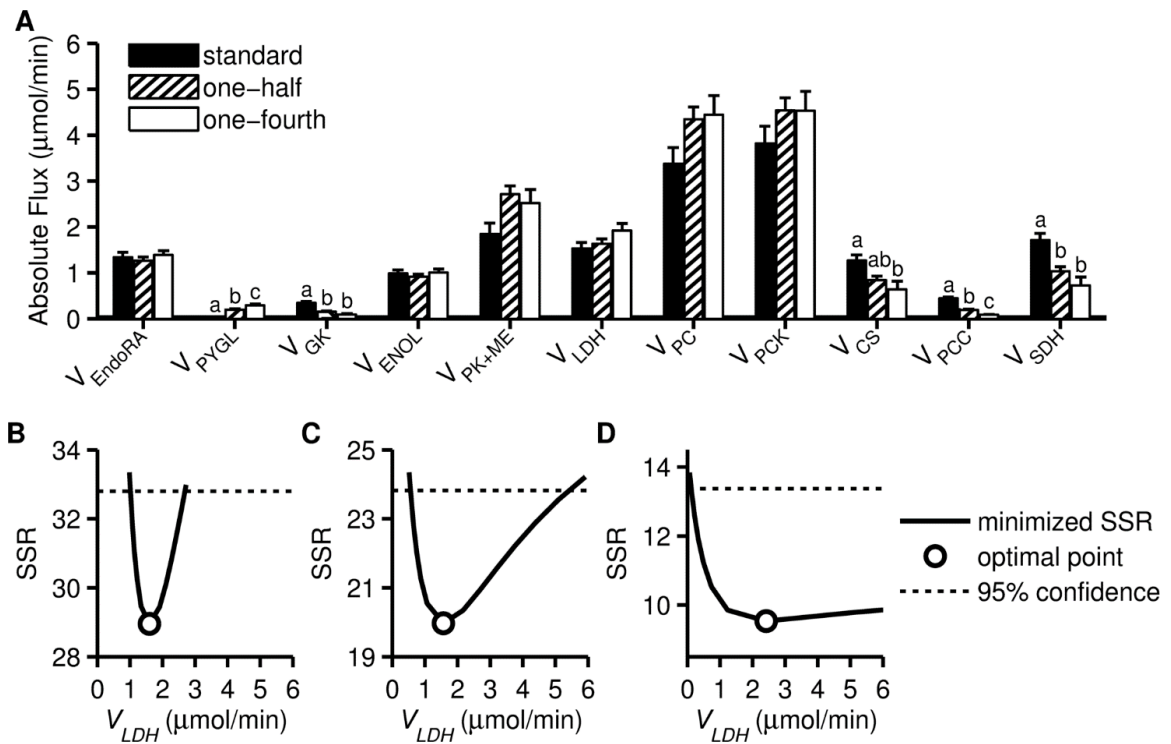


Figure 4.6

Comparison of flux estimates among infusion groups. (A) Comparison of model-estimated fluxes among infusion groups: *standard* (black bars; $n=7$ mice); *one-half* (striped bars; $n=8$ mice); *one-fourth* (white bars; $n=8$ mice). The MFA results for the three isotopic steady state samples were averaged to obtain one representative set of values for each mouse. The bars represent the mean of the biological replicates, and the error bars show the standard error of the mean. V_{GK} and V_{ENOL} are reported in hexose units. One-way ANOVA indicated at least one mean was different at V_{PYGL} , V_{GK} , V_{CS} , V_{PCC} , and V_{SDH} . Tukey-Kramer was then used for pairwise comparisons. Letters above the bars indicate statistically separated groups. (B) Visualization of the 95% confidence interval (CI) around the estimates for V_{LDH} obtained for one representative mouse in the *standard*, (C) *one-half*, and (D) *one-fourth* infusion groups. The solid line depicts the lack of model fit to the data, measured by the sum of squared residuals (SSR), as a function of the V_{LDH} flux value. The model-determined optimal point occurs where the SSR is minimized. The V_{LDH} flux was varied in each direction away from the optimal point while adjusting the remaining fluxes to obtain a new constrained minimum. The 95% confidence interval is determined by the points where the solid line intersects with the 95% confidence threshold (dotted line).

The flux of $[\text{U-}^{13}\text{C}_3]$ -propionate into the citric acid cycle, V_{PCC} , showed a significant, infusion rate-dependent trend (Figure 4.6A) that is consistent with the differences in the relative abundance of higher mass isotopomers in the derivative fragments (Figure 4.5A-F). The flux through V_{PCC} was linearly correlated with the infusion

rate ($R^2=0.9981$). Other fluxes in the citric acid cycle, V_{CS} and V_{SDH} , were also significantly correlated with the $[U-^{13}C_3]$ -propionate infusion rate (Figure 4.6A). These trends suggest $[U-^{13}C_3]$ -propionate infusion enhances flux through the citric acid cycle.

Flux into gluconeogenesis, V_{ENOL} , was the same for all infusion groups (Figure 4.6A). While some infusion rate-dependent trends were observed in the citric acid cycle fluxes, carbon entered gluconeogenesis at the same rate among all infusion groups, regardless of the $[U-^{13}C_3]$ -propionate infusion rate. Consistent with the blood glucose measurements (Figure 4.3B), the rate of endogenous glucose production (V_{EndoRA}) was the same for all infusion groups.

The rates of glycogen depletion, V_{PYGL} , and glycerol utilization, V_{GK} , showed unexpected, $[U-^{13}C_3]$ -propionate infusion rate-dependent trends (Figure 4.6A). All of the mice were fasted 19 hours, and therefore, we expected glycogen stores to be completely depleted. Therefore, we hypothesized that the apparent increase in V_{PYGL} flux at lower infusion rates was a model artefact that emerges due to a reduction in the $[U-^{13}C_3]$ -propionate contribution to glucose enrichment. Simulations in INCA confirmed that the model-estimated values for V_{PYGL} and V_{GK} were inversely correlated. For example, fixing the V_{PYGL} flux to zero in the model resulted in a corresponding increase in the model-estimated V_{GK} flux, and vice versa. Higher mass (M+3 and M+4) isotopomers of glucose were formed from the condensation of a ^{13}C -labeled triose-phosphate intermediate (derived from CAC) with an unlabeled triose-phosphate (potentially derived from glycerol). For many fragments, M+3 and M+4 isotopomers were reduced in the *one-half* infusion group and completely absent in the *one-fourth* infusion group (Figure 4.5). The low abundance of these high mass isotopomers likely contributed to the model's inability to accurately

determine V_{GK} . A similar issue was observed by Antoniewicz et al. (2) in their retrospective analysis of two previous *in vivo* [U- $^{13}\text{C}_6$]-glucose infusion studies, where decreased abundance of high mass isotopomers was implicated as the cause of poor flux identifiability in the study that used a lower tracer infusion rate.

Flux estimates were highly reproducible across different mice within the same infusion group. This precision is reflected in the standard errors shown in Figure 4.6A. However, sensitivity analysis of the best-fit model estimates indicated a gradual loss of flux identifiability with decreasing infusion rate. The 95% flux confidence intervals for the samples in the *standard* infusion group were parabolic and narrow with a well-defined optimal point. One such confidence interval is visualized in Figure 4.6B for a representative sample in the *standard* infusion group. The model-predicted 95% confidence interval for V_{LDH} had a lower limit of 0.99 and an upper limit of 2.72 $\mu\text{mol}/\text{min}$, closely bracketing the optimal value of 1.60 $\mu\text{mol}/\text{min}$. While still parabolic, the confidence intervals for the samples in the *one-half* infusion group were wider than those observed in the *standard* infusion group, with optimal points that were less well defined. In the example shown in Figure 4.6C for one representative sample in the *one-half* infusion group, the optimal V_{LDH} value was 1.57 $\mu\text{mol}/\text{min}$ and the 95% confidence interval ranged from 0.52 to 5.92 $\mu\text{mol}/\text{min}$. Finally, the confidence intervals for the samples in the *one-fourth* infusion group were not parabolic. Instead, the confidence intervals were very long and flat on one or both sides of the optimal point, which was poorly defined. For one representative sample in the *one-fourth* infusion group (Figure 4.6D), the optimal V_{LDH} value was 2.42 $\mu\text{mol}/\text{min}$, the lower limit of the 95% confidence interval was 0.07 $\mu\text{mol}/\text{min}$, and the upper limit of the confidence interval was 1.06×10^5 $\mu\text{mol}/\text{min}$ (off scale). The low glucose enrichment

(Figure 4.5) in the *one-fourth* infusion group, and to a lesser extent in the *one-half* infusion group, likely led to the loss in flux identifiability at lower infusion rates.

The data from these studies supported the use of the *standard* prime and infusion rate. While some enhancement in the CAC flux was observed, the high levels of glucose enrichment and the narrow confidence intervals obtained on model-derived flux estimates together indicated that the *standard* dose was optimal for further studies.

Proof-of-concept: Fasting study

The mice in the *standard* infusion group, hereafter referred to as the *long-term* fasting group, had been fasted for 19 hours at the time isotopic steady state plasma samples were collected. To test the effect of fasting period on hepatic glucose production, mice were fasted 5.5 hours before the experimental time course was initiated, with the collection of a 40 μ L baseline plasma sample at -125 minutes (Figure 4.3). The *standard* protocol, previously determined to be optimal, was used for tracer infusions. Plasma samples were collected from the arterial line at 90, 100, and 110 minutes after approximately 9 hours of fasting. These mice comprised the *short-term* fasting group.

Blood glucose measurements were taken throughout the time course. At -125 minutes, the *short-term* fasted mice had a significantly higher blood glucose level than the *long-term* fasted mice (Figure 4.7A), as expected. After the [U- 13 C $_3$]-propionate prime was given at 0 minutes, a spike in blood glucose was observed in both the *short* and *long-term* fasted mice (Figure 4.7A). The increase in blood glucose was of a similar magnitude in both groups. Blood glucose was significantly different between groups from the beginning

of the time course to 90 minutes. The average blood glucose measurements from 100 to 120 minutes were not significantly different between the groups (Figure 4.7A).

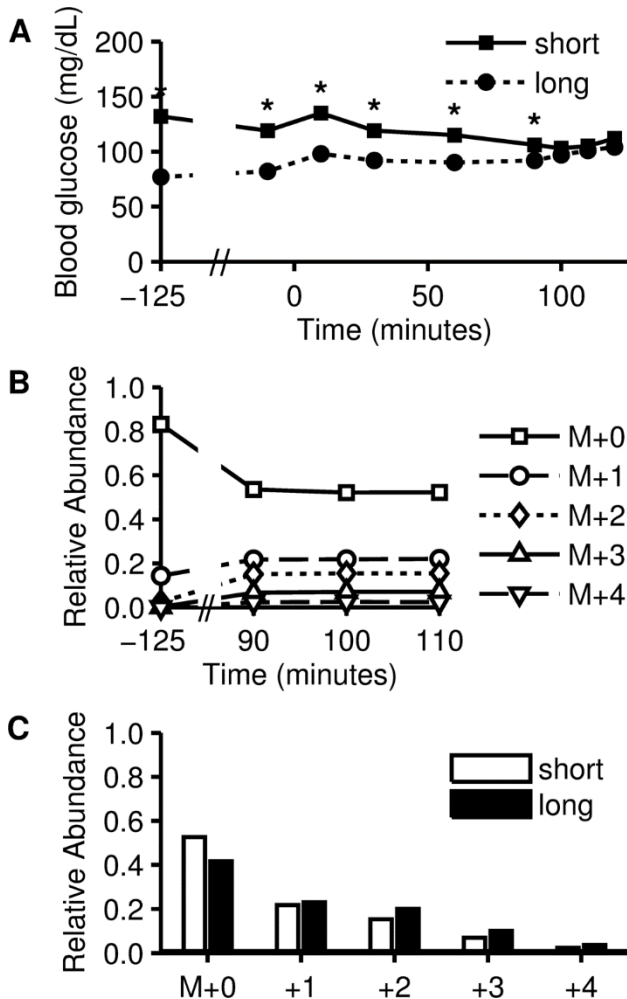


Figure 4.7

Comparison of blood glucose and enrichment levels between fasting groups. (A) Comparison of the average blood glucose measurements taken over the experimental time course for *short* (square marker, solid line; n=5) and *long*-term (circle marker, dotted line; n=7) fasted mice; *p < 0.05. (B) The average mass isotopomer distributions for fragment m/z 301 from baseline (-125 minutes) and isotopic steady state (90, 100, and 110 minutes) samples from *short*-term fasted mice (n=5). (C) Comparison of the average relative abundance of m/z 301 isotopomers between the *short* (n=5) and *long*-term (n=7) fasted mice at isotopic steady state. At 90-110 minutes, the mice in the *short*-term group had been fasted approximately 9 hours, while the mice in the *long*-term group had been fasted 19 hours. For (B) and (C), relative abundance is shown uncorrected for each mass isotopomer from m/z 301 (M+0) to m/z 305 (M+4).

The glucose in the -125, 90, 100, and 110 minute plasma samples from the *short-term* fasted mice was derivatized and analyzed by GC-MS. Like the *long-term* fasted mice (Figure 4.4A), the *short-term* fasted mice were at isotopic steady state during sample collection at 90, 100, and 110 minutes. The average MID for the m/z 301 fragment was unchanged from 90 to 110 minutes (Figure 4.7B). At isotopic steady state, the *short* and *long-term* fasted mice showed differences in stable isotope labeling. For example, the M+0 isotopomer of the m/z 301 fragment was more abundant in the *short-term* than in the *long-term* fasted mice (Figure 4.7C).

The MIDs from the *short-term* fasting group were imported into INCA for MFA. The fluxes in the model (Figure 4.1) were estimated and compared to the average fluxes from the *long-term* fasting group (Figure 4.8). At isotopic steady state, the *short-term* group had been fasted 9 hours, while the *long-term* group had been fasted 19 hours. The absolute fluxes reported either with normalization to mouse weight (i.e., in units of $\mu\text{mol}/\text{min}$, Figure 4.8A) or without normalization (in units of $\mu\text{mol}/\text{kg}/\text{min}$, Figure 4.8B) show expected trends. The rate of glycogen breakdown, V_{PYGL} , was significant in the *short-term*, 9 hour fasted mice. However, after *long-term* fasting, glycogen stores were depleted and flux through V_{PYGL} was negligible. Other carbon sources, including glycerol (V_{GK}) and PEP (V_{ENOL}), were used exclusively by the *long-term* fasted mice for hepatic glucose production (Figure 4.8A-B). This shift becomes even more evident when fluxes are reported relative to V_{EndoRA} (Figure 4.8C), consistent with the differences in enrichment observed in Figure 4.7C.

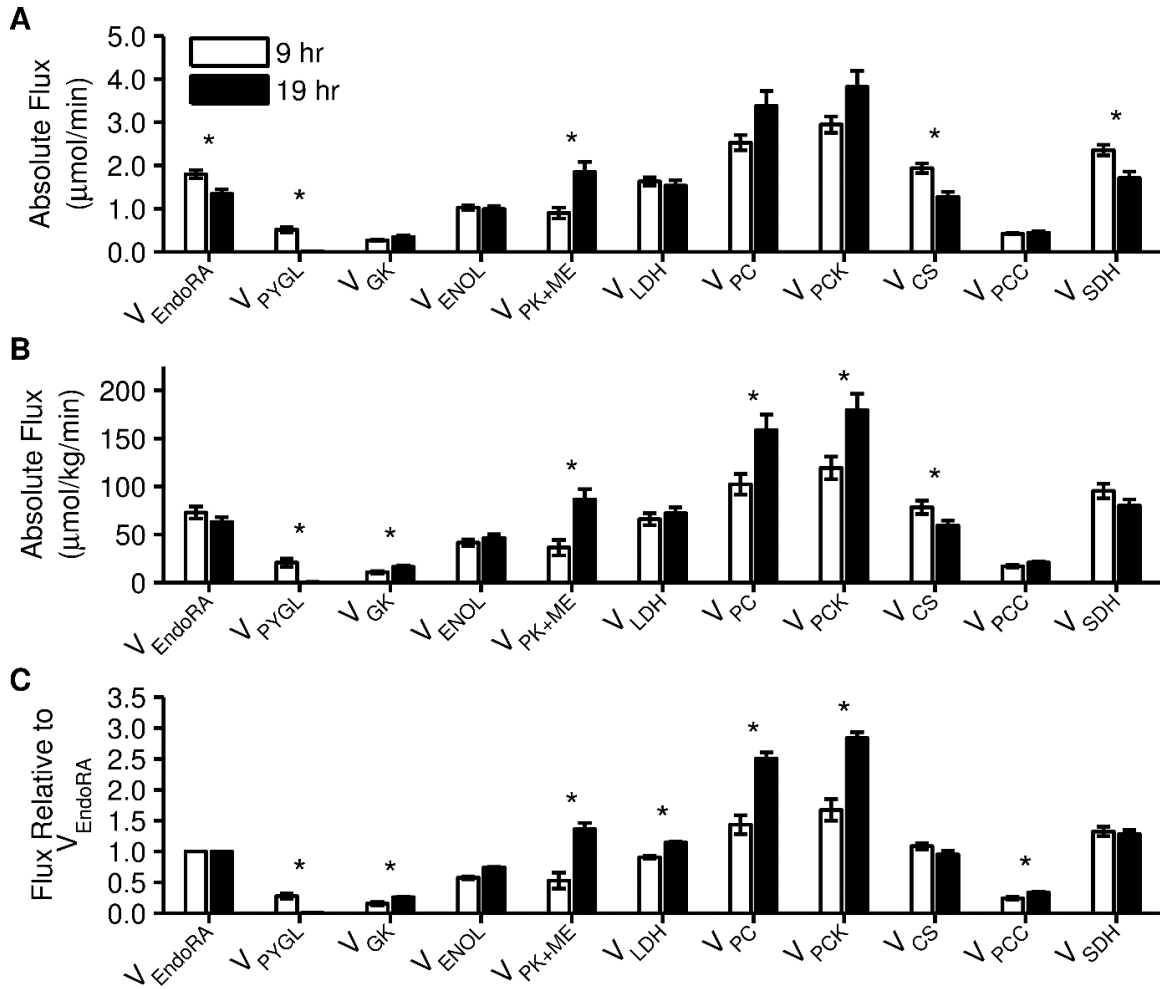


Figure 4.8

Effect of fasting time on fluxes. Comparison of model-estimated fluxes after 9 (white bars; n=5 mice) and 19 (black bars; n=7 mice) hours of fasting (A) in $\mu\text{mol}/\text{min}$, (B) in $\mu\text{mol}/\text{kg}/\text{min}$, (C) relative to V_{EndoRA} . V_{GK} and V_{ENOL} are reported in hexose units. The MFA results for the three isotopic steady state samples were averaged to obtain one representative set of values for each mouse. The bars represent the mean of the representative sets, and the error bars show the standard error of the mean. The statistical comparison was performed by a Student's t-test with equal variance; *p < 0.05.

Effect of CO₂ recycling on flux values

The base model (Table 4.1) was revised to allow ¹³CO₂ recycling in order to test assumption (E) described in **Modeling hepatic glucose production in INCA**. Two additional reactions were added: (1) a CO₂ source reaction (CO₂.source (A) → CO₂ (A));

(2) a CO₂ sink reaction (CO₂ (A) → CO₂.sink (A)). In this revised model, CO₂ is a balanced metabolite, and ¹³CO₂ produced in the CAC or during pyruvate cycling can be fixed by PCC or PC. Fluxes were estimated and fits were accepted as described above. Within each group, the average fit to the model improved, as indicated by a decrease in SSR compared to the base model (Table 4.3). The improvement in fit was most significant (≥50% decrease in SSR) for *long-term* fasted mice. While the simulated enrichment of the CO₂ pool was not significantly different between the *short-term* and *long-term* fasted mice infused with the *standard* [¹³C₃]propionate dose (Table 4.3), CO₂ fixation was greater in the *long-term* fasted mice, allowing for a more significant change in MIDs and fit (Figure 4.8-4.9). Because CO₂ is produced during the conversion of [¹³C₃]propionate to succinyl-coA, the enrichment of the CO₂ pool trended with infusion rate (Table 4.3).

CAC and pyruvate cycling fluxes changed when CO₂ recycling was allowed. Differences in CAC-related fluxes among the three [¹³C₃]propionate infusion groups became insignificant (Figure 4.9A), suggesting that the infusion rate may not significantly alter intermediary metabolism. As expected, the V_{PCC} estimates showed an infusion rate-dependent change (Figure 4.9A). Discrepancies in V_{GK} and V_{PYGL} were still apparent and related to low enrichment and poor flux identifiability in the *one-half* and *one-fourth* infusion groups (Figure 4.9A). Qualitatively, the trends observed between the *short-* and *long-term* fasted mice did not change when the data was fit to the revised model (Figure 4.9B).

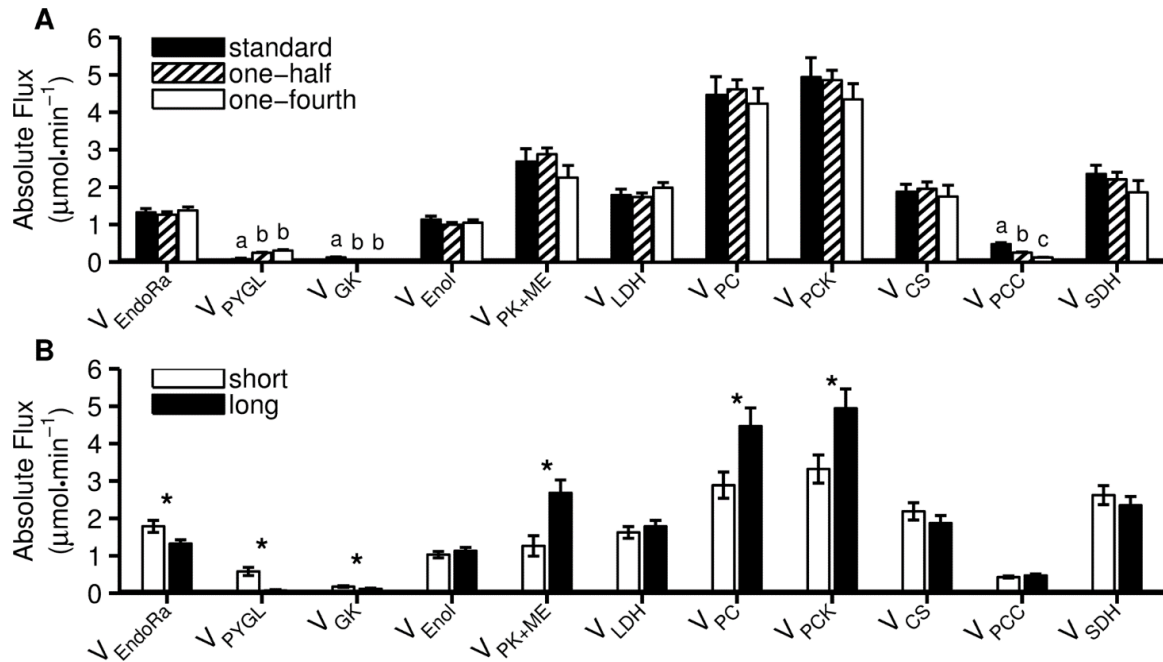


Figure 4.9

The effect of CO₂ recycling on flux estimates. Comparison of model-estimated fluxes with CO₂ recycling (A) from *long-term* fasted mice in the *standard* (black bars; $n=7$), *one-half* (striped bars; $n=8$), and *one-fourth* (white bars; $n=8$) [¹³C₃]propionate infusion groups and (B) from *short-* (white bars; $n=5$) and *long-term* (black bars; $n=7$) fasted mice. MFA results within each group were averaged to obtain a representative set of values for each mouse. Data are presented as means \pm SEM. V_{GK} and V_{Enol} are reported in hexose units. Infusion groups were compared by one-way ANOVA and Tukey-Kramer; letters above the bars indicate statistically separated groups. Fasting groups were compared using a *t*-test with equal variance; $*p<0.05$.

Table 4.3
Effect of CO₂ recycling on SSR and simulated CO₂ enrichment.

Fasting Period	[¹³C₃]propionate Infusion Rate	SSR without CO₂ Recycling	SSR with CO₂ Recycling	Simulated CO₂ Enrichment
short	standard	6.1 ± 0.8	4.5 ± 0.3	4.8 ± 0.7%
long	standard	26.2 ± 1.5	5.2 ± 0.8	5.2 ± 0.4%
long	one-half	18.9 ± 4.7	9.6 ± 4.3	4.2 ± 0.4%
long	one-fourth	6.3 ± 0.5	3.4 ± 0.3	2.3 ± 0.2%

Simulated MIDs through the best-fit model were compared to the experimental MIDs, and SSR was calculated. The SSRs for the three isotopic steady state samples were averaged to obtain a representative value for each mouse. The table shows the mean of the representative SSRs ± SEM for each group fit to the base model (**SSR without CO₂ Recycling**) or to the revised model that allowed CO₂ recycling (**SSR with CO₂ recycling**). The enrichment of the hepatic CO₂ pool (i.e. the relative abundance of ¹³CO₂) was simulated through the best-fit model for each mouse. Values are expressed as mean enrichment ± SEM. short/standard *n*=5; long/standard *n*=7, long/one-half *n*=8, long/one-fourth *n*=8.

Validation: ²H₂O and [6,6-²H₂]glucose

One major advantage of the NMR-based MFA methodology is the ability to discriminate between ²H and ¹³C isotopes. The GC-MS-based method can measure the single mass shift associated with isotope incorporation, but the identity of the isotope cannot be determined with standard instrumentation. Our method relies on the model to deconvolute ²H and ¹³C contributions.

To test the model's ability to determine ²H and ¹³C labeling, we combined simulation and experimental studies. We first performed a simulation study using the best-fit model for each mouse in the *short*-term fasting group (*n*=5). [U-¹³C₃]propionate was removed as a tracer from INCA, and the labeling through the best-fit model using only ²H₂O and [6,6-²H₂]glucose was simulated. The simulated MIDs were fit to the base model

(Figure 4.1). We expected that CAC fluxes would not be determinable because they were informed by ^{13}C incorporation from $[\text{U-}^{13}\text{C}_3]\text{propionate}$. However, no fluxes in the model could be estimated with confidence. We hypothesized that the flux values could not be estimated accurately with V_{CS} fixed. When fluxes were estimated relative to V_{EndoRa} , CAC fluxes were not determinable but gluconeogenic fluxes could be estimated with good confidence from simulated data. The model was simplified to remove fluxes that could not be estimated accurately (Figure 4.10). V_{ENOL} , V_{GK} , V_{PYGL} , V_{EndoRa} , and V_{INF} were unchanged from the base model (Figure 4.1). In the base model, pyruvate enters gluconeogenesis by first being converted to Oac by PC and then to PEP by PCK. The carbon transfers involved in these reactions make their estimations impossible with only deuterated tracers. Therefore, a single pyruvate source, labeled V_{PC} in Figure 4.10, was created by combining V_{PC} and V_{PCK} ($\text{Pyr (ABCcde) + H (f) + H (g) \rightarrow PEP (ABCfg) + H (c) + H (d) + H (e)}$).

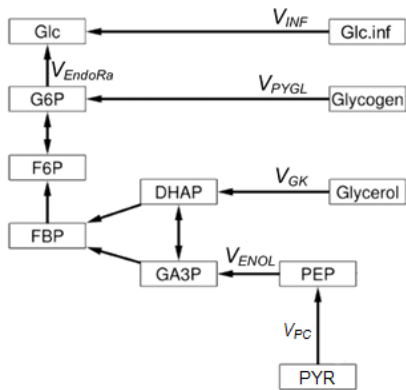


Figure 4.10

A simplified model for estimating gluconeogenic-related fluxes using deuterated tracers. The model has a single pyruvate source, V_{PC} . The remaining reactions are identical to those shown in Figure 4.1.

The GNG-related fluxes V_{EndoRa} , V_{PYGL} , V_{GK} , and V_{Enol} were identical between the simulation study and the fasting study results (Figure 4.11). The combined pyruvate source

flux from the simulation study, V_{PC} , was equal to the amount of pyruvate entering GNG by V_{PCK} minus the amount of PEP converted to Pyruvate by V_{PK+ME} from the fasting study. In all, the simulation study confirmed that GNG-related fluxes in a simplified model could be regressed accurately from experiments that only used ^2H -labeled tracers.

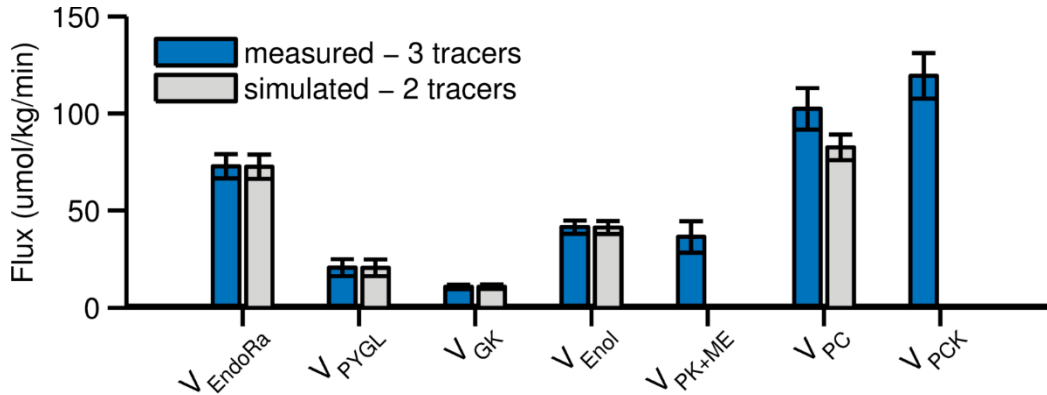


Figure 4.11

Comparison of GNG-related fluxes between simulated and fasting study data. The x-axis shows GNG-related fluxes. The y-axis is absolute flux in $\mu\text{mol}/\text{kg}/\text{min}$. The measured data (blue bars) from the *short-term* fasting study is identical to that shown in Figure 4.8. The flux values in the *measured – 3 tracer* group were obtained by fitting MIDs to the base model (Figure 4.1). The simulated values (gray bars) were obtained by fitting simulated data, containing only ^2H labeling, to a revised model (Figure 4.10).

For the experimental component of this study, eight mice were fasted as in the *short-term* group described in **Proof-of-concept: Fasting study**. The experimental timecourse was identical to Figure 4.3A except $[\text{U-}^{13}\text{C}_3]\text{propionate}$ was not infused. Plasma samples collected at 90, 100, and 110 minutes confirmed that steady-state was reached (Figure 4.12). As expected, the enrichment levels were much lower in this study than in the fasting study, where all three tracers were used (Figure 4.7B).

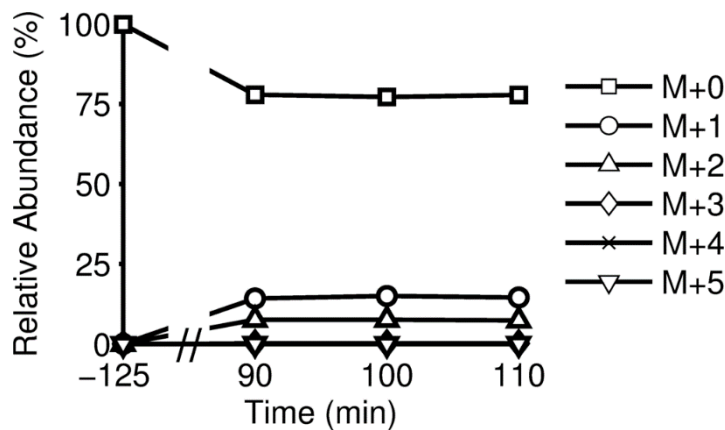


Figure 4.12

^2H enrichment over the experimental timecourse. The mean \pm SEM of the relative abundances of each m/z 301 mass isotopomer from M+0 to M+5 is shown at -125, 90, 100, and 100 minutes. The MIDs were corrected for natural abundance.

The MIDs from this study show the expected M+1 and M+2 labeling patterns (Figure 4.13). Because $^2\text{H}_2\text{O}$ infusion enriches the body water pool by less than 5%, incorporation of more than one ^2H onto a single glucose molecule is unlikely. The only M+2 isotopomers measured were from fragments that contain carbon six of glucose (Figure 1.1). Therefore, the M+2 abundance reflects the infusion of [6,6- $^2\text{H}_2$]glucose.

The MIDs simulated through the best-fit model from the *short-term* fasting group were very similar to the measured MIDs (gray bars vs. orange bars, Figure 4.13). The percent difference in the relative abundance of M+0 ranged from 0.4 to 3.8% (Table 4.4). This result strongly suggests that the model accurately deconvoluted the ^2H and ^{13}C contributions. Based on the similarity in MIDs, we expected flux estimations to be similar. This hypothesis was supported by the results shown in Figure 4.14. All fluxes were estimated with high confidence.

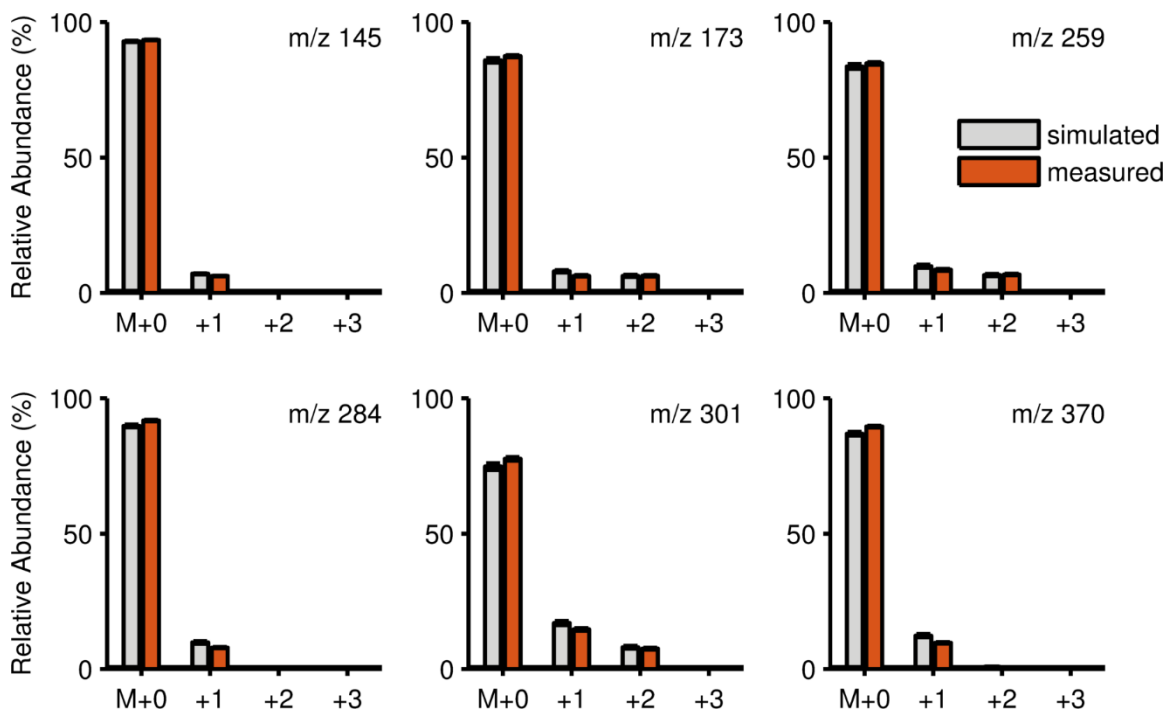


Figure 4.13

Comparison of simulated and measured MIDs. Corrected mean steady-state MIDs \pm SEM for the simulated ($n=5$; gray bars) and measured ($n=8$; orange bars) groups.

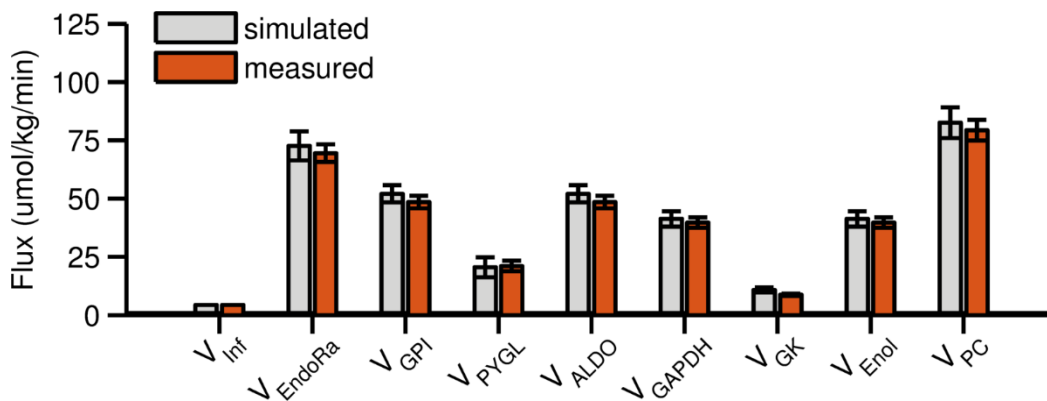


Figure 4.14

GNG-related flux estimates from simulated and measured data. Corrected mean absolute flux values \pm SEM ($\mu\text{mol/kg/min}$). The gray bars show flux estimates from simulated MIDs. The orange bars show flux estimates from measured MIDs.

The reduced model (Figure 4.10) is overly constrained by the mass balance around hydrogen. To test this constraint, the flux of hydrogen into the system was increased *in silico* by reducing the enrichment of the deuterated water tracer by one-half or by one-tenth in INCA. Increasing the hydrogen flux significantly altered estimations of V_{GK} for biological samples using only ^2H tracers. When the hydrogen flux was adjusted to be twice the initial value, V_{GK} was halved and other fluxes in the model compensated but were not significantly different (Figure 4.15). When the hydrogen flux was adjusted to be ten times the initial value, V_{GK} was zero and additional compensation was observed (Figure 4.15). The same effect was not observed with simulated data without added error, suggesting the reduced model is very sensitive to measurement error. Adjusting the hydrogen flux had no effect on V_{GK} in the full model using the *standard* infusion protocol. However, the dependence of V_{GK} estimation on ^{13}C labeling data, observed in the propionate study (see: **Proof-of-concept: [U-13C3]-propionate infusion rate study**), is supported by this finding. The reduced model is therefore best-suited for simulation and validation studies, not for flux estimation from biological samples.

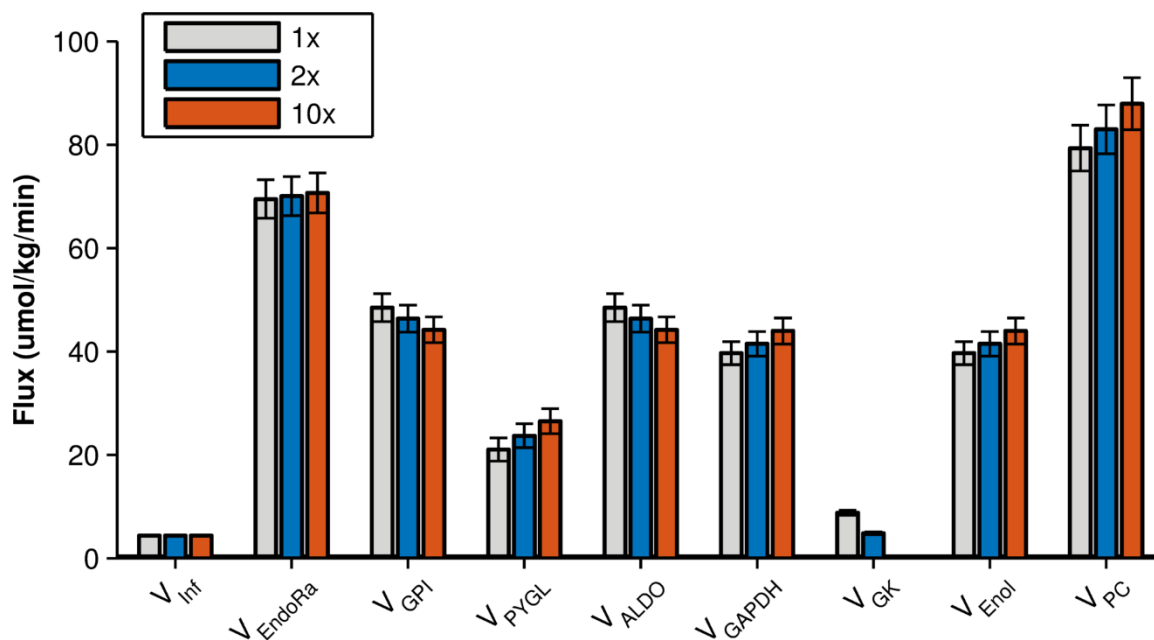


Figure 4.15

Effect of hydrogen flux on the reduced model. Average \pm SEM flux values from biological samples with the standard hydrogen flux into the system (gray bars), twice the normal hydrogen flux (blue bars), or 10 times the normal hydrogen flux (orange bars).

^{13}C recycling could affect the M+1 pool of the simulated MIDs. Incorporation of ^{13}C from CO_2 at V_{PC} or V_{PCC} (Figure 4.1) would cause a single mass shift that the base model would attribute to ^2H incorporation. When MIDs were simulated from the best-fit model that included CO_2 recycling (see: **Effect of CO_2 recycling on flux values**), the simulated MIDs were in better agreement to measured MIDs, with percent differences in M+0 ranging from 0.1 to 1.7% (Table 4.4).

Table 4.4
Percent difference between simulated and measured MIDs with or without $^{13}\text{CO}_2$ recycling.

Fragment (m/z)	M+0 percent difference (%)	
	Without CO_2 recycling	With CO_2 recycling
145	3.8	1.7
173	0.7	0.1
259	1.8	1.0
284	1.4	0.4
301	2.2	1.2
370	3.0	1.6

Conclusions and Future Directions

We hypothesized that six overlapping glucose derivative fragments (Figure 1.1) could provide sufficient information for flux analysis. The results of the studies above strongly support this hypothesis. Combined with mathematical modeling in INCA (Figure 4.1), the measurements provided high-confidence flux estimations.

In the first study, different rates of $[\text{U-}^{13}\text{C}_3]\text{propionate}$ were infused to determine the optimal infusion protocol. The *standard* rate used in NMR experiments was determined to be the best for the GC-MS-based methodology. Reducing ^{13}C enrichment decreased the confidence of flux estimations (Figure 4.6). CAC-related fluxes trended with infusion rate, suggesting that $[\text{U-}^{13}\text{C}_3]\text{propionate}$ infusion may affect intermediary metabolism. However, the rate of endogenous glucose production (V_{EndoRa}) was not significantly different among the groups (Figure 4.6). The stable V_{EndoRa} is also supported by the blood glucose measurements, which did not show an infusion rate-dependent change (Figure 4.3B).

The fasting study produced results (Figure 4.8) that were consistent with physiological expectations. *Long*-term fasting depleted glycogen stores, sending V_{PYGL} to zero. Compared to the *short*-term fasting group, the *long*-term fasted mice relied more heavily on pyruvate, lactate, glucogenic amino acids, and glycerol as carbon sources for glucose. The absolute flux values and their precision were similar to NMR-based studies (61).

The base model (Figure 4.1) could be improved by allowing ^{13}C recycling from the CO_2 pool. When the model was adjusted to allow for CO_2 recycling, fits, as measured by SSR, improved for all groups (Table 4.4). Differences in CAC fluxes reported in the infusion study became insignificant in the revised model, suggesting $[\text{U-}^{13}\text{C}_3]\text{propionate}$ infusion may not significantly affect intermediary metabolism. Future studies measuring metabolic intermediate and amino acid labeling from tissue samples could further validate the methodology and support the inclusion of CO_2 recycling in the model. Empirically measuring the enrichment of the CO_2 pool, perhaps by measuring urea, could also support the addition of recycling to the model.

Simulated and experimental MIDs were closely matched in the $^2\text{H}_2\text{O}$ and $[6,6\text{-}^2\text{H}_2]\text{glucose}$ validation study (Figure 4.13). These results suggest that the model accurately assessed the contribution of ^2H and ^{13}C in the three tracer methodology, at least in *short*-term fasted animals. Simulated data from a model that allowed for CO_2 recycling was a better predictor of the measured data (Table 4.4), further supporting the inclusion of CO_2 recycling in the base model.

The GC-MS-based MFA methodology described in this chapter scales down the traditional NMR-based method. This scaled down method has higher throughput, lower

cost, and improved sensitivity. The extensive computation required can be simplified using a GUI designed for batch processing in INCA (APPENDIX D). For validation studies, we used the same tracers used in NMR. However, simulation studies show that confident flux estimates can be obtained with other tracer sets as well. The methodology described here can serve as a robust platform for the investigation of many biological questions.

CHAPTER V

SUMMARY OF CONCLUSIONS

We hypothesized that the six derivative fragment methodology proposed by Antoniewicz et al. (4) could be used for positional enrichment of glucose from biological samples. The studies described in CHAPTER II supported this hypothesis. While the measurement errors associated with the MID measurements were more significant in biological samples, weighting the fragments by inverse error and reducing the number of isotopomers active in the model allowed for accurate positional enrichment estimations. GUI tools built in the MATLAB programming environment simplified and automated the complex computational steps, increasing the accessibility of the methodology.

We believed that the revised methodology validated in CHAPTER II had broad applicability within metabolic research. We successfully applied the methodology to investigate glucose cycling in isolated mouse islets in CHAPTER III. We showed the first evidence supporting significant rates of glucose cycling, regulated by G6pc2, in mouse islets. Future work will apply the methodology to investigate glucose cycling in human islets.

We hypothesized that the six glucose derivative fragments could provide sufficient information for MFA. Multiple studies described in CHAPTER IV supported this hypothesis. The validated methodology will be used in future studies to quantify metabolic fluxes in mouse models of human disease.

The novel methodology described in this thesis used an interdisciplinary approach to accurately characterize the positional enrichment of stable isotopes on glucose. The combination of chemical and computational methods to assess positional enrichment

represented a major departure from standard NMR-based approaches. The method has the potential to act as a framework for the development of novel strategies for positional enrichment analysis of other metabolites of interest.

APPENDIX A

USER MANUAL FOR THE INTEGRATION GUI

A INTRODUCTION

integrate_gcms is a MATLAB-based graphical user interface (GUI) designed to guide a user through the process of integrating gas chromatography (GC)-mass spectrometry (MS) data from stable isotope tracer experiments in order to obtain mass isotopomer distributions (MIDs) for user-defined metabolites of interest. Integration utilizes a fixed-width, adjustable baseline algorithm described by Antoniewicz et al. (1) and detailed in section F.

B SYSTEM REQUIREMENTS

- Windows 7 or later
- MATLAB R2011a or later, including:
 - Bioinformatics toolbox
 - Statistics toolbox

C GETTING STARTED

C1 Installation

The GUI is provided in a *.zip folder. Extract the folder to any directory. The folder should contain a function **integrate_gcms.m** and three folders: **int_bin**, **int_help**, and **int_methods**.

C2 Launching the GUI

Start MATLAB and change the working directory to the folder containing **integrate_gcms.m**. Type **integrate_gcms** into the Command Window and press enter to launch the GUI. The GUI (Figure A.1) can be resized as needed to fit your screen by using the maximize function or by grabbing the edge of the interface and dragging to adjust the width and/or height.

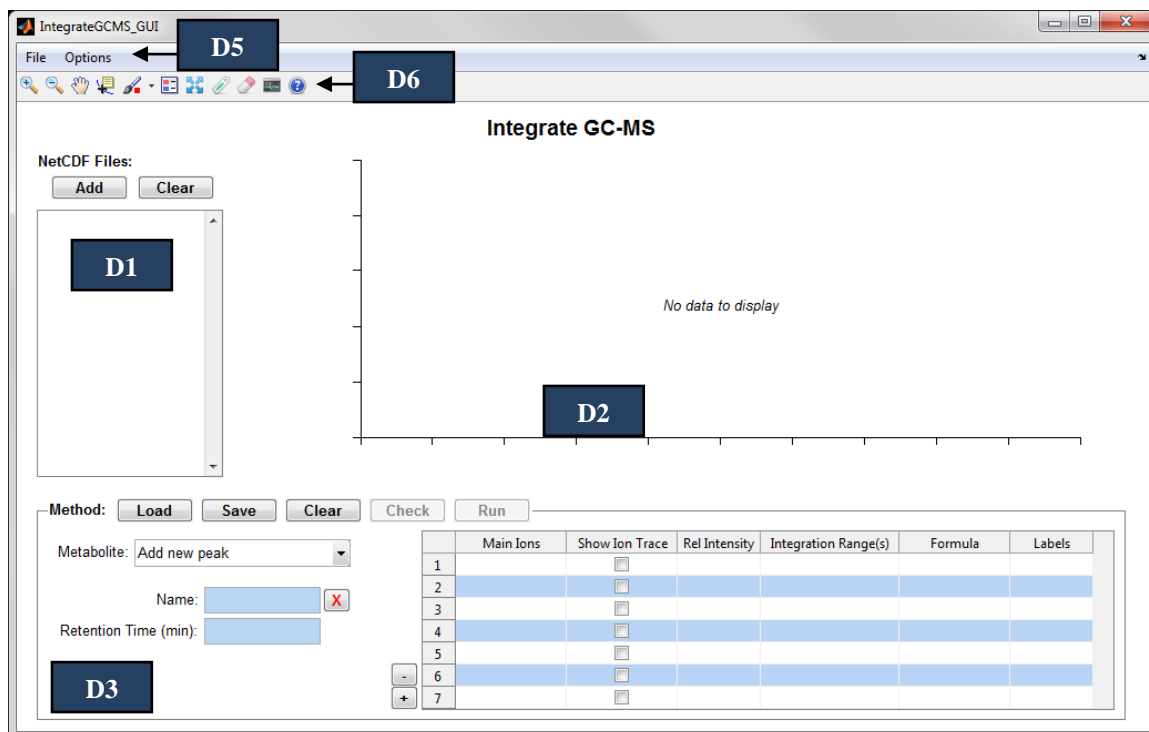


Figure A.1
The launched GUI with major components identified.

D GUI components

D1 File list

The user selects NetCDF data files to load using the file menu (D5.1) or by clicking the **Add** button (Figure A.2). The filenames are displayed in the listbox identified as D1 (Figure A.1). The first filename is highlighted after loading, and its chromatogram is displayed in the GUI axis (D2). Left-click any filename in the listbox to select a different file to visualize. The keyboard's up and down arrows can also be used to quickly browse through the loaded data. The **Clear** button (Figure A.2) removes **ALL** of the loaded files from the GUI workspace.

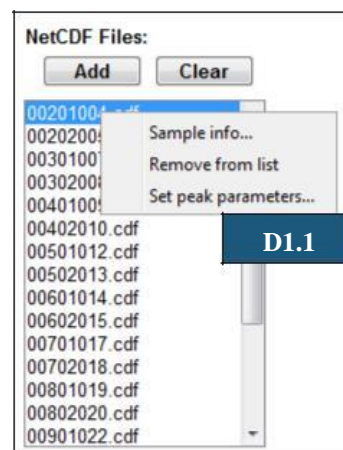


Figure A.2
Loading and visualizing NetCDF files.

D1.1 Right-click menus

Right-clicking on any filename reveals a secondary menu (Figure A.2) with additional options. **Sample info...** displays the meta data associated with that file, including the timestamp of the GC-MS collection, the sample name, and the listed GC-MS operator. **Remove from list** removes the selected file from the loaded data. **Set peak parameters...** reveals a new GUI panel that allows the user to manually edit the retention time, peak start, peak end, and baseline assigned by the algorithm (D4).

D2 Chromatogram plot

The GUI axis, identified as D2 in Figure A.1, displays the chromatogram for the selected file. The x-axis is time in minutes, and the y-axis is total ion abundance. Utilize the plot tools (D6) to investigate the chromatogram. Turn on selected ion traces in the method table (D3.3) to visualize the abundance of an ion range of interest and to identify metabolite peaks (Figure A.3).

D3 Integration method panel

The screenshot shows a software interface for managing integration methods. At the top, there are buttons for 'Method: Load', 'Save', 'Clear', 'Check', and 'Run'. Below these are input fields for 'Metabolite: Aldo', 'Name: Aldo', and 'Retention Time (min): 9.6'. A table with 7 rows and 7 columns is displayed. The columns are labeled 'Main Ions', 'Show Ion Trace', 'Rel Intensity', 'Integration Range(s)', 'Formula', and 'Labels'. The first four rows contain data for peaks 1 through 4. The fifth row is empty. The sixth and seventh rows are highlighted in blue and contain a dark blue box labeled 'D3.3'. A dark blue box labeled 'D3.2' is located at the bottom left of the panel.

	Main Ions	Show Ion Trace	Rel Intensity	Integration Range(s)	Formula	Labels
1	173-178	<input type="checkbox"/>	100	173-178	C8H13O4	H3
2	259-265	<input type="checkbox"/>	24	259-265	C12H19O6	H4
3	284-289	<input type="checkbox"/>	12	284-289	C13H18O6N	H3
4	370-376	<input type="checkbox"/>	14	370-376	C17H24O8N	H4
5		<input type="checkbox"/>				
6		<input type="checkbox"/>				
7		<input type="checkbox"/>				

Figure A.3


The method panel allows the user to load and edit an existing method or create a new method.

D3.1 Button functions

- **Load** Allows the user to select a *.m integration method file (also D5.1).

- **Save** Allows the user to save an integration method as a *.m file (also D5.1).
- **Clear** Clears the loaded method from the GUI workspace.
- **Check** Using the metabolite information defined by the user, the **Check** button finds the target metabolites, calculates the noise and the baseline, and then determines the peak start and the peak end (algorithm detail, F1). The peak start, peak end, and average baseline are displayed for the user as plot annotations following successful completion of **Check** (Figure A.3). Metabolites that are not found are returned with a retention time of zero.
- **Run** The **Run** button sums the total ion counts between the peak start and peak end and subtracts the baseline for each metabolite (algorithm detail, F2). The integrated counts for each ion in the range are normalized, and the mass isotopomer distributions are written to a *.csv file (G4).

D3.2 Metabolite pull-down menu, Name, and Retention Time

The pull-down menu displays all of the defined metabolites. Selecting a metabolite displays its information in the method panel. The name of the metabolite can be changed in the **Name** edit textbox. The  button can be used to remove the selected metabolite from the integration method. The user can refine each metabolite's retention time using the **Retention Time (min)** edit textbox; this information is key to ensure that the GUI can find the target metabolite in each loaded file.

D3.3 Method table

The method table has 6 columns:


- **Main Ions** The main ions expected in the selected metabolite. Each main ion is defined as a range to account for stable isotope labeling (e.g. m/z 173-180). This information is used to find the target metabolite; as such, defining more than one main ion improves the ability of the algorithm to find the metabolite. Each main ion range must have a defined relative intensity (**Rel Intensity**).
- **Show Ion Trace** Check the box beside a defined **Main Ions** cell to visualize the abundance of the ions in the selected range (axis, Figure A.4).
- **Rel Intensity** The estimated relative intensity of each main ion. Every defined main ion range must have a defined relative intensity. This information is used to find the target metabolite.
- **Integration Range(s)** After the metabolites are found with peak start, peak end, and baseline defined, the ion ranges provided in this column define which MIDs are desired by the user. This column is entirely separate from the **Main Ions** column, and the ranges defined can be different from the ranges used for target identification.
- **Formula** The chemical formula of the fragment defined in each integration range. This information is optional, but is necessary to output the theoretical MID for an unlabeled fragment and to correct for natural abundance (D5.2).
- **Labels** The maximum possible labeling if all of the fragment atoms are labeled. For example, if a ^{13}C stable isotope tracer is used, and the fragment

has four carbons, then the **Labels** column should read *C4*. This information is optional, but is necessary to correct for natural abundance (D5.2).

D4 Edit peak parameters panel

This panel is accessible from the Options menu (**Manually set peak parameters...** D5.2) or by right-clicking on any filename in the listbox and selecting **Set peak parameters...** (D1.1 and Figure A.2). The panel covers the **Method table** until the user presses the **Done** button (red box, Figure A.4). Following **Check** (D3.1), the peak start, peak end, and baseline is defined for each file and all metabolites. The user can view and manually edit the algorithm-determined values if they appear to have been set in error. All edits are immediately applied and visualized on the chromatogram.

D4.1 Visualize and Adjust Baselines

The adjustable baseline algorithm calculates a baseline for every ion in each integration range. If the option to **Calculate baseline for each ion** (Figure A.7; D5.2) is checked (default), then the  button beside **Avg Baseline** in the peak parameters panel (Figure A.4) is enabled. Clicking this button launches a small interface that allows the user to view and adjust any of these baselines (Figure A.5). If the **Calculate baseline for each ion** (Figure A.7; D5.2) is not checked, then the integration function will use the average baseline shown in the panel to perform baseline subtraction.

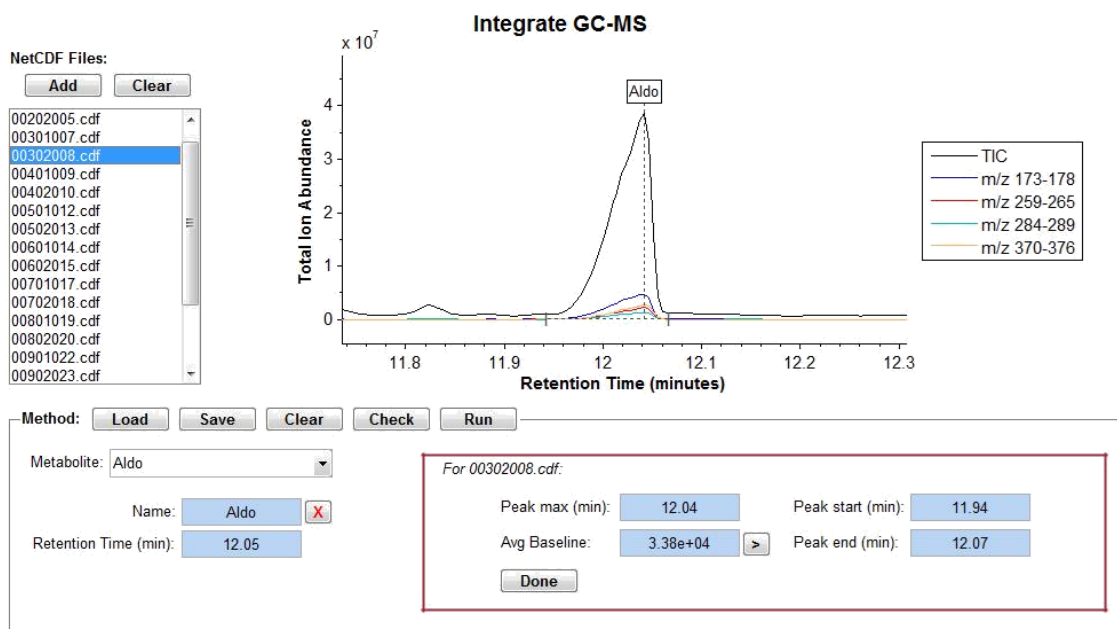


Figure A.4

The peak parameters (highlighted by a red box) can be viewed and edited manually by the user in the panel accessible from the Options menu or by right-clicking on a filename in the listbox.

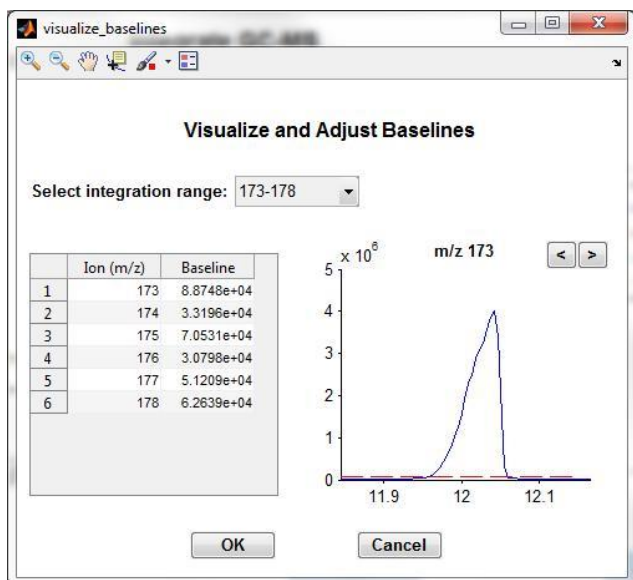


Figure A.5
All calculated baselines can be visualized and edited in the *Visualize and Adjust Baselines* interface.

D5 Menu functions

D5.1 File Menu (Figure A.6)

- **Load data...** Allows the user to select one or more NetCDF files containing GC-MS data for integration (also D1).
- **Load method...** Allows the user to select a *.m integration method file (also D3.1).
- **Save method...** Allows the user to save an integration method as a *.m file (also D3.1).
- **Export data to workspace** Sends the loaded data formatted as a structure array and named **NetCDF_data** (G1) to the Command Window in MATLAB; the user can then edit the data, create plots, or save.
- **Import data from workspace** Imports the structure array called **NetCDF_data** to the GUI workspace.

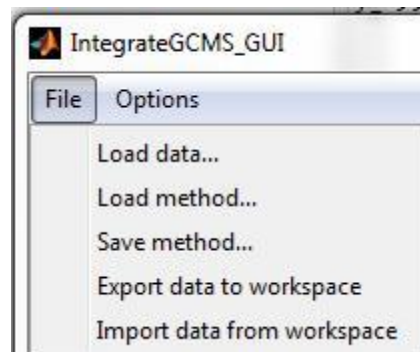


Figure A.6
The File menu.

D5.2 Options Menu (Figure A.7)

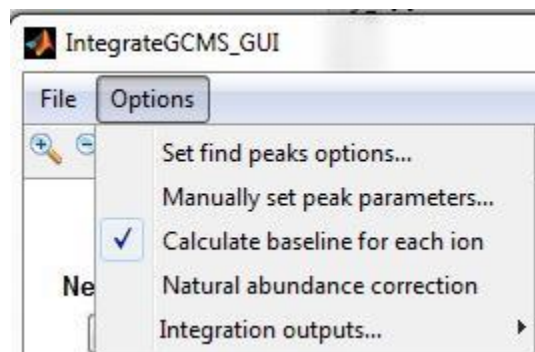


Figure A.7
The *Options* menu.

- **Set find peaks options...** In a new interface (Figure A.8), allows the user to edit the settings used to calculate noise and the baseline as well as to edit the algorithm used to find the peak start and the peak end (see F1).
- **Manually set peak parameters...** Allows the user to edit the baseline, peak start, and peak end values assigned to a given metabolite in a single file (also D1.1).
- **Calculate baseline for each ion** Implements an adjustable baseline algorithm for baseline subtraction; by default, this option is checked.
- **Natural abundance correction** Uses tools described by Fernandez et al. (23) to correct mass isotopomer distributions for natural abundance; by default, this option is unchecked.
- **Integration outputs...** Allows the user to select the desired outputs of integration; by default, *.csv is checked, but the user can also elect to output the data as a MATLAB *.mat file.

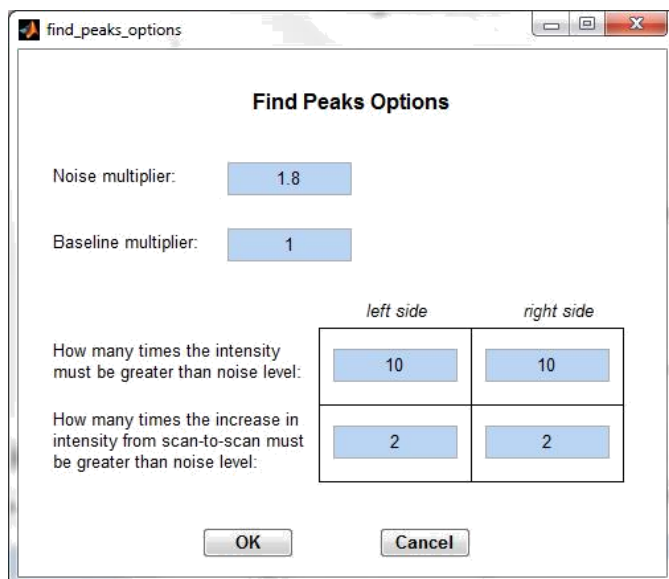













Figure A.8
The *Find Peaks Options* interface allows the user to adjust the settings used in the algorithm to calculate noise and the baseline.

D6 Plot Toolbar

- Note: hover over any icon on the plot toolbar to get the name of the tool.
-  **Zoom in** Turns the cursor into a magnifying glass. Left-click to zoom in, or hold down the left mouse button and draw a box to magnify a specific region of the plot. Right-click within the axis to open an options menu that allows for horizontal or vertical zooming.
-  **Zoom out** Turns the cursor into a magnifying glass. Left-click once to zoom out or double-click to reset the plot. Right-click within the axis to open an options menu that allows for horizontal or vertical zooming.



-  **Pan** Turns the cursor into a hand. Grab within the plot by holding down the left mouse button, then drag to pan through the plot.
-  **Data cursor** The data cursor can be placed on the chromatogram to obtain exact x and y values for the selected point.
-  **Brush/select data tool** Use the brush to make annotations to the plot.
-  **Legend on/off** Turns the plot legend on or off.
-  **Fill axis** Resets all zooming and fills the axis with the plot.
-  **Redraw plot annotations** Upon zooming, peak annotations are obscured. This tool redraws the annotations on the plot.
-  **Remove SICs** Removes all selected ion chromatograms from the plot and unchecks all **Show Ion Trace** boxes (D3.3).
-  **Open GC-MS scan** Opens the selected data file in a new window, allowing the user to review the MS scans in full (D6.1).
-  **Open help document** Opens the *.pdf help document.

D6.1 GC-MS Scan

The highlighted file (D1) is opened in the gcms_scan window when the user clicks the corresponding menu button (D6). gcms_scan contains two axes. The top axis contains the full chromatogram. As in D2, the x-axis is retention time in minutes, and the y-axis is the total ion abundance. The bottom axis shows the MS scan at a user-selected timepoint. The

x-axis shows the ion values (m/z), and the y-axis shows total ion abundance. Both the top and bottom axes can be manipulated with zoom, pan, and cursor tools, as described in D6.

Two additional plot tools are present:

-  **View ion traces** Opens an input dialog box wherein the user can type specific ion (m/z) values to view the trace on the chromatogram (e.g. blue line, Figure A.9).
-  **View MS** Turns the cursor into crosshairs, allowing the user to select a specific point on the chromatogram to view the full MS scan (e.g. the full MS scan at 9.54 minutes is shown in Figure A.9, bottom panel).

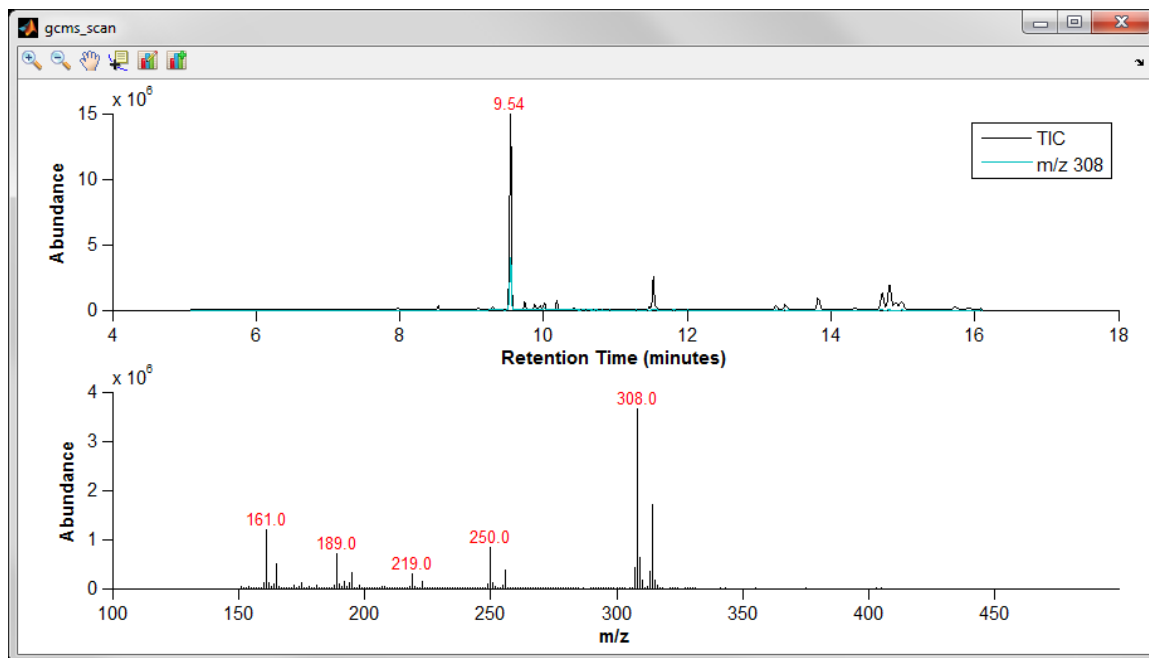


Figure A.9

The `gcms_scan` window allows the user to review the full MS scan at any timepoint in the chromatogram.

E STEP-BY-STEP GUIDE

1. Load GC-MS data in NetCDF format by clicking the **Add** button or from **File > Load data...** (D1 or D5.1)
 - a. The listbox will populate with the loaded filenames, and the chromatogram for the first filename in the list will display in the axis.
2. Load a saved *.m integration method by clicking the **Load** button in the **Integration method panel** (D3.1) or from **File > Load method...** (D5.1)
 - a. For the format of the integration method file, refer to section G2.
 - b. To create a new method, refer to section G3.
3. For each target metabolite, refine the retention time
 - a. Visualizing the main ion traces (D3.3) and the plot tools (D6) can be used to identify the metabolite peak's retention time.
4. Click the **Check** button (D3.1) to command the GUI to locate the target metabolites in each loaded file.
5. Browse through the files in the listbox to verify that the target metabolite(s) were properly defined by the GUI.
 - a. If needed, manually edit peak parameters set in error (D4).
6. Click the **Run** button (D3.1) to integrate with respect to the ranges defined in the method (D3.3) and output a *.csv file with the MIDs.
 - a. For an explanation of the output file, refer to section G4.
7. Save the integration method (D3.1 or D5.1).

F ALGORITHM DETAIL

F1 Defining a metabolite peak

A press of the **Check** button (D3.1) commands the GUI to find a GC-MS peak corresponding to each defined metabolite. The **Check** function returns the retention time of the metabolite peak, the peak start and peak end, and the baseline.

F1.1 Finding the Metabolite

The algorithm uses the **Main Ions** and the estimated **Rel Intensity** defined by the user in the method table (D3.3) to locate the metabolite. The function calculates the probability, p_1 , that the metabolite peak is at a given time value, T , based on the ratio of the relative intensities of the main ions, `MainIonsRelInt`. Then, the function calculates the probability, p_2 , that the metabolite peak is at a given time value, T , based on the retention time, `RetTime`, provided by the user. The most likely timepoint, x , is based on the abundances of the selected ions in the **Main Ions** range, `sum(sim)`, multiplied by p_1 and p_2 .

```
% Determine most likely location of peak based on relative peak values
K = nMainIons*0.1;
p1 = (sum(abs(relsim-repmat(MainIonsRelInt,1,nT)))/K+1).^(-2);

% Determine most likely location of peak based on retention time
K = 0.05; % minutes
p2 = normpdf(T-RetTime,0,K);

% Determine most likely location of metabolite peak
x = sum(sim).*p1.*p2;
idx = find(x==max(x));
idx = idx(1);
timepoint = T(idx);
```

F1.2 Calculating the noise

The sum of the metabolite's **Main Ions** is defined as the variable `cnts`. A built-in smoothing function, `mssgolay` (Figure A.10), is used to smooth `cnts`, and the

smoothed data is defined as `c`. The median of the difference between `cnts` and `c`, multiplied by the **Noise multiplier** (D4 and Figure A.8; the default multiplier is 1.8), is equal to `noise`.

```
% Smooth out data
c = mssgolay([1:1:length(cnts)]', cnts');

% Estimate average noise-intensity or use the minimum noise level of 10
NoiseLB = 10;
noise = max(NoiseLB, options.noise_mult*median(abs(c-cnts)));
```

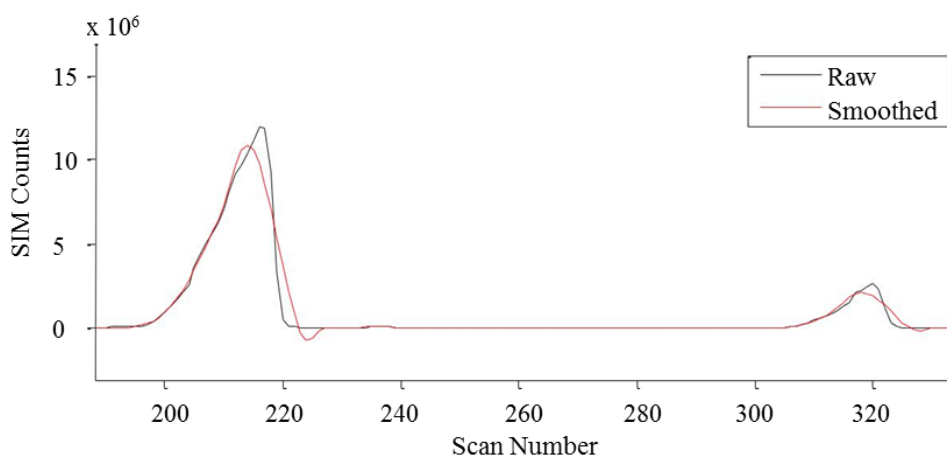


Figure A.10
An example of smoothing the raw, summed selected ion chromatogram using `mssgolay`.

F1.3 Identifying the baseline index and calculating the average baseline

The scan numbers where `cnts <= noise` is set as the baseline index. The index values that are nearest to the metabolite peak, defined as the variable `base`, are used to calculate the average baseline, `bsln`. The average baseline is multiplied by a baseline multiplier, `options.bsln_mult` (D4 and Figure A.8; the default multiplier is 1.0). *Note*: the same index, `base`, is used to calculate the average baseline for every ion in the ion range, using each ion's average abundance over the index.

```
% Set average baseline
bsln = options.bsln_mult*mean(cnts(base));
```

F1.4 Defining the peak start and peak end

From the peak maximum estimated to occur at `timepoint`, the function moves down, one scan at a time in a `while` loop, until the intensity of `c` is at `noise` times a multiplier, `options.lb_mult` (D4 and Figure A.8; the default multiplier is 10), and the change in intensity from scan-to-scan is greater than `noise` times a multiplier, `options.lb_inc` (D4 and Figure A.8; the default is 2). The point where the `while` loop is satisfied is set as the peak start. The same protocol is followed to set the peak end, except the function moves up, one scan at a time in a `while` loop until the conditions are satisfied.

F2 Integration

For each **Integration Range** defined in the method table (D3.3), a MID is calculated. The integration range is set as the variable `SIM`. The summed counts for each ion in `SIM` between peak start and peak end are calculated as `simCnts`. The baselines are subtracted from each ion's `simCnts`, and the total integrated counts are calculated by taking the sum. The counts are then normalized to one, by convention.

```
% sum MS data between peak start and end
sumMS = nansum(MS(peak(1):peak(2),:));

% calculate total ion counts
simCnts = sumMS(:,SIM(n,1):SIM(n,2));

% correct for baseline by subtraction
simCntsCorrected = max(0, simCnts-bsln);

% calculate total integrated counts
tc = sum(simCntsCorrected);

% normalize counts to 1
x = simCntsCorrected'/sum(simCntsCorrected)];
```

G ADDITIONAL INFORMATION

G1 *MATLAB* structure array: NetCDF_data

NetCDF_data is a $1 \times n$ structure array, where n is the number of NetCDF files loaded into the GUI workspace. Each entry has 10 subfields (Table A.1):

Table A.1
Description of NetCDF_data subfields.

Subfield	Description
filename	NetCDF filename in a string, e.g. '00201004.cdf'
RT	The time values, in minutes, in a $t \times 1$ matrix
TIC	The total ion counts corresponding to each time in RT ; a $t \times 1$ matrix
SIC	The ion counts for each ion at each time in RT ; an $m \times t$ matrix, where m is the ion mass. Unless the collected data exceeds m/z 500, the SIC is by default $500 \times t$
info	The metadata included in the file. Subfields within info: netcdf_stamp with the collection timestamp, sample_name , operator , time (corresponds to t), and scans
timepoints	The time value corresponding to the maximum of each metabolite peak; a $1 \times p$ matrix, where p is the total number of metabolites in the integration method
peak_start	The time value corresponding to the peak start for each metabolite peak; a $1 \times p$ matrix
peak_end	The time value corresponding to the peak end for each metabolite peak; a $1 \times p$ matrix
baseline	The subfield SIM contains the baseline for each ion in the integration range for each metabolite
avg_baseline	The average baseline for each metabolite peak; a $1 \times p$ matrix

G2 *Format of an integration method file*

The *.m integration method file must be defined as a function called MSLib. Each metabolite in the function is defined in a structure array as follows:

```
function MSLib=Aldo_method()

MSLib = struct('Name', {},
    'RetTime', {}, 'MainIons', {}, 'MainIonsRelInt', {}, 'SelectedIons', {},
    'SelectedIonsFormula', {}, 'SelectedIonsLabeled', {});
Item.Name = 'Aldo';
Item.RetTime = 12.06;
Item.MainIons = [173,178; 259,265; 284,289; 370,376];
Item.MainIonsRelInt = [100; 24; 12; 14];
Item.SelectedIons = [173,178; 259,265; 284,289; 370,376];
Item.SelectedIonsFormula = {'C8H13O4'; 'C12H19O6'; 'C13H18O6N'; 'C17H24O8N'};
Item.SelectedIonsLabeled = {'H3'; 'H4'; 'H3'; 'H4'};
MSLib(end+1) = Item;
```

A new metabolite can be added within the GUI (*G3*) or directly to the end of the method

*.m file, e.g.:

```
Item.Name = 'New Metabolite';
Item.RetTime = 8.52;
Item.MainIons = [210,218; 341,350];
Item.MainIonsRelInt = [100; 70];
Item.SelectedIons = [210, 218];
Item.SelectedIonsFormula = {'C17H24O8N'};
Item.SelectedIonsLabeled = {'H3'};
MSLib(end+1) = Item;
```

The format must be exact to ensure proper loading. `Item.Name` is used in the Metabolite pull-down menu and written to the **Name:** edit textbox (*D3.2*). `Item.RetTime` is written in the **Retention Time (min):** edit textbox within the GUI (*D3.2*), and the remaining entries are written to specific columns in the method table (Table A.2, *D3.3*).

Table A.2
Correlation between MSLib subfields and method table columns

MSLib subfield	Method table column
MainIons	Main Ions
MainIonsRelInt	Rel Intensity
SelectedIons	Integration Range(s)
SelectedIonsFormula	Formula
SelectedIonsLabeled	Labels

G3 Creating a new integration method

1. The user must have knowledge of the target metabolite's chemical properties, including what fragments are formed by ionization in the MS and the chemical

formula of the fragments of interest. This is best obtained using standards and other tools such as NIST libraries or AMDIS.

2. In the GUI, define the name of the first target metabolite
 - a. the **Metabolite** pop-up menu (D3.2) should read **Add new peak** until the **Name** is defined; then, the menu will populate with the new name (Figure A.11)

The figure shows two side-by-side screenshots of a software interface. Each screenshot has a 'Metabolite:' label followed by a dropdown menu. In the left screenshot, the dropdown menu shows 'Add new peak'. Below it are two text input fields: 'Name:' and 'Retention Time (min):'. In the right screenshot, the dropdown menu shows 'NewMetab'. The 'Name:' text box now contains 'NewMetab'. The 'Retention Time (min):' text box is empty. Both text boxes have a small red 'X' icon to their right.

Figure A.11

With *Add new peak* selected in the *Metabolite* menu, define the name of the new metabolite

3. Estimate the retention time for the target metabolite, and fill in the **Retention Time (min)** field (Figure A.11)
4. In the **Main Ions** column in the method table (D3.3), set the ion ranges that will be used to identify the target metabolite
 - a. At least two ranges are suggested for best results
5. In the **Rel Intensity** column, estimate the relative intensity of each main ion range
 - a. This process can be facilitated using plot tools. Turn on the ion traces for each main ion range and zoom in on the target peak. Use the data cursor tool to obtain the ion abundances. Set the most abundant ion range to 100, then scale the remaining ranges relative to this range. Accurate estimates facilitate proper identification of the metabolite by the GUI.

- b. For example (Figure A.12):
- i. m/z 173-178 is the most abundant range, so the **Rel Intensity** is set to 100.
 - ii. m/z 370-376 has a maximum abundance of 2.961e+06; compared to m/z 173-178, this is approximately 60%. Therefore, the **Rel Intensity** is set to 60.
 - iii. m/z 259-265 has **Rel Intensity** of approximately 50.
 - iv. m/z 284-289 has **Rel Intensity** of approximately 30.

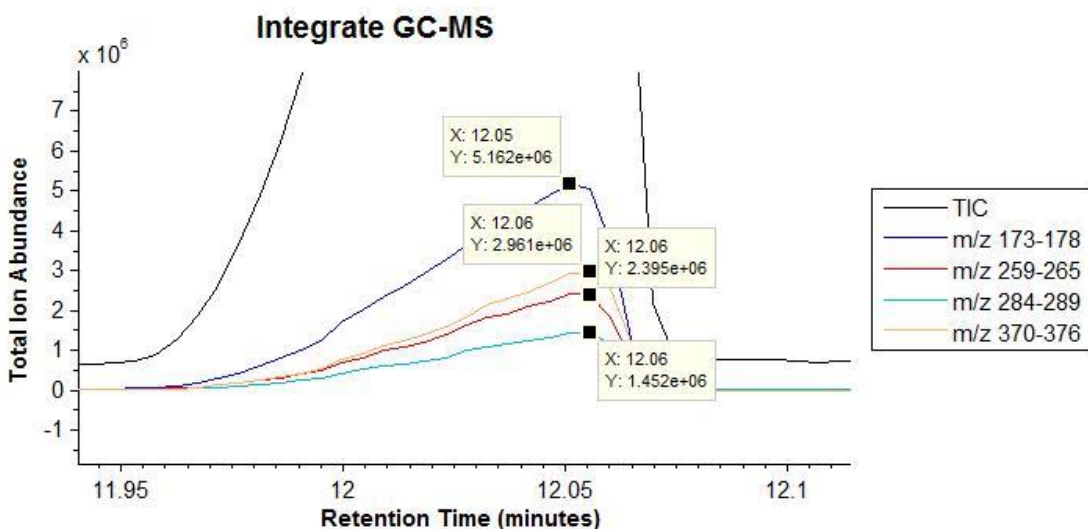


Figure A.12
Estimating relative intensities of main ion ranges using GUI plot tools.

6. In the **Integration Range(s)** column, identify the ion ranges for which MIDs are required.
7. (*Optional*) Provide a chemical formula for the fragment defined by each integration range in order to obtain a theoretical MID and to correct for natural abundance

8. (*Optional*) Provide the number of atoms that could be labeled in the fragment by the stable isotope tracer; for example, if the fragment has five carbons that could be labeled, the Labels column should read C5.
9. Add another metabolite to the method by selecting **Add new peak** from the **Metabolite** pull-down menu; follow steps 1-8.
10. Save the method using the **Save** button (D3.1) or from **File > Save method...** (D5.1)

G4 Understanding the output file

The *.csv file that is created by the GUI can be opened in Excel in other spreadsheet software. The spreadsheet is separated into four sections: (1) **Samples**; (2) **Retention Times (min.)**; (3) **Total ion counts**; (4) **Mass isotopomer abundances**.

The **Samples** sections lists the sample names the user provided during the GC-MS run. The **GCMS ID** is the number assigned to each sample during the GC-MS run. For the Agilent system used to produce the data shown in Figure A.13, the ID number contains information on the sample number, replicate number, and injection number. For example, “702018” refers to sample #7, replicate #2, and injection #18.

The **Retention Times (min.)** section lists the retention time for each metabolite in the integration method. The time reported occurs at the estimated maximum intensity (*FI.I*).

The **Total ion counts** section lists the total integrated counts for each ion range defined in the **Integration Range(s)** column in the method table (D3.3). While only the first ion is listed (e.g. *Aldo 173* in Figure A.13), the total ion count is the sum of the abundances of all of the ions in the integration range from the peak start to the peak end, with the baseline subtracted (F2).

The **Mass isotopomer abundances** section presents the MID for each metabolite and each integration range. In the final column, after the MIDs for all samples have been written, a column titled *Theory* is written (Figure A.13). This column contains the theoretical MID for an unlabeled sample with the chemical formula defined in the **Formula** column of the method table (D3.3).

	A	B	C	D	E	F	G	H	I	L
1	Samples									
2	Names	Standard1	Standard1	Standard2	Standard2	Expt1	Expt1	Expt2	Expt2	
3	GCMS ID	101002	102003	201004	202005	301007	302008	701017	702018	
4										
5	Retention Times (min.)									
6	Aldo	12.04	12.04	12.03	12.04	12.03	12.03	12.04	12.04	
7										
8	Total ion counts									
9	Aldo 173	8.23E+07	8.02E+07	5.62E+07	5.59E+07	5.13E+07	4.66E+07	4.05E+07	3.65E+07	
10	Aldo 259	3.84E+07	3.72E+07	2.51E+07	2.52E+07	2.29E+07	2.06E+07	1.81E+07	1.61E+07	
11	Aldo 284	2.30E+07	2.24E+07	1.51E+07	1.51E+07	1.38E+07	1.24E+07	1.09E+07	9.74E+06	
12	Aldo 370	4.70E+07	4.53E+07	3.03E+07	3.01E+07	2.76E+07	2.47E+07	2.18E+07	1.96E+07	
13										
14	Mass isotopomer abundances									
15	GCMS ID	101002	102003	201004	202005	301007	302008	701017	702018	Theory
16	Aldo173 (M0)	0.9004	0.9004	0.9015	0.9022	0.8368	0.8385	0.8128	0.8181	0.9060
17	Aldo174 (M1)	0.0823	0.0820	0.0818	0.0812	0.1317	0.1309	0.1536	0.1516	0.0825
18	Aldo175 (M2)	0.0110	0.0110	0.0105	0.0107	0.0234	0.0235	0.0254	0.0249	0.0107
19	Aldo176 (M3)	0.0009	0.0009	0.0009	0.0008	0.0024	0.0023	0.0028	0.0024	0.0007
20	Aldo177 (M4)	0.0003	0.0004	0.0005	0.0004	0.0009	0.0004	0.0008	0.0000	0.0001
21	Aldo178 (M5)	0.0051	0.0051	0.0048	0.0047	0.0048	0.0043	0.0046	0.0030	0.0000
22										
23	Aldo259 (M0)	0.8616	0.8606	0.8626	0.8640	0.7822	0.7813	0.7529	0.7519	0.8624
24	Aldo260 (M1)	0.1168	0.1170	0.1161	0.1162	0.1728	0.1755	0.1964	0.1979	0.1177
25	Aldo261 (M2)	0.0177	0.0179	0.0173	0.0167	0.0363	0.0347	0.0404	0.0411	0.0180
26	Aldo262 (M3)	0.0017	0.0018	0.0017	0.0016	0.0051	0.0044	0.0057	0.0053	0.0017
27	Aldo263 (M4)	0.0011	0.0009	0.0008	0.0006	0.0014	0.0013	0.0016	0.0015	0.0002
28	Aldo264 (M5)	0.0005	0.0009	0.0008	0.0004	0.0010	0.0015	0.0019	0.0014	0.0000
29	Aldo265 (M6)	0.0006	0.0009	0.0008	0.0006	0.0012	0.0012	0.0012	0.0009	0.0000
30										
31	Aldo284 (M0)	0.8460	0.8447	0.8461	0.8469	0.7744	0.7773	0.7569	0.7621	0.8501
32	Aldo285 (M1)	0.1322	0.1322	0.1322	0.1322	0.1322	0.1322	0.1322	0.1322	0.1322

Figure A.13
Screenshot of integrate_gcms output file in Excel.

APPENDIX B

USER MANUAL FOR THE POSITIONAL ANALYSIS GUI

INTRODUCTION

gpa is a MATLAB-based graphical user interface (GUI) designed to guide a user through the process of analyzing mass isotopomer distribution (MID) data from six distinct fragment ions in order to estimate the positional enrichment of deuterium (^2H) on glucose. The methodology was adapted from Antoniewicz et al. (2). An overview of the method is shown in Figure 1.2.

Sample glucose is derivatized through three different protocols. The chemically distinct glucose derivatives – glucose aldonitrile pentapropionate, glucose methyloxime pentapropionate, and glucose 1,2,5,6-di-isopropylidene propionate – elute at different times by gas chromatography and fragment into different ions by mass spectrometry. MIDs obtained from six separate ions are the required inputs into the GUI. These MIDs are used in a least squares (LSQ) regression to estimate the isotopic enrichment at each carbon position of the parent glucose molecule (Figure 1.2).

The six MIDs are linearly combined in a single vector in MATLAB (MID_M). The theoretical MIDs expected for each of the 2^7 (or 128) possible hydrogen isotopomers of glucose are calculated based on natural isotope abundances and the atomic formula of each fragment. Theoretical MIDs are combined into a matrix, T . Multiplying T by a fractional contribution matrix, x , produces a vector of MIDs (MID_C) expected from the x -defined mixture of hydrogen isotopomers (Equation B.1). The LSQ regression minimizes the difference between MID_M and MID_C by manipulating x (Equation B.2). Therefore, the first

output of the computational method is an estimation of the relative abundance of each hydrogen isotopomer in the sample. Multiplying this output, x , by a transformation matrix that defines each hydrogen isotopomer in terms of zeros, representing unlabeled carbons, and ones, representing ^2H -labeled carbons, produces a second output that quantifies the total ^2H enrichment at each of the six carbon positions of glucose.

$$MID_C = T \times x \quad (\text{B.1})$$

$$\min \sum (MID_C - MID_M)^2 \quad (\text{B.2})$$

SYSTEM REQUIREMENTS

- Windows 7 or later
- MATLAB R2011a or later, including:
 - Bioinformatics toolbox
 - Statistics toolbox

OPTIONAL SOFTWARE

- **integrate_gcms**
 - to obtain accurate MIDs from raw GC-MS data
 - available from the Young lab
- **Isotopically Nonstationary Compartment Analysis (INCA) (77)**
 - provides a secondary method for positional analysis for low enrichment experiments
 - available from <http://mfa.vueinnovations.com/>

GETTING STARTED

Installation

The GUI is provided in a *.zip folder. Extract the folder to any directory. The folder should contain a function **gpa.m** and three folders: **gpa_bin**, **gpa_help**, and **gpa_test**.

Launching the GUI

Start MATLAB and change the working directory to the folder containing **gpa.m**. Type **gpa** into the Command Window and press enter to launch the GUI (Figure B.1). The GUI can be resized as needed to fit your screen by using the maximize function or by grabbing the edge of the interface and dragging to adjust the width and/or height.

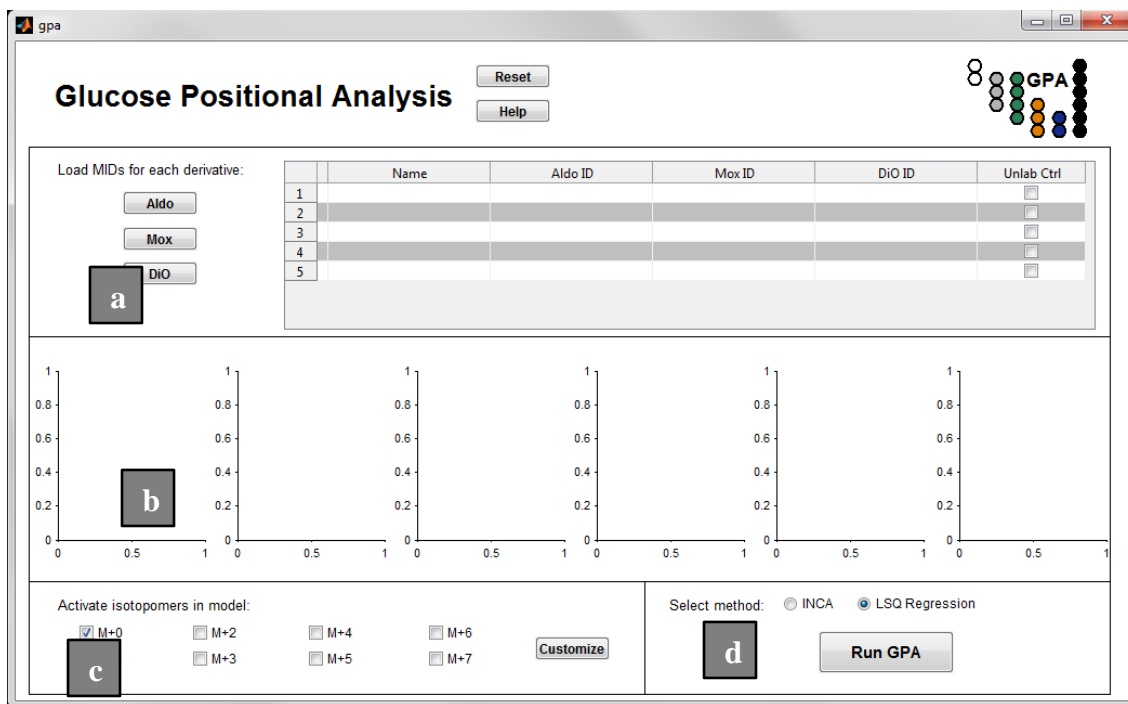


Figure B.1

The launched gpa GUI. The GUI is divided into four major sections. MID data are loaded from *.csv files in *a*. MID data are visualized in *b*. The active isotopomers in the model are adjusted in *c*. In *d*, the user runs the analysis on the loaded data.

STEP-BY-STEP GUIDE

1. Obtain MIDs

Accurate MIDs are necessary for the methodology to produce accurate enrichment estimates. Root mean squared error (*RMSE*), measured by comparing MIDs from n unlabeled samples (MID_M) to the theoretical MID (MID_T), should not exceed 1% for any of the six fragments (Equation B.3). Work by Antoniewicz et al. (1) determined that a fixed-width, adjustable baseline integration produces the most accurate MIDs. The Young lab's **integrate_gcms** GUI utilizes this algorithm, and the output *.csv files are directly compatible with **gpa**. Example *.csv files are included in the **gpa_test** folder.

$$RMSE = \max \left(\sqrt{\frac{\sum_{i=1}^n (MID_M - MID_T)^2}{n}} \right) \quad (\text{B.3})$$

2. Load MIDs

Three separate *.csv files are loaded into the GUI. The MIDs for m/z 173, 259, 284, and 370, obtained from the aldonitrile derivative of glucose, are loaded by clicking the **Aldo** button (Figure B.2). The MID for m/z 145 is loaded by clicking the **Mox** button. The MID for m/z 301 is loaded by clicking the **DiO** button. In addition to the MIDs, the GUI imports the sample name and GCMS ID numbers to help the user navigate the data. Injection replicates are automatically averaged, and the GCMS IDs for these replicates are combined (e.g. in Figure B.2, the combined GCMS ID 013[01,02][029,030] indicates that the vial in position #13 was tested twice in injections #29 and #30). If loading is successful, the loading buttons are disabled, and the sample names and combined GCMS IDs populate the GUI table (Figure B.2).

Load MIDs for each derivative:

	Name	Aldo ID	Mox ID	DiO ID	Unlab Ctrl
1	+ Standard1	001[01,02][002,003]	001[01,02][002,003]	001[01,02][002,003]	<input type="checkbox"/>
2	Standard2	002[01,02][004,005]	002[01,02][004,005]	002[01,02][004,005]	<input type="checkbox"/>
3	Expt1	003[01,02][007,008]	003[01,02][007,008]	003[01,02][007,008]	<input type="checkbox"/>
4	Expt2	007[01,02][017,018]	007[01,02][017,018]	007[01,02][017,018]	<input type="checkbox"/>
5	Expt3	013[01,02][029,030]	013[01,02][029,030]	013[01,02][029,030]	<input type="checkbox"/>

Figure B.2

The GUI table is populated with sample names and ID numbers. In this example, the three files were loaded from the **gpa_test** folder. The *A_test.csv* file was loaded by the **Aldo** button. *M_test.csv* was loaded by clicking **Mox**. The **DiO** button was used to load *D_test.csv*.

3. View MIDs

The GUI axes display the MIDs for each of the six ions (Figure B.3). The y-axes show relative ion abundance. The x-axes show the isotopomer distribution from an unlabeled ($M+0$) to fully labeled ($M+n$) state. The active sample has a + in the first column of the GUI table (e.g. in Figure B.2, *Standard1* is the active sample). To change the active sample, the user can click on any cell in that sample's row (Figure B.2).

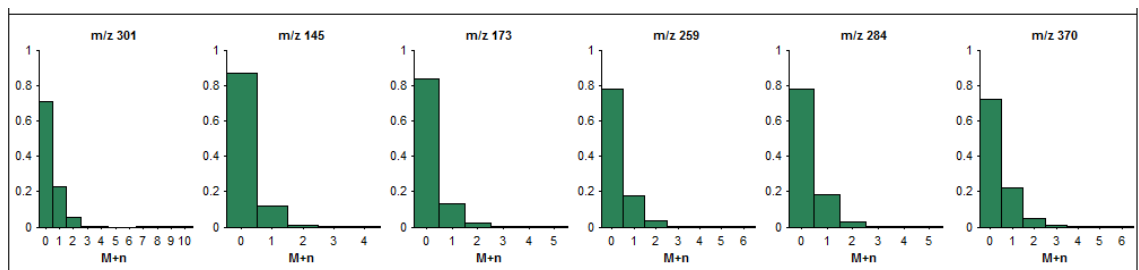


Figure B.3

The GUI axes display the sample MIDs for each fragment. In this example, the MIDs for *Expt1* from **gpa_test** are shown.

4. Add weights (optional)

Work in the Young lab supports the use of weighting in order to produce the most accurate positional enrichment estimates. Each fragment is weighted based on the inverse of its RMSE (Equation B.3), which the GUI calculates from unlabeled control samples (**Unlab Ctrl**) checked by the user in the GUI table (Figure B.4).

	Name	Aldo ID	Mox ID	DiO ID	Unlab Ctrl
1	+ Standard1	001[01,02][002,003]	001[01,02][002,003]	001[01,02][002,003]	<input checked="" type="checkbox"/>
2	Standard2	002[01,02][004,005]	002[01,02][004,005]	002[01,02][004,005]	<input checked="" type="checkbox"/>
3	Expt1	003[01,02][007,008]	003[01,02][007,008]	003[01,02][007,008]	<input type="checkbox"/>
4	Expt2	007[01,02][017,018]	007[01,02][017,018]	007[01,02][017,018]	<input type="checkbox"/>
5	Expt3	013[01,02][029,030]	013[01,02][029,030]	013[01,02][029,030]	<input type="checkbox"/>

Figure B.4

Unlabeled control samples are used for weighting fragments in the LSQ regression. For the test case, *Standard1* and *Standard2* from *gpa_test* are checked as unlabeled control samples.

5. Adjust active isotopomers in the model (optional)

Because there are seven hydrogens on glucose, there are 128 possible hydrogen isotopomers in the full model. If assumptions can be applied to limit the number of active isotopomers, the analysis produces better enrichment estimates. All of the isotopomers with one ^2H can be turned on by checking the $M+1$ box, two ^2H by checking the $M+2$ box, etc. The fully unlabeled isotopomer is activated by checking $M+0$, and the fully labeled isotopomer is activated by checking the $M+7$ box (Figure B.5).

Activate isotopomers in model:

<input checked="" type="checkbox"/> M+0	<input type="checkbox"/> M+2	<input type="checkbox"/> M+4	<input type="checkbox"/> M+6	<input type="button" value="Customize"/>
<input checked="" type="checkbox"/> M+1	<input type="checkbox"/> M+3	<input type="checkbox"/> M+5	<input type="checkbox"/> M+7	

Figure B.5

The active isotopomers in the model can be adjusted by the user. The data collected for *gpa_test* was from an *in vivo* experiment that used infused $^2\text{H}_2\text{O}$ and $[6,6-^2\text{H}_2]\text{glucose}$ to measure gluconeogenic flux and total glucose production, respectively. Based on the experimental design, we hypothesized that $M+2$ isotopomers would be improbable. Therefore, only $M+0$ and $M+1$ isotopomers were active for this analysis.

Specific isotopomers can be activated by clicking the **Customize** button. A custom dialog box appears after the **Customize** button is clicked (Figure B.6). The labeling state of each carbon, from the first carbon (C1) to the sixth carbon (C6), can be adjusted by the user. A

0 represents an unlabeled carbon. A 1 indicates a single ^2H at that carbon position. C6 may also have a value of 2. To save the changes, the user must click the **Return to GPA** button (Figure B.6).

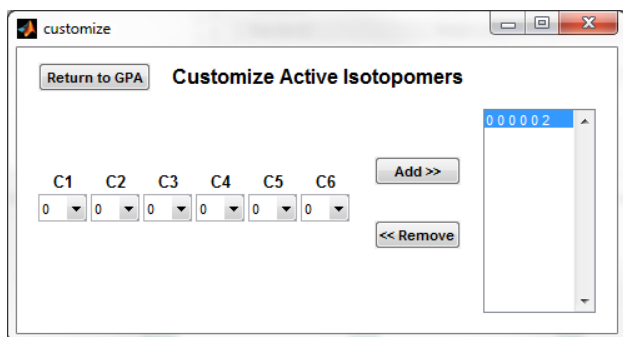


Figure B.6

The user can activate specific isotomers in the model using *Customize*. Each carbon position is given a numerical value that indicates the number of ^2H bound. For the test case, the only probable $M+2$ isotopomer in the model was from the $[6,6-^2\text{H}_2]$ glucose tracer. Therefore, this single $M+2$ isotopomer, represented by the sequence **0 0 0 0 0 2**, was added to the model.

6. Run the LSQ regression

By default, the *LSQ Regression* methodology is active. The user clicks the **Run GPA** button to begin the analysis (Figure B.7).

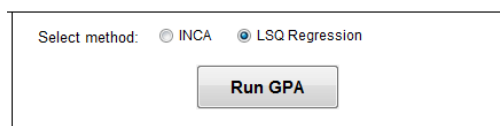


Figure B.7

A click of the Run GPA button initiates the analysis.

7. Analyze the output files

The LSQ regression produces two separate output files. The first file contains the fractional contribution values, x , for each sample (see **INTRODUCTION**). The first

column contains the numerical sequences for each active isotopomer in the model, using the same 0/1/2 representation detailed in step 5 (Figure B.8).

The second output is the result of multiplying the fractional contribution values, x , by a transformation matrix as described in the **INTRODUCTION**. The A_v column for each sample shows the average estimated enrichment (%) at each carbon position (Figure B.9). If many isotopomers are active in the model, this output provides a concise summary of enrichment. The best-fit data is plotted on the GUI axes to visualize the optimization (Figure B.10).

	A	B	C	D	E	F
1	Isotopomers	<i>Standard1</i>	<i>Standard2</i>	<i>Expt1</i>	<i>Expt2</i>	<i>Expt3</i>
2	000000	100.00	100.00	84.77	79.04	83.84
3	000001	0.00	0.00	1.83	2.69	2.14
4	000001	0.00	0.00	1.83	2.69	2.14
5	000002	0.01	0.00	1.24	1.62	0.95
6	000010	0.00	0.00	2.25	2.94	2.15
7	000100	0.00	0.00	1.88	2.55	2.01
8	001000	0.00	0.00	0.39	1.66	1.22
9	010000	0.00	0.00	5.80	5.94	5.16
10	100000	0.00	0.00	0.00	0.86	0.40

Figure B.8

The first output file contains the fractional contribution values for each isotopomer. Each isotopomer is represented by a numerical sequence. The six digits represent each carbon in glucose. A 0 indicates carbon with ^1H bound, 1 with ^2H bound, and 2 with two ^2H bound (C6 only). The test case used a model with nine active isotopomers. *Standard1* and *Standard2* were unlabeled samples. The regression determined that 100% of the glucose in these standards was naturally labeled, as expected. The experimental samples, *Expt1-Expt*, have a significant abundance of [2- ^2H]glucose and [5- ^2H]glucose, as expected for gluconeogenic experiments.

A	B	C	D	E	F	G	H	I	J	K	
1	Standard1		Standard2		Expt1		Expt2		Expt3		
2	Av	Std	Av	Std	Av	Std	Av	Std	Av	Std	
3	C1	0.00	0.00	0.00	0.00	0.00	0.87	0.05	0.41	0.03	
4	C2	0.00	0.00	0.00	0.00	5.83	0.02	5.97	0.06	5.18	0.04
5	C3	0.00	0.00	0.00	0.00	0.39	0.02	1.67	0.04	1.23	0.03
6	C4	0.00	0.00	0.00	0.00	1.89	0.02	2.56	0.03	2.01	0.02
7	C5	0.00	0.00	0.00	0.00	2.26	0.02	2.95	0.04	2.15	0.02
8	C6	0.01	0.01	0.00	0.00	3.08	0.01	4.34	0.03	3.10	0.02

Figure B.9
The second output file contains the total enrichment estimates (%) at each carbon position.

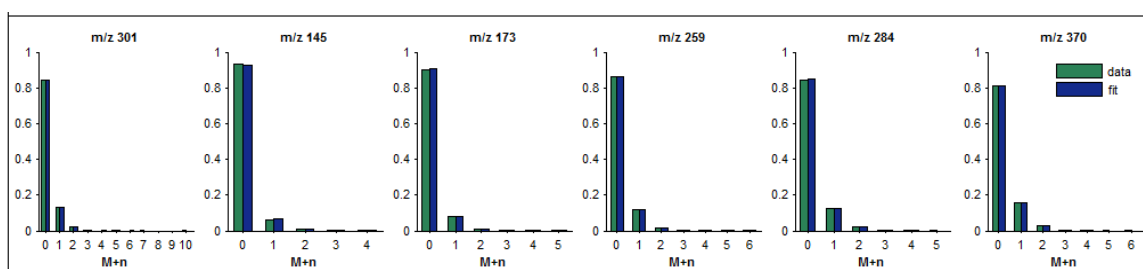


Figure B.10
After the analysis has completed, the minimized MIDs are plotted (*fit*) with the experimental values (*data*).

8. Run positional analysis using INCA (optional)

A complementary positional analysis can be performed by a secondary software program, INCA. At this time, analysis is constrained to low enrichment experiments that use the nine isotopomer model shown in Figure B.11. The output file (Figure B.11) details both isotopomer abundances and enrichment estimates. In addition, INCA evaluates the goodness-of-fit and reports a sum of squared residuals (*SSR*) value. The lower (*LB95*) and upper (*UB95*) bounds of the 95% confidence intervals are also reported.

	A	B	C	D	E	F	G
1			Standard1				
2			SSR 5.99	DOF 29			
3			<i>Value</i>	<i>SE</i>	<i>LB95</i>	<i>UB95</i>	<i>V</i>
4	D1	D1 -> Sink	0.00	0.85	0.00	0.37	
5	D2	D2 -> Sink	0.00	0.98	0.00	0.23	
6	D3	D3 -> Sink	0.00	0.66	0.00	0.29	
7	D4	D4 -> Sink	0.00	0.57	0.00	0.15	
8	D5	D5 -> Sink	0.00	0.58	0.00	0.16	
9	D6	2*D6 -> Sink	0.00	0.40	0.00	0.09	
10	D66	Glucose.66 -> Glucose	0.00	0.13	0.00	0.23	
11	Unlabeled	Glucose.u -> Glucose	100.00	0.44	99.59	100.00	100
12	H1	Glucose.1 -> Glucose + D1	0.00	0.85	0.00	0.37	
13	H2	Glucose.2 -> Glucose + D2	0.00	0.98	0.00	0.23	
14	H3	Glucose.3 -> Glucose + D3	0.00	0.66	0.00	0.29	
15	H4	Glucose.4 -> Glucose + D4	0.00	0.57	0.00	0.15	
16	H5	Glucose.5 -> Glucose + D5	0.00	0.58	0.00	0.16	
17	H6	Glucose.6 -> Glucose + D6	0.00	0.80	0.00	0.19	
18	Glucose	Glucose -> Glucose.ext	100.00	0.00	100.00	100.00	100
19							

Figure B.11

The INCA output details isotopomer abundances (*H1-H6*), average enrichment values (*D1-D6*), and an evaluation of the goodness-of-fit (SSR; 95% confidence intervals *LB95* and *UB95*).

9. Reset the GUI

The user can press the **Reset** button at the top of the GUI to clear all loaded data (Figure B.12).

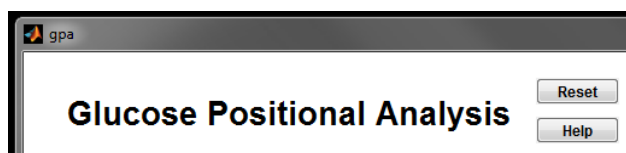


Figure B.12

The **Reset** button is used to clear all data from the GUI.

APPENDIX C

DERIVATION OF GLUCOSE CYCLING EQUATION

The model shown in Figure 3.1 defines the rate of glucose phosphorylation by glucokinase as v_1 , the rate of G6P hydrolysis by G6pc2 as v_2 , and the net glucose uptake as v_{net} . Based on this model, we derived simplified balance equations to describe the change in the MID of extracellular glucose over time as a result of glucose cycling. Let A represent the fractional abundance of the M+7 mass isotopomer of glucose after correction for natural isotope abundance. A mass balance on the M+7 mass isotopomer gives the following differential equation

$$\frac{d(CA)}{dt} = C \frac{dA}{dt} + A \frac{dC}{dt} = -v_1 A \frac{N}{V} \quad (\text{C.1})$$

where C is the total glucose concentration in the extracellular medium, V is the liquid volume in each well (=175 μL), and N is the number of islets in each well. A mass balance on total glucose also gives the following equation

$$\frac{dC}{dt} = -v_{net} \frac{N}{V} \quad (\text{C.2})$$

Rearranging this equation to solve for $\frac{N}{V}$ and substituting the result into Equation C.1 gives the following balance

$$C \frac{dA}{dt} = \frac{v_2}{v_{net}} A \frac{dC}{dt} \quad (\text{C.3})$$

where we have used the relationship $v_{net} = v_1 - v_2$ to simplify the result.

In preliminary experiments in which islets were incubated with a doubly labeled [U-¹³C₆; 1,2,3,4,5,6,6-²H₇]glucose tracer, we observed that a negligible amount of the M+13 tracer was completely de-deuterated to form M+6 glucose (data not shown). Therefore, in our experiments with the D7-glucose tracer, we assumed that none of the tracer was completely de-deuterated to form M+0 glucose and that the increase in M+1 through M+6 fractional abundances must balance the decrease in M+7 fractional abundance over time. If we let B represent the sum of the M+1 through M+6 fractional abundances, this assumption implies that $\frac{dB}{dt} = -\frac{dA}{dt}$, and therefore the sum $A+B$ is constant. Dividing Equation C.3 by $A+B$ gives the following result

$$C \frac{dA'}{dt} = \frac{v_2}{v_{net}} A' \frac{dC}{dt} \quad (\text{C.4})$$

where A' is the ratio $\frac{A}{A+B}$. In contrast to Equation C.3, this equation is normalized to remove the effects of the M+0 mass isotopomer abundance, an adjustment that was found to improve precision of the cycling calculation by removing variability associated with unintended carryover of unlabeled glucose from the preculture. Integrating Equation C.4 with respect to time gives the final result

$$\ln(A') = \frac{v_2}{v_{net}} \ln(C) + D \quad (\text{C.5})$$

where D is a constant of integration whose value depends on the initial enrichment and concentration of glucose in the culture medium. Therefore, the slope of the $\ln(A')$ versus $\ln(C)$ plot can be used to estimate the cycling rate as a percentage of uptake v_2/v_{net} .

APPENDIX D

USER MANUAL FOR THE BATCH GUI

Introduction

inca_batch is a MATLAB-based graphical user interface (GUI) designed to batch data import, export, and fitting within the framework of the INCA environment (77). The GUI significantly reduces analysis time.

Getting Started

Extract the contents of the batch folder into the INCA directory. Open MATLAB and launch INCA. In the *Current Folder* window, right-click on the batch folder and add it to the path. Launch the batch GUI by typing **inca_batch** on the command line (Figure D.1).

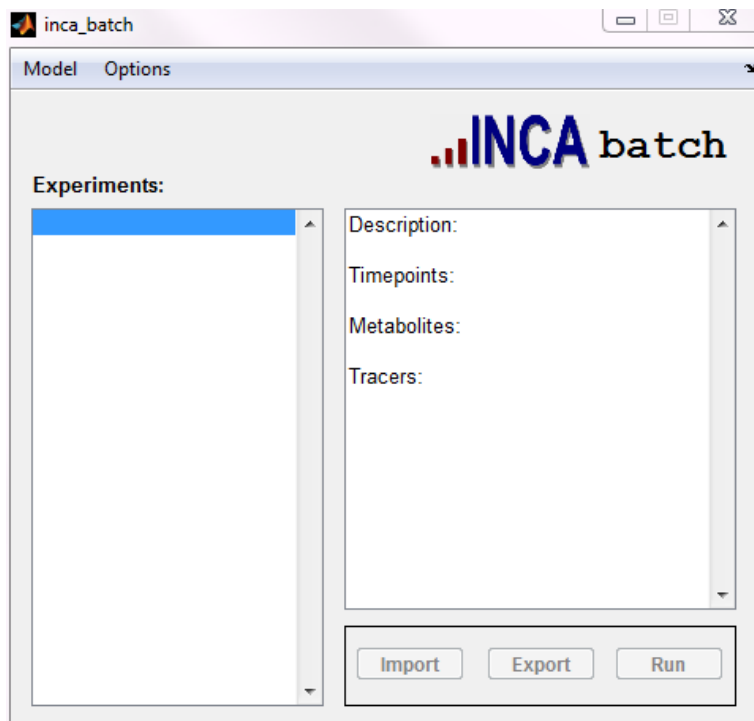


Figure D.1
The initialized inca_batch GUI

Import Data

1. Load a model from the **Model** menu (**Model >> Load**).
 - a. The model should contain at least one experiment that can act as a template for additional experiments. The template experiment should define all of the metabolites of interest.
 - b. *Example:* load **mod_test.mat** in **batch/example1** (Figure D.2)

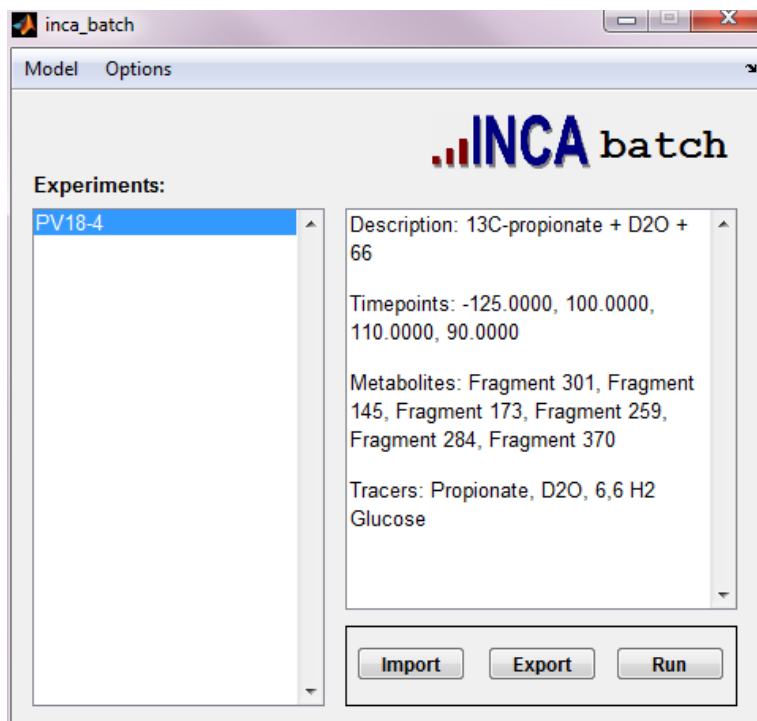


Figure D.2
The batch GUI with **mod_test** loaded. The box on the left-hand side displays the experiment names, while the box on the right-hand side displays a summary of the selected experiment.

2. Organize MIDs for additional experiments in an Excel spreadsheet as in Figure D.3.
 - a. The spreadsheet must be formatted as shown in the examples. Of note, the metabolite identifiers in the first column must exactly match the metabolite names defined in the INCA model.
 - b. *Example:* see **MIDs_test.xlsx** in **batch/example1**

	A	B	C	D	E	F	G	H	I	J	K	L	M
1		PV18-7	PV18-7	PV18-7	PV18-7	PV18-7	PV18-7	PV18-7	PV18-7	PV18-9	PV18-9	PV18-9	PV18-9
2		Av	SE	Av	SE	Av	SE	Av	SE	Av	SE	Av	SE
3		-125	-125	90	90	100	100	110	110	-125	-125	90	90
4	Fragment 173	0.9047	0.0038	0.6164	0.0038	0.6079	0.0038	0.6032	0.0038	0.9025	0.0038	0.6178	0.0038
5	Fragment 173	0.0798	0.0038	0.1671	0.0038	0.1677	0.0038	0.1706	0.0038	0.0822	0.0038	0.1685	0.0038
6	Fragment 173	0.0115	0.0038	0.1873	0.0038	0.1956	0.0038	0.1957	0.0038	0.0120	0.0038	0.1845	0.0038
7	Fragment 173	0.0020	0.0038	0.0249	0.0038	0.0241	0.0038	0.0260	0.0038	0.0019	0.0038	0.0248	0.0038
8	Fragment 173	0.0020	0.0038	0.0043	0.0038	0.0046	0.0038	0.0046	0.0038	0.0015	0.0038	0.0044	0.0038
9		-125	-125	90	90	100	100	110	110	-125	-125	90	90
10	Fragment 259	0.8611	0.0025	0.5545	0.0025	0.5470	0.0025	0.5380	0.0025	0.8609	0.0025	0.5556	0.0025
11	Fragment 259	0.1152	0.0025	0.1913	0.0025	0.1947	0.0025	0.1981	0.0025	0.1162	0.0025	0.1950	0.0025
12	Fragment 259	0.0198	0.0025	0.1738	0.0025	0.1766	0.0025	0.1810	0.0025	0.0188	0.0025	0.1643	0.0025
13	Fragment 259	0.0029	0.0025	0.0667	0.0025	0.0668	0.0025	0.0681	0.0025	0.0031	0.0025	0.0696	0.0025
14	Fragment 259	0.0010	0.0025	0.0137	0.0025	0.0148	0.0025	0.0148	0.0025	0.0010	0.0025	0.0156	0.0025
15		-125	-125	90	90	100	100	110	110	-125	-125	90	90
16	Fragment 284	0.8461	0.0040	0.5947	0.0040	0.5968	0.0040	0.5842	0.0040	0.8428	0.0040	0.5851	0.0040
17	Fragment 284	0.1235	0.0040	0.2306	0.0040	0.2388	0.0040	0.2359	0.0040	0.1312	0.0040	0.2355	0.0040
18	Fragment 284	0.0222	0.0040	0.1048	0.0040	0.0976	0.0040	0.1073	0.0040	0.0198	0.0040	0.1063	0.0040
19	Fragment 284	0.0054	0.0040	0.0553	0.0040	0.0521	0.0040	0.0580	0.0040	0.0036	0.0040	0.0582	0.0040
20	Fragment 284	0.0027	0.0040	0.0146	0.0040	0.0146	0.0040	0.0147	0.0040	0.0026	0.0040	0.0150	0.0040
21		-125	-125	90	90	100	100	110	110	-125	-125	90	90
22	Fragment 370	0.8107	0.0050	0.5058	0.0050	0.4947	0.0050	0.4936	0.0050	0.8121	0.0050	0.4907	0.0050
23	Fragment 370	0.1542	0.0050	0.2480	0.0050	0.2511	0.0050	0.2493	0.0050	0.1549	0.0050	0.2491	0.0050
24	Fragment 370	0.0299	0.0050	0.1435	0.0050	0.1496	0.0050	0.1502	0.0050	0.0280	0.0050	0.1479	0.0050
25	Fragment 370	0.0041	0.0050	0.0696	0.0050	0.0690	0.0050	0.0729	0.0050	0.0040	0.0050	0.0777	0.0050
26	Fragment 370	0.0007	0.0050	0.0251	0.0050	0.0282	0.0050	0.0256	0.0050	0.0007	0.0050	0.0267	0.0050
27	Fragment 370	0.0004	0.0050	0.0080	0.0050	0.0075	0.0050	0.0084	0.0050	0.0003	0.0050	0.0079	0.0050

Figure D.3
An Excel spreadsheet defines MIDs and measurement errors (SE) for each timepoint of each experiment.

3. Press the **Import** button and select the *.xlsx file. Wait for the data to load. When prompted, save the updated model. After loading, the imported experiments will appear in the list (Figure D.4).
 - a. *Example:* import MIDs from **MIDs_test.xlsx** in **batch/example1**

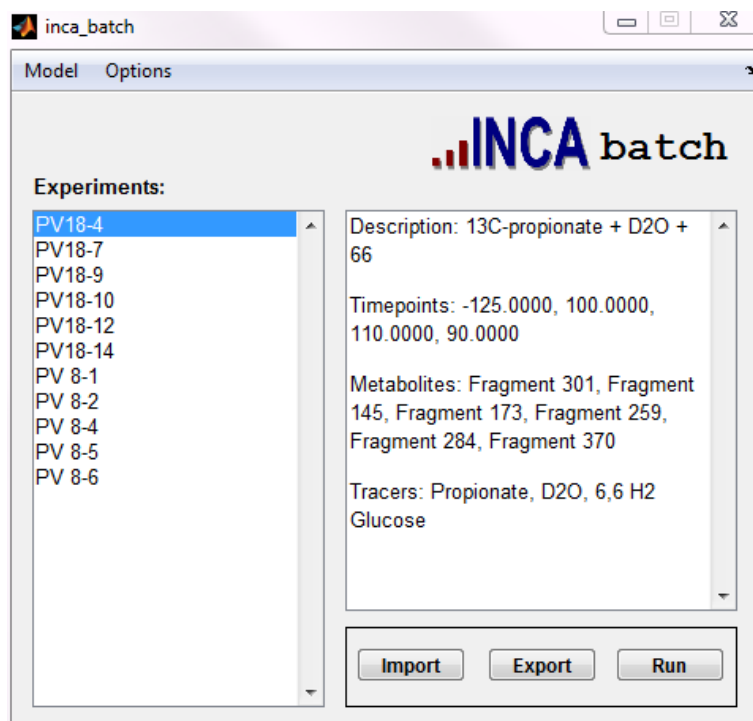


Figure D.4
The batch GUI displays the imported experiments.

Export Data

1. Select all of the experiments for which exported data is desired. Highlight multiple experiments by holding the Ctrl key or using Ctrl + Shift.
2. If MIDs should be corrected for natural abundance, ensure **Export corrected data** under the **Options** menu is checked (Figure D.5).
3. Press the **Export** button. When prompted, select a path and filename for the *.csv file.
 - a. The exported file will be formatted as shown in Figure D.3.

Fitting Data

Options (Figure D.5)

Export run set-up: When checked, exports a *.csv file that defines the settings for each fit run in the batch, including the samples, timepoints, and metabolites that were active, designated by a 1 or 0, during that run.

See batch/example1/run_test_setup.csv.

Fit each experiment: When checked, the GUI will fit each experiment separately. When unchecked, the GUI will fit all of the user-selected experiments at the same time.

Fit each timepoint: When checked, the GUI will fit each timepoint separately. When unchecked, the GUI will fit all of the user-selected timepoints at the same time.

Select timepoints...: Allows the user to select specific timepoints. For example, allows for the exclusion of baseline samples.

Fit options...: Allows the user to define the number of random starts and the confidence interval alpha value.

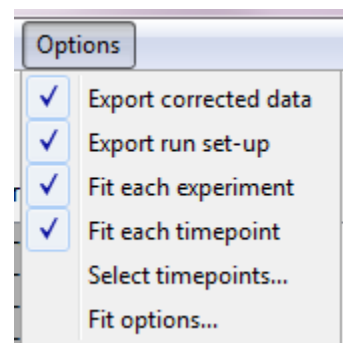


Figure D.5
The *Options* menu defines the batch protocol for data fitting.

Fitting Experiments to the Model

1. Select the experiments to fit to the model. Hold down the Ctrl key to highlight multiple experiments.
2. Set the desired fitting options as described above.
3. Press the **Run** button (Figure D.4). When prompted, select a path and filename for the data.

APPENDIX E

DESCRIPTION OF MATHEMATICAL MODELING FOR FLUX ANALYSIS

The INCA software suite (77) mathematically describes the metabolic reaction network (**Table A1**) through a series of balance equations that define the relationship between fluxes and MIDs. A decomposition method is used to break isotopomers into elementary metabolite units (EMUs) to reduce computational burden (3). Each EMU includes a subset of metabolite atoms directly involved in atom transitions. EMUs are organized into size blocks, where *size* refers to the number of atoms represented in the EMU. INCA employs size decoupling of large blocks for efficiency (78); furthermore, EMUs and EMU balance equations are derived through automation. These features allow INCA users to build models of arbitrary complexity, test assumptions, and perform simulations with relative ease. The analysis presented in this study can be replicated by setting up the network (**Table A1**) in INCA or in other software platforms designed for MFA (58, 63, 64, 74, 76, 79).

The network detailed in **Table A1** breaks down into 108 EMUs organized within 13 EMU blocks. One EMU balance equation is derived for each block of the form:

$$Ax + By = 0 \quad (\text{E.1})$$

where A and B are functions of model fluxes and x and y are functions of EMU MIDs. EMU balance equations are detailed in **S. Table 2**. In these equations, the fluxes in matrices A and B are described in **Table A1**. The x and y matrices define the EMU by the metabolite name and the subset of atoms it includes. EMU atom numbering is based on the atomic

definitions for each metabolite from **Table A1**. For example, carbon and hydrogen atoms in Gluc.ext are defined as AaBbCcDdEeFfg in the V_{EndoRa} model reaction, where capital letters refer to carbon atoms and lowercase letters refer to hydrogen atoms. The atoms are numbered sequentially for EMU definitions, where A=1, a=2, B=3, b=4, etc. There are six Gluc.ext EMUs (Table E.1) that correspond to the six measured glucose derivative fragments shown in **Figure 2B**. These EMUs are highlighted in bold in the EMU balance equations.

The relationships described in the EMU balance equations are logical. For example, the EMU balance equation for block 13 (Table E.2) shows that the mass isotopomer distribution for G6P (x , row 1) is dependent on the fluxes V_{GPI} , V_{PYGL} , and V_{EndoRa} (A, column 1). Total glucose, Gluc.ext (x , row 2), is dependent on the [6,6- $^2\text{H}_2$]glucose infusion flux, V_{inf} , and endogenous glucose production, V_{EndoRa} (A, column 2). The metabolites that form G6P and Gluc.ext EMUs, the *input* EMUs, are defined in y and include infused glucose (Gluc.inf), F6P, and Glycogen. These input EMUs feed through V_{inf} , V_{GPI} , and V_{PYGL} , respectively (B). The F6P input is shown as a convolution of a 12 atom F6P EMU MID and a hydrogen MID ($F6P_{1\cdot3\cdot4\cdot5\cdot6\cdot7\cdot8\cdot9\cdot10\cdot11\cdot12\cdot13} \times H_1$; y , row 2). The F6P EMU does not include the second defined atom, a hydrogen, because it is lost in the conversion of F6P to G6P and replaced by a hydrogen (H_1) from water. This hydrogen exchange is also represented in the convolution of a 12 atom glycogen EMU and a hydrogen MID ($Glycogen_{1\cdot2\cdot3\cdot5\cdot6\cdot7\cdot8\cdot9\cdot10\cdot11\cdot12\cdot13} \times H_1$; y , row 3). Since the outputs ($A * x$) and inputs ($B * y$) must balance, their sum is equal to zero.

Table E.1
Gluc.ext EMUs correspond to measured glucose fragments.

Gluc.ext EMUs	Fragment (m/z)
<i>Gluc.ext</i> _{1·2·3·4·5·6·7·8·9·10·11·12·13}	301
<i>Gluc.ext</i> _{1·3·4·5·6·7·8·9·10}	370
<i>Gluc.ext</i> _{7·8·9·10·11·12·13}	259
<i>Gluc.ext</i> _{1·3·4·5·6·7·8}	173
<i>Gluc.ext</i> _{9·10·11·12·13}	145
<i>Gluc.ext</i> _{1·2·3·4}	284

REFERENCES

1. **Antoniewicz MR, Kelleher JK, and Stephanopoulos G.** Accurate assessment of amino acid mass isotopomer distributions for metabolic flux analysis. *Analytical chemistry* 79: 7554-7559, 2007.
2. **Antoniewicz MR, Kelleher JK, and Stephanopoulos G.** Determination of confidence intervals of metabolic fluxes estimated from stable isotope measurements. *Metabolic engineering* 8: 324-337, 2006.
3. **Antoniewicz MR, Kelleher JK, and Stephanopoulos G.** Elementary metabolite units (EMU): a novel framework for modeling isotopic distributions. *Metabolic engineering* 9: 68-86, 2007.
4. **Antoniewicz MR, Kelleher JK, and Stephanopoulos G.** Measuring deuterium enrichment of glucose hydrogen atoms by gas chromatography/mass spectrometry. *Analytical chemistry* 83: 3211-3216, 2011.
5. **Arden SD, Zahn T, Steegers S, Webb S, Bergman B, O'Brien RM, and Hutton JC.** Molecular cloning of a pancreatic islet-specific glucose-6-phosphatase catalytic subunit-related protein. *Diabetes* 48: 531-542, 1999.
6. **Ashcroft SJ, and Randle PJ.** Glucose-6-phosphatase activity of mouse pancreatic islets. *Nature* 219: 857-858, 1968.
7. **Bentsi-Barnes K, Doyle ME, Abad D, and Kandeel F.** Detailed protocol for evaluation of dynamic perfusion of human islets to assess β -cell function. *Islets* 2011.
8. **Berglund M, and Wieser ME.** Isotopic compositions of the elements 2009 (IUPAC Technical Report). *Pure and Applied Chemistry* 83: 397-410, 2011.
9. **Bouatia-Naji N, Bonnefond A, Baerenwald DA, Marchand M, Bugliani M, Marchetti P, Pattou F, Printz RL, Flemming BP, Umunakwe OC, Conley NL, Vaxillaire M, Lantieri O, Balkau B, Marre M, Levy-Marchal C, Elliott P, Jarvelin MR, Meyre D, Dina C, Oeser JK, Froguel P, and O'Brien RM.** Genetic and functional assessment of the role of the rs13431652-A and rs573225-A alleles in the G6PC2 promoter that are strongly associated with elevated fasting glucose levels. *Diabetes* 59: 2662-2671, 2010.
10. **Bouatia-Naji N, Rocheleau G, Van Lommel L, Lemaire K, Schuit F, Cavalcanti-Proenca C, Marchand M, Hartikainen AL, Sovio U, De Graeve F, Rung J, Vaxillaire M, Tichet J, Marre M, Balkau B, Weill J, Elliott P, Jarvelin MR, Meyre D, Polychronakos C, Dina C, Sladek R, and Froguel P.** A polymorphism within the G6PC2 gene is associated with fasting plasma glucose levels. *Science* 320: 1085-1088, 2008.
11. **Boustead JN, Martin CC, Oeser JK, Svitek CA, Hunter SI, Hutton JC, and O'Brien RM.** Identification and characterization of a cDNA and the gene encoding the

mouse ubiquitously expressed glucose-6-phosphatase catalytic subunit-related protein. *Journal of molecular endocrinology* 32: 33-53, 2004.

12. **Boztug K, Appaswamy G, Ashikov A, Schaffer AA, Salzer U, Diestelhorst J, Germeshausen M, Brandes G, Lee-Gossler J, Noyan F, Gatzke AK, Minkov M, Greil J, Kratz C, Petropoulou T, Pellier I, Bellanne-Chantelot C, Rezaei N, Monkemoller K, Irani-Hakimeh N, Bakker H, Gerardy-Schahn R, Zeidler C, Grimbacher B, Welte K, and Klein C.** A syndrome with congenital neutropenia and mutations in G6PC3. *N Engl J Med* 360: 32-43, 2009.

13. **Burgess SC, He T, Yan Z, Lindner J, Sherry DA, Malloy CR, Browning JD, and Magnuson MA.** Cytosolic phosphoenolpyruvate carboxykinase does not solely control the rate of hepatic gluconeogenesis in the intact mouse liver. *Cell Metabolism* 5: 313-320, 2007.

14. **Caprio S.** Obesity and type 2 diabetes: the twin epidemic: preface. *Diabetes Spectrum* 16: 230-230, 2003.

15. **Chandramouli V, Khan A, Ostenson CG, Berggren PO, Low H, Landau BR, and Efendic SE.** Quantification of glucose cycling and the extent of equilibration of glucose 6-phosphate with fructose 6-phosphate in islets from ob/ob mice. *Biochem J* 278 (Pt 2): 353-359, 1991.

16. **Chen WM, Erdos MR, Jackson AU, Saxena R, Sanna S, Silver KD, Timpson NJ, Hansen T, Orru M, Grazia Piras M, Bonnycastle LL, Willer CJ, Lyssenko V, Shen H, Kuusisto J, Ebrahim S, Sestu N, Duren WL, Spada MC, Stringham HM, Scott LJ, Olla N, Swift AJ, Najjar S, Mitchell BD, Lawlor DA, Smith GD, Ben-Shlomo Y, Andersen G, Borch-Johnsen K, Jorgensen T, Saramies J, Valle TT, Buchanan TA, Shuldiner AR, Lakatta E, Bergman RN, Uda M, Tuomilehto J, Pedersen O, Cao A, Groop L, Mohlke KL, Laakso M, Schlessinger D, Collins FS, Altshuler D, Abecasis GR, Boehnke M, Scuteri A, and Watanabe RM.** Variations in the G6PC2/ABCB11 genomic region are associated with fasting glucose levels. *J Clin Invest* 118: 2620-2628, 2008.

17. **Chen Z, and Zhong C.** Decoding Alzheimer's disease from perturbed cerebral glucose metabolism: implications for diagnostic and therapeutic strategies. *Progress in Neurobiology* 108: 21-43, 2013.

18. **Cheung YY, Kim SY, Yiu WH, Pan CJ, Jun HS, Ruef RA, Lee EJ, Westphal H, Mansfield BC, and Chou JY.** Impaired neutrophil activity and increased susceptibility to bacterial infection in mice lacking glucose-6-phosphatase-beta. *J Clin Invest* 117: 784-793, 2007.

19. **Dadon D, Tornovsky-Babaey S, Furth-Lavi J, Ben-Zvi D, Ziv O, Schyr-Ben-Haroush R, Stolovich-Rain M, Hija A, Porat S, Granot Z, Weinberg-Corem N, Dor Y, and Glaser B.** Glucose metabolism: key endogenous regulator of beta-cell replication and survival. *Diabetes Obes Metab* 14 Suppl 3: 101-108, 2012.

20. **Easley C, Rocheleau J, Head W, and Piston D.** Quantitative measurement of zinc secretion from pancreatic islets with high temporal resolution using droplet-based microfluidics. *Analytical chemistry* 81: 9086-9095, 2009.
21. **Egnatchik RA, Leamy AK, Jacobson DA, and Shiota M.** ER calcium release promotes mitochondrial dysfunction and hepatic cell lipotoxicity in response to palmitate overload. *Molecular Metabolism* 3: 544–553, 2014.
22. **Egnatchik RA, Leamy AK, Noguchi Y, and Shiota M.** Palmitate-induced activation of mitochondrial metabolism promotes oxidative stress and apoptosis in H4IIEC3 rat hepatocytes. *Metabolism* 63: 283-295, 2014.
23. **Fernandez C, Des Rosiers C, Previs S, David F, and Brunengraber H.** Correction of ¹³C mass isotopomer distributions for natural stable isotope abundance. *Journal of mass spectrometry : JMS* 31: 255-262, 1996.
24. **Foster JD, Pederson BA, and Nordlie RC.** Glucose-6-phosphatase structure, regulation, and function: an update. *Proc Soc Exp Biol Med* 215: 314-332, 1997.
25. **Groen AK, Roermund VCW, Vervoorn RC, and Tager JM.** Control of gluconeogenesis in rat liver cells. Flux control coefficients of the enzymes in the gluconeogenic pathway in the absence and presence of glucagon. *Biochem J* 237: 379-389, 1986.
26. **Han B, Serra P, Amrani A, Yamanouchi J, Maree AF, Edelstein-Keshet L, and Santamaria P.** Prevention of diabetes by manipulation of anti-IGRP autoimmunity: high efficiency of a low-affinity peptide. *Nat Med* 11: 645-652, 2005.
27. **Hasenour CM, Wall ML, and Ridley DE.** Mass Spectrometry-Based Microassay of ²H and ¹³C Plasma Glucose Labeling to Quantify Liver Metabolic Fluxes In vivo. *American Journal of Physiology, Endocrinology and Metabolism* 309: 191-203, 2015.
28. **Heiden VMG, Cantley LC, and Thompson CB.** Understanding the Warburg effect: the metabolic requirements of cell proliferation. *Science* 324: 1029-1033, 2009.
29. **Hutton JC, and O'Brien RM.** The glucose-6-phosphatase catalytic subunit gene family. *J Biol Chem* 284: 29241-29245, 2009.
30. **Iynedjian PB.** Molecular physiology of mammalian glucokinase. *Cellular and molecular life sciences : CMLS* 66: 27-42, 2009.
31. **Jarchum I, Nichol L, Trucco M, Santamaria P, and DiLorenzo TP.** Identification of novel IGRP epitopes targeted in type 1 diabetes patients. *Clin Immunol* 127: 359-365, 2008.
32. **Jin ES, Beddow SA, Malloy CR, and Samuel VT.** Hepatic glucose production pathways after three days of a high-fat diet. *Metabolism* 62: 152-162, 2013.

33. **Jin ES, Jones JG, Merritt M, Burgess SC, and Malloy CR.** Glucose production, gluconeogenesis, and hepatic tricarboxylic acid cycle fluxes measured by nuclear magnetic resonance analysis of a single glucose derivative. *Analytical Biochemistry* 327: 149-155, 2004.
34. **Jones JG, Solomon MA, Cole SM, Sherry AD, and Malloy CR.** An integrated ²H and ¹³C NMR study of gluconeogenesis and TCA cycle flux in humans. *American Journal of Physiology-Endocrinology And Metabolism* 281: 848-856, 2001.
35. **Kayton NS, Poffenberger G, and Henske J.** Human islet preparations distributed for research exhibit a variety of insulin-secretory profiles. *American Journal of Physiology, Endocrinology and Metabolism* 308: 592-602, 2015.
36. **Khan A, Chandramouli V, Ostenson CG, Ahren B, Schumann WC, Low H, Landau BR, and Efendic S.** Evidence for the presence of glucose cycling in pancreatic islets of the ob/ob mouse. *J Biol Chem* 264: 9732-9733, 1989.
37. **Khan A, Chandramouli V, Ostenson CG, Berggren PO, Low H, Landau BR, and Efendic S.** Glucose Cycling Is Markedly Enhanced in Pancreatic-Islets of Obese Hyperglycemic Mice. *Endocrinology* 126: 2413-2416, 1990.
38. **Khan A, Chandramouli V, Ostenson CG, Low H, Landau BR, and Efendic S.** Glucose cycling in islets from healthy and diabetic rats. *Diabetes* 39: 456-459, 1990.
39. **Khan A, and Efendic S.** Evidence That Increased Glucose Cycling in Islets of Diabetic Ob/Ob Mice Is a Primary Feature of the Disease. *Am J Physiol-Endoc M* 269: E623-E626, 1995.
40. **Khan A, Narangoda S, Ahren B, Holm C, Sundler F, and Efendic S.** Long-term leptin treatment of ob/ob mice improves glucose-induced insulin secretion. *Int J Obes Relat Metab Disord* 25: 816-821, 2001.
41. **Kim NH.** Obstructive sleep apnea and abnormal glucose metabolism. *Diabetes & metabolism journal* 36: 268-272, 2012.
42. **Kooi BT, Onuma H, Oeser JK, Svitek CA, Allen SR, Kooi CW, Chazin WJ, and O'Brien RM.** The glucose-6-phosphatase catalytic subunit gene promoter contains both positive and negative glucocorticoid response elements. *Molecular Endocrinology* 19: 3001-3022, 2005.
43. **Landau BR, Wahren J, Chandramouli V, Schumann WC, Ekberg K, and Kalhan SC.** Contributions of gluconeogenesis to glucose production in the fasted state. *The Journal of clinical investigation* 98: 378-385, 1996.
44. **Laybutt DR, Glandt M, Xu G, Ahn YB, Trivedi N, Bonner-Weir S, and Weir GC.** Critical reduction in beta-cell mass results in two distinct outcomes over time. Adaptation with impaired glucose tolerance or decompensated diabetes. *J Biol Chem* 278: 2997-3005, 2003.

45. **Leamy AK, Egnatchik RA, and Young JD.** Molecular mechanisms and the role of saturated fatty acids in the progression of non-alcoholic fatty liver disease. *Progress in lipid research* 52: 165-174, 2013.
46. **Lieberman SM, Evans AM, Han B, Takaki T, Vinnitskaya Y, Caldwell JA, Serreze DV, Shabanowitz J, Hunt DF, Nathenson SG, Santamaria P, and DiLorenzo TP.** Identification of the beta cell antigen targeted by a prevalent population of pathogenic CD8+ T cells in autoimmune diabetes. *Proc Natl Acad Sci U S A* 100: 8384-8388, 2003.
47. **Malaisse W, Malaisse-Lagae F, Liemans V, Ottinger R, and Willem R.** Phosphoglucoisomerase-catalyzed interconversion of hexose phosphates: isotopic discrimination between hydrogen and deuterium. *Molecular and cellular biochemistry* 93: 153-165, 1990.
48. **Martin CC, Bischof LJ, Bergman B, Hornbuckle LA, Hilliker C, Frigeri C, Wahl D, Svitek CA, Wong R, Goldman JK, Oeser JK, Lepretre F, Froguel P, O'Brien RM, and Hutton JC.** Cloning and characterization of the human and rat islet-specific glucose-6-phosphatase catalytic subunit-related protein (IGRP) genes. *J Biol Chem* 276: 25197-25207, 2001.
49. **Martin CC, Oeser JK, Svitek CA, Hunter SI, Hutton JC, and O'Brien RM.** Identification and Characterization of a Human cDNA and Gene Encoding a Ubiquitously Expressed Glucose-6-Phosphatase Catalytic Subunit-Related Protein. *Journal of molecular endocrinology* 29: 205-222, 2002.
50. **Matschinsky FM.** Banting Lecture 1995. A lesson in metabolic regulation inspired by the glucokinase glucose sensor paradigm. *Diabetes* 45: 223-241, 1996.
51. **Mithieux G.** New knowledge regarding glucose-6 phosphatase gene and protein and their roles in the regulation of glucose metabolism. *Eur J Endocrinol* 136: 137-145, 1997.
52. **Mukherjee R, Wagar D, Stephens TA, Lee-Chan E, and Singh B.** Identification of CD4+ T cell-specific epitopes of islet-specific glucose-6-phosphatase catalytic subunit-related protein: a novel beta cell autoantigen in type 1 diabetes. *J Immunol* 174: 5306-5315, 2005.
53. **Murphy TA, Dang CV, and Young JD.** Isotopically nonstationary ¹³C flux analysis of Myc-induced metabolic reprogramming in B-cells. *Metabolic engineering* 15: 206-217, 2012.
54. **O'Brien RM.** Moving on from GWAS: functional studies on the G6PC2 gene implicated in the regulation of fasting blood glucose. *Current diabetes reports* 13: 768-777, 2013.
55. **Perales MA, Sener A, and Malaisse WJ.** Hexose metabolism in pancreatic islets: the glucose-6-phosphatase riddle. *Mol Cell Biochem* 101: 67-71, 1991.

56. **Petrolonis A, Yang Q, Tummino P, Fish S, Prack A, Jain S, Parsons T, Li P, Dales N, Ge L, Langston S, Schuller A, An W, Tartaglia L, Chen H, and Hong S-B.** Enzymatic characterization of the pancreatic islet-specific glucose-6-phosphatase-related protein (IGRP). *The Journal of biological chemistry* 279: 13976-13983, 2004.
57. **Pound LD, Oeser JK, O'Brien TP, Wang Y, Faulman CJ, Dadi PK, Jacobson DA, Hutton JC, McGuinness OP, Shiota M, and O'Brien RM.** G6PC2: a negative regulator of basal glucose-stimulated insulin secretion. *Diabetes* 62: 1547-1556, 2013.
58. **Quek L-EE, Wittmann C, Nielsen LK, and Krömer JO.** OpenFLUX: efficient modelling software for ¹³C-based metabolic flux analysis. *Microbial cell factories* 8: 25, 2008.
59. **Rocheleau J, Walker G, Head W, McGuinness O, and Piston D.** Microfluidic glucose stimulation reveals limited coordination of intracellular Ca²⁺ activity oscillations in pancreatic islets. *Proceedings of the National Academy of Sciences of the United States of America* 101: 12899-12903, 2004.
60. **Rowe I, Chiaravalli M, Mannella V, Ulisse V, and Quilici G.** Defective glucose metabolism in polycystic kidney disease identifies a new therapeutic strategy. *Nature medicine* 19: 488-493, 2013.
61. **Satapati S, Sunny NE, Kucejova B, Fu X, He TT, Méndez-Lucas A, Shelton JM, Perales JC, Browning JD, and Burgess SC.** Elevated TCA cycle function in the pathology of diet-induced hepatic insulin resistance and fatty liver. *Journal of lipid research* 53: 1080-1092, 2012.
62. **Small GW, Ercoli LM, and Silverman DHS.** Cerebral metabolic and cognitive decline in persons at genetic risk for Alzheimer's disease. *Proc Natl Acad Sci U S A* 97: 6037-6042, 2000.
63. **Sokol S, Millard P, and Portais JC.** influx_s: increasing numerical stability and precision for metabolic flux analysis in isotope labelling experiments. *Bioinformatics* 28: 687-93, 2012.
64. **Srour O, Young JD, and Eldar YC.** Fluxomers: a new approach for ¹³C metabolic flux analysis. *BMC systems biology* 5: 129, 2010.
65. **Sunny NE, Parks EJ, Browning JD, and Burgess SC.** Excessive hepatic mitochondrial TCA cycle and gluconeogenesis in humans with nonalcoholic fatty liver disease. *Cell metabolism* 14: 804-810, 2011.
66. **Sweet IR, Najafi H, Li G, Grodberg J, and Matschinsky FM.** Measurement and modeling of glucose-6-phosphatase in pancreatic islets. *Am J Physiol* 272: E696-711, 1997.
67. **Templeton N, Lewis A, Dorai H, Qian EA, Campbell MP, Smith KD, Lang SE, Betenbaugh MJ, and Young JD.** The impact of anti-apoptotic gene Bcl-2 expression on CHO central metabolism. *Metabolic engineering* 25: 92-102, 2014.

68. **Tokuyama Y, Sturis J, DePaoli AM, Takeda J, Stoffel M, Tang J, Sun X, Polonsky KS, and Bell GI.** Evolution of beta-cell dysfunction in the male Zucker diabetic fatty rat. *Diabetes* 44: 1447-1457, 1995.
69. **van de Werve G, Lange A, Newgard C, Mechin MC, Li Y, and Berteloot A.** New lessons in the regulation of glucose metabolism taught by the glucose 6-phosphatase system. *Eur J Biochem* 267: 1533-1549, 2000.
70. **Van Schaftingen E, and Gerin I.** The glucose-6-phosphatase system. *Biochem J* 362: 513-532, 2002.
71. **Wall ML, Pound LD, Trenary I, and O'Brien RM.** Novel Stable Isotope Analyses Demonstrate Significant Rates of Glucose Cycling in Mouse Pancreatic Islets. *Diabetes* 64: 2129-2137, 2015.
72. **Wang Y, Martin CC, Oeser JK, Sarkar S, McGuinness OP, Hutton JC, and O'Brien RM.** Deletion of the Gene Encoding the Islet-Specific Glucose-6-Phosphatase Catalytic Subunit-Related Protein Autoantigen Results in a Mild Metabolic Phenotype. *Diabetologia* 50: 774-778, 2007.
73. **Wegner A, Weindl D, ger C, Sapcariu SC, Dong X, Stephanopoulos G, and Hiller K.** Fragment formula calculator (FFC): determination of chemical formulas for fragment ions in mass spectrometric data. *Analytical chemistry* 86: 2221-2228, 2014.
74. **Weitzel M, Nöh K, Dalman T, Niedenführ S, Stute B, and Wiechert W.** 13CFLUX2—high-performance software suite for 13C-metabolic flux analysis. *Bioinformatics* 29: 143-145, 2013.
75. **Yang J, Danke NA, Berger D, Reichstetter S, Reijonen H, Greenbaum C, Pihoker C, James EA, and Kwok WW.** Islet-specific glucose-6-phosphatase catalytic subunit-related protein-reactive CD4+ T cells in human subjects. *J Immunol* 176: 2781-2789, 2006.
76. **Yoo H, Antoniewicz MR, and Stephanopoulos G.** Quantifying reductive carboxylation flux of glutamine to lipid in a brown adipocyte cell line. *The Journal of biological chemistry* 283: 20621-20627, 2008.
77. **Young JD.** INCA: a computational platform for isotopically non-stationary metabolic flux analysis. *Bioinformatics (Oxford, England)* 30: 1333-1335, 2014.
78. **Young JD, Walther JL, Antoniewicz MR, Yoo H, and Stephanopoulos G.** An elementary metabolite unit (EMU) based method of isotopically nonstationary flux analysis. *Biotechnology and Bioengineering* 99: 686-699, 2008.
79. **Zamboni N, Fischer E, and Sauer U.** FiatFlux--a software for metabolic flux analysis from 13C-glucose experiments. *BMC bioinformatics* 6: 209, 2004.

80. **Zhang H, Stevens RD, Young SP, and Surwit R.** A Convenient LC-MS Method for Assessment of Glucose Kinetics In Vivo with d-[13C6] Glucose as a Tracer. *Clinical chemistry* 55: 527-532, 2009.